Final Technical Report

Project Title:	Narrow-Channel, Fluidized Beds for Effective Particle Thermal Energy Transport and Storage
Project Period:	02/01/19 – 03/31/23
Submission Date:	04/11/23
Recipient:	Colorado School of Mines
Address:	1500 Illinois St. Golden, CO 80401
Website (if available)	www.mines.edu
Award Number:	DE-EE0008538
Project Team:	Sandia National Laboratories
Principal Investigator:	Gregory S. Jackson, Professor Phone: 303-273-3609 Email: gsjackso@mines.edu
Business Contact:	Elizabeth Sanders, Contracts Administrator Phone: 303-384-2302 Email: evsanders@mines.edu
Technology Manager:	Shane Powers
Project Officer:	Christine Bing
Grant Specialist:	Elizabeth Parrish
Contracting Officer:	Clay Pfrangle

Acknowledgement: *This material is based upon work supported by the U.S. Department of Energy's Office of Energy Efficiency and Renewable Energy (EERE) under the Solar Energy Technologies Office (SETO) award number DE-EE0008538.*

Disclaimer: *This report was prepared as an account of work sponsored by an agency of the United States Government. Neither the United States Government nor any agency thereof, nor any of their employees, makes any warranty, express or implied, or assumes any legal liability or responsibility for the accuracy, completeness, or usefulness of any information, apparatus, product, or process disclosed, or represents that its use would not infringe privately owned rights. Reference herein to any specific commercial product, process, or service by trade name, trademark, manufacturer, or otherwise does not necessarily constitute or imply its endorsement, recommendation, or favoring by the United States Government or any agency thereof. The views and opinions of authors expressed herein do not necessarily state or reflect those of the United States Government or any agency thereof.*

Executive Summary: Colorado School of Mines (Mines) led this program in collaboration with Sandia National Laboratories (Sandia) to characterize narrow-channel fluidized beds of aluminosilicate particles – supplied by Carbo Ceramics – as a means for releasing high-temperature thermal energy in particle heat exchangers and for capturing concentrated solar energy in indirect particle receivers. Single-channel, heat transfer experiments at Mines and reduced-order 1-D models and 3-D two-fluid, CFD models explored many aspects of counterflow, bubbling fluidized beds (net downward particle flow and upward gas flow) for enhancing particle-wall heat transfer at elevated temperatures. Results at Mines on single-channel test sections consistently showed that mild bubbling fluidization increases particle-wall heat transfer coefficients ($h_{T,w}$) regularly by more than 4.0× over $h_{T,w}$ values without fluidization at similar conditions (mean particle diameter d_p, bed depth Δz_b, and bed particle temperatures T_p).

Insights from lab-scale tests and modeling studies provided Nusselt number correlations for $h_{T,w}$ and informed the design and fabrication (by Vacuum Process Engineering) of a nominal 40-kW$_{th}$, particle-sCO$_2$ plate heat exchanger (HX) with 12 parallel narrow-channel, fluidized beds bounded by stainless-steel walls with embedded microchannels for high-pressure sCO$_2$ flows. Tests of the 40-kW$_{th}$ HX at the particle-sCO$_2$ HX test stand at Sandia's National Solar Thermal Test Facility (NSTTF) were limited, due to HX design, to particle inlet temperatures $T_{p,in} \leq 520°C$ with maximum sCO$_2$ outlet temperatures $T_{sCO2,out} \approx 440°C$, which are well below design conditions for a primary HX in a sCO$_2$ power cycle for a Gen-3 concentrating solar power (CSP) plant. Total heat transfer $\dot{Q}_{HX}$ remains relatively constant with increased fluidization for fixed particle and sCO$_2$ inlet conditions because higher $h_{T,w}$ due to fluidization is offset by increased axial dispersion, which suppresses temperature differences between the particles and sCO$_2$ in the counterflow configuration. The axial dispersion reduces the effective overall heat transfer coefficient U based on $T_{p,in}$ to values around 200 W m^{-2} K^{-1}.

Results from this program provide key quantitative insights into the potential and challenges for narrow-channel, fluidized-bed HXs to meet performance and cost targets for primary HXs for thermal energy storage (TES) subsystems in CSP applications. Nusselt number correlations derived from single-channel test results at Mines suggest pathways to higher $h_{T,w} \geq 1000$ W m^{-2} K^{-1} for $T_{p,in} > 600°C$ and particle $d_p < 250$ μm. Such high $h_{T,w}$ may be achieved with gas mass fluxes < 2% of downward design particle mass fluxes of ≈10 kg m^{-2} s^{-1}. However, such high $h_{T,w}$ only benefits HX design if strategies are developed to reduce axial dispersion. Higher particle mass fluxes showed some benefit to reducing the effects of dispersion without changing $h_{T,w}$ significantly. Exploratory 100-h tests on wall wear and particle attrition during mild fluidization at $T_p \approx 500°C$ indicated no significant measurable impact on wall oxide layers or on particle size distribution, and these results combined with the low parasitic loads to support necessary fluidizing gas mass flows informed system models that show sustainable fluidization conditions can be sustained with < 2% parasitic energy loss to drive and heat the gas flows. Further development of narrow-channel, fluidized beds for both primary HXs and indirect particle receivers will benefit significantly from qualitative and quantitative insights gained from this study, and any efforts to reduce axial dispersion in bubbling counterflow fluidized beds may enable smaller particle-sCO$_2$ HXs or indirect particle receivers for future CSP applications.

Table of Contents

1. Project background, objectives, and overview

1.1. Background

Oxide particles have been identified as one of the most promising means of high-temperature thermal energy storage (TES) at temperatures above 600°C [1, 2] where conventional molten-nitrate salt mixtures decompose [3]. Oxide particles have been chosen by the U.S. Dept of Energy (DOE) as the TES and heat transfer media for the next-generation Gen 3 Particle Pilot concentrating solar power (CSP) plant [4]. Both inert and reactive oxide particles have been considered, but current emphasis has been on inert oxide materials such as sands [5] and engineered aluminosilicate ceramic particles, like those made by Carbo Ceramics [6]. The engineered aluminosilicate particles, such as Carbo Ceramics CARBOBEAD HSP, offer high particle density ρ_p = 3610 kg m^{-3} with a relatively high specific heat capacity, $c_{p,p} \approx$ 1200 J kg^{-1} K^{-1} at 600°C [7]. Current expectation is that a TES subsystem coupled to recompression closed Brayton (RCBC) power cycles with sCO$_2$ as the working fluid will support high conversion of stored thermal energy to electric power at efficiencies > 50% [8].

Highly recuperated RCBC sCO$_2$ power cycles will require a relatively small change in temperature in the range of $T_{sCO2,out} - T_{sCO2,in} \approx$ 150°C in the primary heat source [9], which for a plant coupling particle-based TES to the power cycle would be the particle-sCO$_2$ heat exchanger (HX). $T_{sCO2,out}$ for an RCBC sCO$_2$ cycle is expected to be at least 700°C [1]. With likely approach temperatures of the particle-sCO$_2$ HX between 20 and 50°C, particle temperatures across the primary HX are expected to range from $T_{p,in} \approx$ 750°C to $T_{p,out} \approx$ 570°C [10]. Such a temperature range provides a particle specific enthalpy difference, $\Delta h_p \approx$ 240 kJ/kg for CARBOBEAD HSP, which will require particle flows at approximately 4.2 kg/s for every MW$_{th}$ of stored enthalpy extracted from the particles. Such large mass flows at such high temperatures will require expensive Ni alloys for sustained operation, and that places an emphasis on designing a volumetrically efficient HX with a high overall heat transfer coefficient, U, and high total heat exchange surface area, A_{tot} per unit volume to minimize the mass and cost of Ni alloys. DOE cost targets for the sCO$_2$ power block of < \$900/kW$_{elec}$ [9] can be translated roughly into heat exchanger costs of < \$150/kW$_{th}$ [11].

Transferring thermal energy out of hot particles into a power-cycle fluid through an HX presents many challenges because it requires controlled flow of particles from a hot storage bin at high temperatures. Two principal architectures for high-temperature particle HX have received the most attention for development over the past several years: 1) moving packed bed particle HXs [10-13], and 2) fluidized bed particle HXs [14-17]. A recent study by Sandia evaluated these approaches and different geometries (shell-and-tube vs. plate) weighed many factors including cost, scalability, and other factors, and the authors concluded that the cost benefits of the simpler moving packed bed designs made them most attractive for an initial development effort. In general, gravity-fed moving packed beds offer simplicity without complications and associated costs of injecting and separating fluidizing gas flow from the downward particle flows.

Early work at DLR in Germany focused on a moving packed-bed, particle-thermal oil HX with external, granular flow over horizontal tubes. This study reported effective particle-wall $h_{T,w}$ of 240 W m^{-2} K^{-1}, but these values were obtained at conditions of heat exchanger effectiveness ε_{HX} < 50% [12]. The extensive moving packed bed plate HX development at Sandia has significantly advanced understanding on how to control and condition moving packed bed particle flows for stable heat exchanger performance with multiple parallel channels of no more than a few mm in thickness. Initial parametric design studies of a moving packed bed plate HX showed a pathway with narrow bed channels down to 3 mm for particle diameters $d_p \leq 300$ μm (to avoid particle bridging in the narrow channels) to achieve overall U approaching 400 W m^{-2} K^{-1} at expected primary HX operating conditions with the sCO$_2$ flow in banks with cross-flow arrangements [1, 11]. Initial tests of a stainless-steel, moving packed bed HX with 3 banks of sCO$_2$ cross-flow using

CARBOBEAD HSP 40/70 demonstrated low overall U (< 80 W m^{-2} K^{-1}) due in part to limited $T_{p,in}$ < 300°C and due to relatively large bed channel depths [10]. Design of a stainless-steel, 20-kW_{th} moving packed bed HX provided with smaller 3.0 mm deep channels enabled significant improvements with overall $U \approx 300$ W m^{-2} K^{-1} at particle mass fluxes through the channels approaching 25 kg m^{-2} s^{-1} and $T_{p,in}$ ranging from 200°C to 500°C [18]. Interestingly, although it has been assumed that the sCO_2 side heat transfer is not the limiting thermal resistance, increasing the sCO_2 flowrates by 50% over design conditions increased U to ≈ 400 W m^{-2} K^{-1} at $T_{p,in}$ = 500°C. These results are very encouraging, but still fall short of what the authors identified as a desirable $U \approx 600$ W m^{-2} K^{-1} for moving-packed-bed plate HX to likely meet DOE cost targets [18]. Another recent study from CSIRO in Australia identified the benefit of staging the moving packed bed to break up the granular flow temperature profile, which improved the particle-wall heat transfer coefficient $h_{T,w}$ in a counterflow shell-and-tube HX [13]. Like the Sandia study, the CSIRO study showed minimal influence of particle mass flux on the overall U.

Although inherently more complicated due to the need for injecting fluidization gas, fluidized bed HXs have the potential to achieve higher overall U. Numerous studies have shown that fluidization increases particle-wall $h_{T,w}$ over granular flow from 2 to 5× [17, 19, 20] for Geldart type B particles typically used in high-temperature TES. This increase in $h_{T,w}$ lowers the presumed limiting thermal resistance between the particles and the wall and motivates developments of fluidized bed HX for particle-based TES subsystems. Studies show that >80% of the improvements in $h_{T,w}$ over granular flow values are achieved with superficial fluidization velocities, U_g that are not more than 3× the minimum fluidization velocity U_{mf} for Geldart type B particles [17, 20, 21]. For oxide particles with $d_p \leq 300$ μm at primary HX conditions, U_{mf} is 0.15 m s^{-1} or lower. As such, the low air mass rates needed to achieve preferred U_g with significant enhancement in $h_{T,w}$ present a relatively small parasitic load.

Different approaches to fluidized bed HXs for TES subsystems have been implemented. An early study on particle-wall heat transfer in a channel-like fluidized bed heat transfer for CSP applications at CNRS in France showed how $h_{T,w}$ increases significantly with T_p up to 800°C, but even more significantly, the results showed how lowering d_p down to 280μm raised $h_{T,w}$ up to 500 W m^{-2} K^{-1} at a low U_g close to U_{mf} [19]. That early study did not explore a very broad range of U_g, but the seminal work of Molerus [20, 22, 23] provided critical insight into developing meaningful correlations for convective Nusselt number Nu_{pc} to derive $h_{T,w}$ functional dependencies for Geldart type B particles with respect to particle Archimedes number Ar_{lam} and a dimensionless excess fluidization velocity $\hat{U}$.

Multiple fluidized bed HXs for thermal energy storage incorporated large open circulating beds with horizontal fluid tubes [15-17, 24-26]. These designs, however, are likely not favorable for the primary sCO_2 HX application because the high surface area needed for the fluid side requires large numbers of relatively small diameter tubes to minimize thermal resistance on the fluid side. Furthermore, the crossflow arrangement of these HXs tends to lower the mean-temperature difference in comparison to more effective counterflow designs. Some recent studies including the development discussed in this report, have explored counterflow plate heat exchangers with a net particle flow in the fluidized bed in counterflow to the power fluid [14, 27]. The counterflow fluidized bed design here benefits from insights gained from similar moving-packed bed HXs.

In addition to primary HX applications, the current program explored the potential for utilizing fluidized beds of Geldart type B particles for indirect particle receiver applications. Although currently, the US DOE and the Australian government have funded the development of open falling curtain particle receivers [28-30] in order to minimize the needs for expensive high-temperature confinement walls and complex optics to protect leading edges of confinement structures. The DOE has chosen the falling particle curtain receiver design for the Gen-3 particle-based Pilot Plant [4]. However, uncertainty about the scalability and reliability of the falling particle curtain receiver concepts has encouraged continued exploration of indirect particle cavity receivers, where the particles are confined inside high-surface area angled walls that receive highly concentrated solar radiation in open receiver apertures. Such concepts were encouraged by exploration of particles with thermochemical energy storage (TCES) with reducible perovskite oxides being used to achieve higher energy storage densities by supplementing sensible energy with endothermic chemical reduction [2, 31-33]. For indirect particle receivers with inert oxides that only have sensible energy storage, high particle-wall $h_{T,w}$ are critical to avoid excessive wall temperatures that compromise structural materials [2, 34]. As such, confined fluidized beds with high $h_{T,w}$ in upward, horizontal, or downward net particle flows have been considered for receiver applications [34-37]. As of yet, none of these concepts have been demonstrated at a scale that merits large-scale demonstration as is the case for the falling particle curtain [38].

While fluidized beds offer the potential for very high particle-wall heat transfer rates, they present complications with respect to parasitic loads in terms of heat loss and electric power to drive the fluidizing flows against the pressure drop necessary for fluidization. The issue of parasitic losses has often been discussed as a concern for fluidization, but to-date, they have not been studied in a sufficiently quantitative nature to understand their severity [1, 14]. In addition, fluidization of particles may enhance particle attrition as well as wear on high-temperature HX wall surfaces that are most likely surface oxide layers. While past studies have looked at wall surface wear inside fluidized beds [39, 40], only one recent study has documented well how high-temperature particle impact influences the wear of HX surfaces expected in high-temperature particle HXs and indirect receivers [41]. However, even that recent study does not clearly address the unique environment of bubbling fluidized beds where relatively low velocities can provide significant benefits in particle-wall $h_{T,w}$.

This research was motivated by the potential for narrow-channel, counterflow fluidized beds to provide a cost-effective design for particle-sCO$_2$ HXs and a possible solution for indirect, particle cavity receivers. Experimental tests at the lab-scale provided a measurement of the particle wall $h_{T,w}$, that was implemented into modeling tools to assess the viability of fluidized beds to meet performance targets for next-generation CSP plants. The quantitative $h_{T,w}$ analysis was combined with practical insight gained from rig operation to design, fabricate, and test a 12-channel. fluidized bed particle-sCO$_2$ HX to establish qualitative as well as quantitative insights on the design and operation of a multiple-channel fluidized bed HX for a TES subsystem in a CSP plant. Performance measurements were complemented by some simple studies on particle-wall wear and parasitic losses to understand the viability of preferred operating conditions and materials to survive in a practical application for next-generation CSP plants.

1.2. Introduction

This project sought to demonstrate the potential of narrow-channel, counterflow fluidized beds to reduce the size of particle-sCO_2 HXs and to a lesser extent, to enable indirect particle receiver designs for central tower CSP plants. Figure 1a illustrates the concept behind the project in a process schematic of a vertically integrated TES subsystem in a CSP plant. In the particle-based TES subsystems, solar heat is captured in oxide particles as they pass down through the fluidized-bed indirect-receiver into the hot storage bin. The hot storage bin feeds a particle-sCO_2 HX with fluidized beds that serves as the primary heat source for a recompression sCO_2 Brayton power cycle.

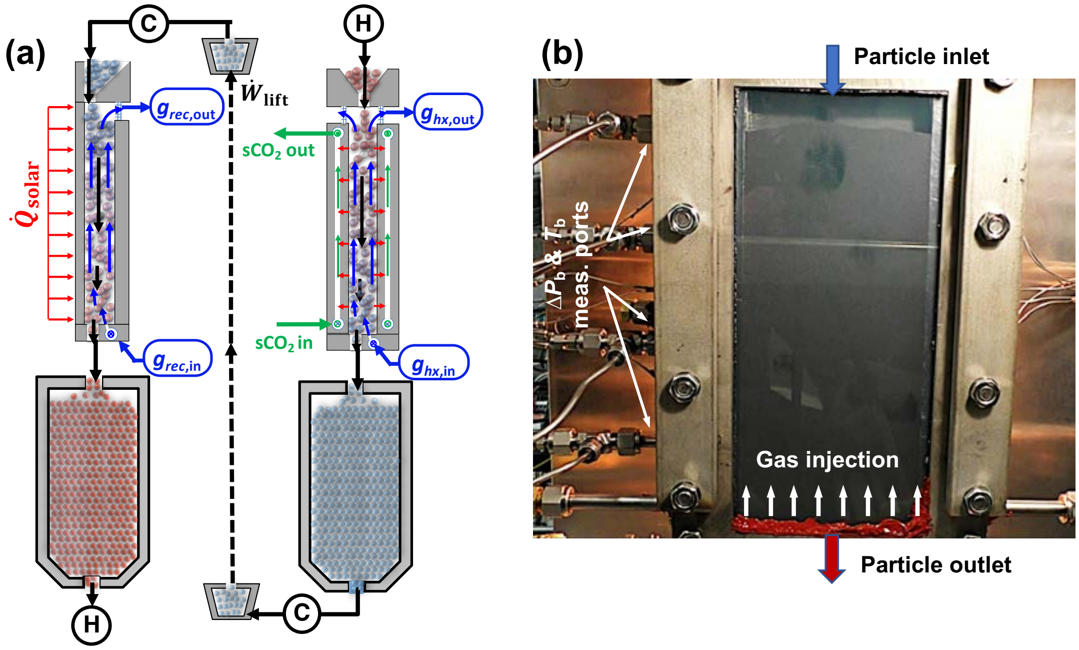

Figure 1: a) Schematic drawing of a TES subsystem for a CSP plant that employs narrow-channel counterflow fluidized beds for both an indirect particle receiver and a particle-sCO_2 heat exchanger. The single bed schematic illustrates the counterflow of the falling particles and the upward fluidizing gas flow that can be less than 1% of the solid flow on a mass basis. b) An image of the narrow-channel counterflow fluidized bed heat transfer rig operating with a conductive fluorinated-tin-oxide window for fluidized bed flow visualization.

Very high $h_{T,w}$ in the narrow-channel beds represent a potential pathway to smaller, cost-effective particle-sCO_2 HXs and to indirect cavity particle receivers with aperture solar fluxes (> 1000 suns) and wall temperatures $T_{w,ext}$ under 1000°C [2].

For this project, a single narrow channel test rig was used to investigate counterflow fluidized bed heat transfer and explore the feasibility of sustaining high heat transfer uniformly and steady flows of particles downward and gas upward . These tests led to the development of Nusselt number correlations for evaluating local convective $h_{T,w}$ that were incorporated into design models for a multi-channel demonstration-scale 40-kW$_{th}$ particle-sCO$_2$ HX. Figure 1b) illustrates the test rig with a bed height of ≈ 25 cm operating in a counterflow configuration with an upward air mass flow rate, $\dot{m}_{g,in} \approx$ 2% of the downward particle mass flow rate $\dot{m}_{p,in}$. A successful test campaign in the single-channel test rig calibrated numerical modeling tools that enabled design, assembly, and testing of the multi-bed 40-kW$_{th}$, particle-sCO$_2$ HX. Multi-physics modeling provided a basis for evaluating the robustness of HX design and for exploring indirect cavity particle receiver designs, which may also depend on development of oxide coatings for passive thermal management of leading edges where concentrated incident fluxes are normal to the surface. Analysis of a full-scale TES subsystem will motivate further investment and development of the particle-to-sCO$_2$ heat exchangers and indirect particle receivers for implementation in CSP applications.

1.3. Project objectives

The goal of this R&D program involved identifying designs and operating conditions for narrow-channel, fluidized beds of inert oxide particles to serve as primary particle HX heat sources for power cycles and as indirect particle receivers in CSP plants. Lab-scale testing and multiphase-flow modeling of narrow-channel counterflow fluidized beds were established to identify preferred oxide particle properties, optimal fluidized bed operating regimes, and wall/channel configurations for efficient particle-sCO$_2$ HXs and indirect particle receivers at part of a TES subsystem for concentrating solar power plants. This project also sought to address other key aspects of implementing fluidized beds for both primary HX and indirect receiver applications including wall wear, particle attrition, and protective oxide coatings. The overall project goals as laid out in the Statement of Program Objectives (SOPO) are summarized here:

- scalable fluidized bed particle-sCO$_2$ HX design with flow paths that provide average $h_{T,w} \geq 1000$ W m^{-2} K^{-1} with effectiveness, $\varepsilon_{hx} > 80\%$.
- testing of a stainless-steel particle-sCO$_2$ HX that transfers 40 kW$_{th}$ at $T_{p,in} \geq 600°C$ with a drop in $T_p \geq 150°C$, mean $h_{T,w} \geq 1000$ W m^{-2} K^{-1}, and $\varepsilon_{hx} > 80\%$.
- identification of narrow-channel, fluidized bed receiver design and flow conditions that achieve average $h_{T,w} \geq 1000$ W m^{-2} K^{-1} at $T_{p,out} \geq 720°C$.
- specification of oxide particles that sustain mass loss rates to fines of less than 1% per year of operation in a primary HX flow path.
- Technoeconomic analysis showing full-scale receiver and TES subsystem that meet DOE cost targets.

The project has had three budget periods with milestone objectives for each period related toward furthering the development and confidence of narrow-channel fluidized beds for means of utilizing inert particle TES in CSP plants. Unforeseen challenges in experimental testing primarily delayed the program objectives for the first two budget periods and in some cases, aggressive Milestones have not been fully met. The list here lays out key program Milestones for each budget period.

- Budget Period 1 (from February 2019 to April 2020):

  - measuring $h_{T,w}$ in a narrow-channel fluidized bed ≥ 0.25 m high with wall area > 0.025 m^2 for T_p up to 600°C to develop Nusselt number correlations.
  - model results for 40-kW_{th} primary HX operation with gas-to-particle mass flow ratios < 2%, average $h_{T,w} \geq 1000$ W m^{-2} K^{-1}, and $T_{p.out}$-$T_{CO2,in} < 30$°C.
- Budget Period 2 (from May 2020 to February 2022):
  - demonstration in a fluidized bed ≥ 0.25 m-high, a flow path for stable primary HX operation with $h_{T,w} \geq 1000$ W m^{-2} K^{-1} at $T_{p,in}$ up to 600°C.
  - 100-h tests at $T_p \approx 500$°C showing minimal wear on oxidized bed walls and minimal particle attrition.
  - design and assembly of a stainless-steel, fluidized bed particle-sCO_2 HX capable of transferring 40-kW_{th} with particle flow variation of ± 10%.
- Budget Period 3 (from March 2022 to March 2023):
  - stable operation of a narrow-channel, fluidized bed HX transferring 40 kW_{th} with $T_{p,in} > 500$°C, overall drop in $T_p \geq 150$°C, and $\varepsilon_{HX} > 80\%$.
  - demonstration in a lab-scale fluidized bed ≥ 0.25 m-high, a scalable flow path for indirect receiver operation with average $h_{T,w} \geq 1000$ W m^{-2} K^{-1} at $T_{p.out} \geq 600$°C.

The testing and model development in this project provided tools for scaling up narrow-channel fluidized bed concepts into a prototype demonstration, 40-kW_{th} particle-sCO_2 fluidized bed HX that was tested in the particle-sCO_2 HX test facility at Sandia's NSTTF. Analysis of a TES subsystem that relies on fluidized bed HX provides direction for possible further research and development of particle-sCO_2 HXs and indirect receivers for implementation in full-scale CSP plants.

1.4. Project schedule and summary of results

Three one-year budget periods for the project were originally planned for the project, but delays due to funding, inability to meet early milestones, and the Covid-19 pandemic limiting lab access caused the project to extend to 3 budget periods over 4 years. The progress is summarized chronologically for each budget period, but the detailed reporting is broken into four major thrusts, which spanned all budget periods as indicated in Fig. 2.

In Budget Period 1, Mines established a lab-scale, single-channel fluidized bed heat transfer rig with sufficient height ($\Delta y_b \approx 25$ cm) and instrumented walls to extract $h_{T,w}$ at multiple bed locations. The experimental studies provided particle-wall $h_{T,w}$ as a function of excess fluidization velocity for two CARBO particles (HSP 40/70 and CP 40/100) for temperatures, T_p up to 500°C but did not achieve the Milestone of $h_{T,w} \geq 1000$ W m^{-2} K^{-1}. The extensive data was fit to convective Nusselt correlations in the vein of Molerus [20, 22], which provided a basis for developing reduced-order 1-D fluidized bed models of a particle HX and indirect particle receiver adopted from previous models in the literature [42-44]. The initial modeling efforts did not account for thermal energy dispersion

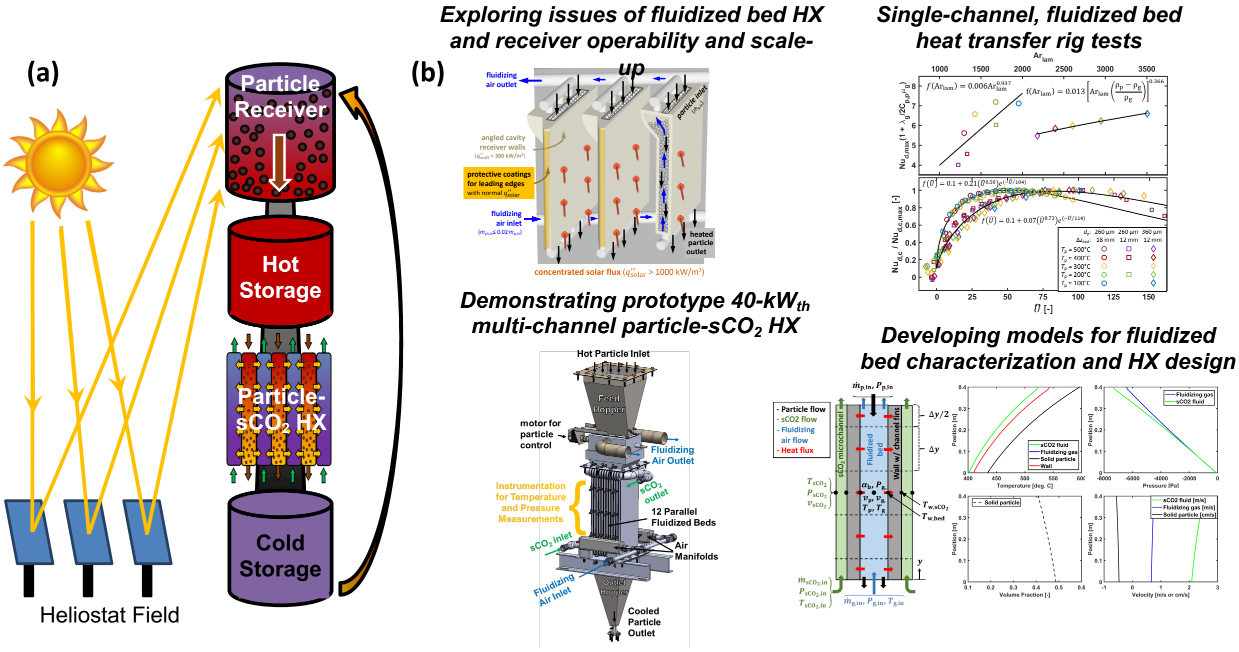

Figure 2: a) Schematic of a central CSP tower with a vertical particle flow path for TES subsystem using fluidized beds for the solar receiver and the particle-sCO$_2$ HX; b) summary images highlighting key tasks in project designed to address design and feasibility issues of fluidized bed for particle HXs and receivers for TES subsystems.

in the bed due to fluidization but did point to how an average $h_{T,w} \geq 1000$ W m^{-2} K^{-1} could be reached for $d_{p,mean} < 250$ μm and $\dot{m}_{g,in}/\dot{m}_{p,in} < 2\%$ at $T_{p,in} \approx 600$°C. Finally, in Budget Period 1, dip-coating methods were explored for depositing passive oxide barriers to reduce solar loads on leading edges of indirect, fluidized-bed particle receivers through optical and thermal spreading of concentrated solar fluxes.

In Budget Period 2, the team gathered more heat transfer data in the single-channel test rig at Mines with CARBOBEAD particles for T_p up to 520°C. The results led to updated $h_{T,w}$ correlations [45], which were used in the 1-D HX models to design a multi-channel particle-sCO$_2$ HX with similar structure to Sandia's moving packed bed designs [10, 46]. Mines worked with Sandia and Vacuum Process Engineering (VPE) to build a nominal 40-kW$_{th}$ fluidized-bed, particle-sCO$_2$ HX for testing at Sandia's NSTTF particle-sCO$_2$ HX facility. VPE diffusion-bonded stainless-steel plates etched with sCO$_2$ microchannels and flow distribution manifolds, and bonded spacer frames between the plates to form 12 parallel fluidized-bed channels in the HX. Mines designed and built the balance of plant include a particle-feed wedge hopper, an exit hopper, and a unique rotating scoop to control inlet particle flow from the feed hopper into a freeboard zone above the multi-bed HX core. Room-temperature fluidization tests with HSP 40/70 in the multi-bed HX showed but uniform solid volume fractions α_b across the 12 parallel bed channels were sustained by keeping a layer of fluidized particles in the freeboard zone. Continued development of oxide coatings for receiver leading edges explored porous CuCr$_2$O$_4$ spinel coatings on oxidized metal alloys, but this effort was terminated after Budget Period 2 to focus resources on the particle-sCO$_2$ HX demonstration.

For Budget Period 3, the single-channel test rig at Mines was updated to simulate receiver-like conditions and added temperature and pressure measurements in a freeboard zone above the core to evaluate axial dispersion during continuous particle flow testing. Multiple 100-h fluidized bed tests at $T_\mathrm{p} \approx 500°\mathrm{C}$ measured wear and abrasion on oxidized stainless steel 304 and Haynes 230 wall coupons. The tests showed minimal surface oxide abrasion rates in the mild bubbling, fluidized bed HX environment. In Budget Period 3, the 40-kW$_\mathrm{th}$ particle-sCO$_2$ HX was tested at NSTTF over a range of particle, gas, and sCO$_2$ flow conditions. The tests demonstrated targeted heat transfer to the sCO$_2$ $\dot{Q}_\mathrm{HX} > 40$ kW$_\mathrm{th}$ for $\dot{m}_\mathrm{p} = 0.240$ kg s^{-1}. However, axial dispersion in the fluidized bed (as indicated by the difference in $T_\mathrm{p,in}$ and particle freeboard temperature $T_\mathrm{p,fb}$) lowered the effective particle-sCO$_2$ log-mean temperature difference and overall $U < 200$ W m^{-2} K^{-1} below targeted Milestone values. The demonstration HX testing at Sandia did not meet all milestones in part due to limitations on $T_\mathrm{p,in} < 520°\mathrm{C}$, because Mines inlet hopper design caused uneven flow in Sandia's particle electric preheater. The HX tests motivated updates to the reduced-order models of the fluidized bed HX and indirect particle receiver by incorporating axial dispersion. The updated models were used to study particle-sCO$_2$ HX integration into a TES subsystem to assess tradeoffs between increased parasitic loads and improved heat transfer associated with fluidization gas flows. These models have been integrated with an RCBC sCO$_2$ power cycle model [47, 48] to assess how performance of a fluidized bed particle-sCO$_2$ HX impacts the feasibility of a full-scale, particle-based TES subsystem meet DOE performance and cost targets.

Detailed summaries of task results are broken up into the four major thrusts listed here with the relevant tasks (numbered by Budget Period) shown beneath the listed thrust.

- ***Single-channel, fluidized bed heat transfer tests***
  - *Task 1.1: Lab-scale tests to identify HX operating regimes and flow paths*
  - *Task 2.0: Lab-scale tests to verify HX operation and particle-wall wear*
  - *Task 2.3: Lab-scale tests to assess preferred receiver particle and gas flow*
  - *Task 3.0: Further lab-scale tests to assess receiver particle and gas flow paths*
- ***Exploring issues of fluidized bed HX and indirect particle receiver operability***
  - *Task 1.2: Designing particle properties for optimal fluidized bed HX performance*
  - *Task 2.4: Optimizing particle manufacturing for low-cost and low abrasion rates*
  - *Task 1.4: Exploring passive solutions for receiver tip thermal management*
  - *Task 2.5: Identifying passive solutions for receiver tip thermal management*
- ***Developing models for fluidized bed characterization and HX design***
  - *Task 1.3: Development/validation of models for fluidized bed HX design*
  - *Task 2.1: 1-D and 3-D modeling of particle-sCO$_2$ HX design.*
  - *Task 3.1: 1-D and 3-D modeling of receiver design.*
- ***Demonstrating prototype 40-kW$_{th}$ multi-channel particle-sCO$_2$ HX***
  - *Task 2.2: Demonstrating 40-kW$_{th}$ stainless-steel particle-sCO$_2$ HX*
  - *Task 3.2: Technoeconomic analysis of heat exchanger and TES subsystem.*

Results reported below focus on major findings tied to Milestones as well as unexpected findings that concern the viability of narrow-channel fluidized beds to meet DOE cost targets. Intermediate progress is highlighted when it is critical for explaining challenges or critical decisions in technology development. Several presentations of this work have been given at numerous conferences, and multiple publications on this work, beyond the first one [45], are in preparation for submission this year to disseminate analysis of fluidized bed heat transfer and practical insight about HX and indirect receiver design.

2. Single-channel, fluidized bed heat transfer tests

Much of the experimental research in this program centered around a single narrow-channel fluidized bed heat transfer test rig at Mines. The test rig which went through numerous upgrades throughout the project was used to collect extensive particle-wall heat transfer data for CARBOBEAD CP 40/100, HSP 40/70, and HSP 45/60. These particles were provided generously by CARBO Ceramics in support of this program, and some of the most critical properties for the particles are provided in Table 1. The rig in its primary operation consisted of a single narrow channel 12 or 18 mm in depth for this study wherein particles were fluidized. The channel was surrounded by walls with ungrounded, sheathed K-type thermocouples to measure temperature differences between the external and internal surfaces ($T_{w,ext} – T_{w,int}$) and thereby assess local wall heat fluxes, q_w as a path to evaluating $h_{T,w}$. Heat transfer measurements were conducted in two modes:

- *batch particle mode* with no net vertical particle flow and one channel wall was externally heated with a bank of near IR quartz lamps and the other wall was cooled with external fans to keep the rig at a near constant bed temperature T_b.
- *continuous flow mode* where the particles flowed downward counter to fluidizing gas with both channel walls either heated with near IR quartz lamps or cooled with external forced convection on the outer wall surfaces.

Mines installed a 6 kW$_{elec}$ bank of near-IR quartz lamps with controllers from Fannon Electric to provide uniform heating of an instrumented wall at fluxes up to 250 kW m^{-2}. Measurements in both modes provided a basis for developing convective Nusselt number correlations ($Nu_{pc} = h_{T,w,conv}\, d_p/\lambda_g$, where λ_g is the gas thermal conductivity and $h_{T,w,conv}$ is the convective portion of the total particle-wall $h_{T,w}$, which includes radiation transfer). Experiments in both batch particle mode without particle flow in and out of the channel as well as continuous particle flow gave comparable $h_{T,w}$ at otherwise similar operating conditions and as such, the simpler batch mode operation was employed for more extensive measurements. New Nu_{pc} correlations, reported here and soon to be published, improve upon past correlations from work at Mines [34, 45].

Table 1: Particle physical and thermodynamic properties with densities taken from CARBO Ceramics spec. sheet and measured Sauter mean diameter from PSA at Mines and cp measurements from literature [7]

Particle type	ρ_p [kg m^{-3}]	$\alpha_{p,max}$ [--]	Quoted $d_{p,mean}$ [μm]	Meas. $d_{p,mean}$ [μm]	$c_{p@400°C}$ [J kg^{-1} K^{-1}]
CARBOBEAD CP 40/100	3270	0.575	260	304	1053
CARBOBEAD HSP 45/60	3620	0.567	287	333	1063
CARBOBEAD HSP 40/70	3620	0.567	360	408	1063

2.1. Single-channel fluidized bed heat transfer test rig design

The single narrow-channel fluidized bed heat transfer test section assembled at Mines had a bed height, $\Delta y_b \approx 0.25$ m (from gas injector to freeboard zone) and width, $\Delta x_b = 0.10$ m) to assess particle-wall heat transfer over a scale comparable to those expected in a multi-kW heat exchanger or indirect particle receiver. Mines 3-D printed narrow-channel frames out of Inco 718 of two different bed depths for the heat transfer test section. Machined stainless steel (SS304) flat plates with embedded thermocouples for wall heat flux, q_w measurements at 6 different locations (3 each along the heights on the right and left side of beds as shown in Fig. 3), were bolted on opposing sides of the 3-D printed frames with carbon graphite sealing gaskets between the side walls. The channel frames with graphite gaskets provided two different bed depths (Δz_b of 12 mm and 18 mm). An alternative side wall consisted of an SS304 frame for a fluorinated tin oxide (FTO) conductive glass window as shown in the photo of Fig. 3, which allowed for flow visualization at temperatures, T_p up to 250°C as shown in Fig. 4. Side ports in the channel frame at the bottom of the test section for inserting a 6.35 mm OD tube (with 0.5 mm wall thickness) for fluidizing gas injection. The injector tube, which had 126 evenly spaced holes of diameter, $d_{inj} = 127$ µm aligned to point vertically upward, provided fluidizing air to the heat transfer section. Other injector tubes were tested with thin slots and alternative hole arrangements, but the fluidized bed heat transfer was not found to be very sensitive

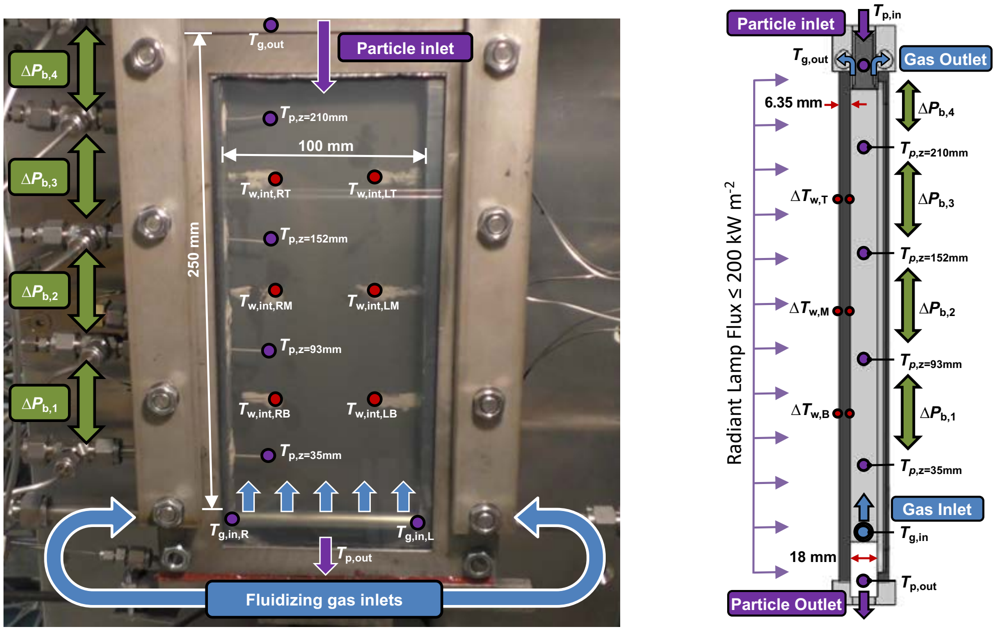

Figure 3: Photo and sideview schematic of heat transfer section with FTO window for flow visualization showing the 6 internal wall TC locations, injector, and particle inlet and outlets at the top and bottom of the channel. The back wall is irradiated by near-IR lamps. Thermocouples embedded in grooves of the external and internal wall surface of the heated plate provide a measure for heat flux through the plate on the right (R) and left (L) sides of the plate at heights above the gas injector of 62 mm (B), 120 mm (M), and 178 mm (T). Bulk particle temperatures T_p are measured in the channel at 35 mm, 93 mm, 152 mm, and 210 mm above the gas injector.

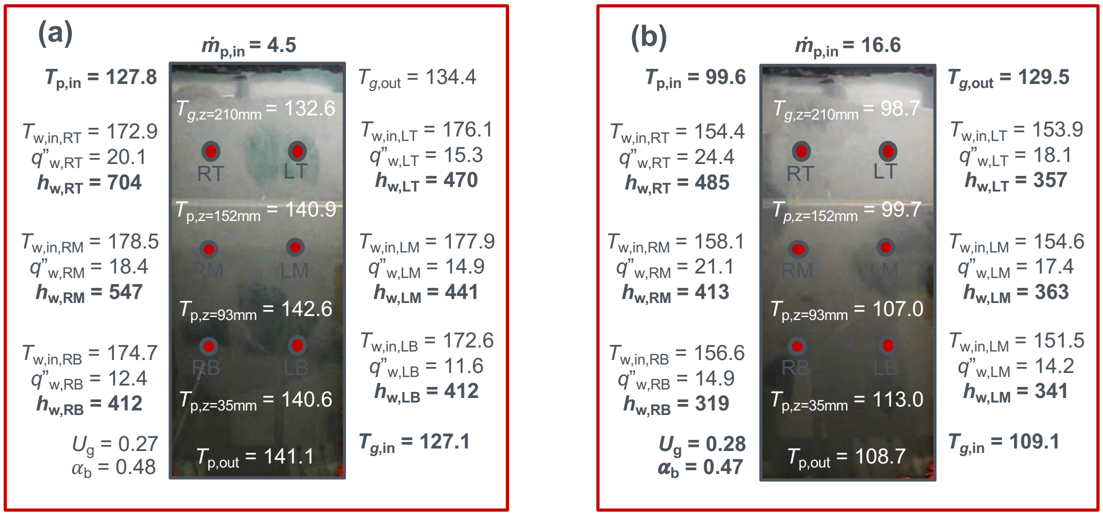

Figure 4: Particle and wall temperatures (in °C), heat flux q'' (in kW m^{-2}), and $h_{T,w}$ (in W m^{-2} K^{-1}) for particle mass flow rates 50% and 170% of design particle mass flux at $T_{p,in}$ from 95 to 132°C at U_g = 0.27 m/s ($\hat{U}$ = 30).

to the injector design. The side frame had four locations for inserting 1.6 mm sheathed K-type thermocouples through a fitting, which also provided access for pressure measurements along the height of the bed (as shown in Fig. 3).

Four gas pressure taps for P_g with fittings for thermocouples to measure local T_p provided data to assess both solid volume fraction α_p and $h_{T,w}$ as a function of height in the bed. Pressure drops, Δp_g between the taps gave mean values for mean α_p over the distance between the taps.

$$\alpha_{\mathrm{p},\Delta y} = \frac{\Delta p_{\mathrm{g},\Delta y} - \Delta y \rho_{\mathrm{g}} g}{\Delta y (\rho_{\mathrm{p}} - \rho_{\mathrm{g}}) g} \qquad \text{(eq. 1)}$$

The measurements of $T_{w,ext} - T_{w,int}$ at six locations as shown in Fig. 3 on the side wall plates provided a means for assessing variations in local heat wall flux q_w and $h_{T,w}$ over the height and width of the bed according to eq. 2.

$$h_{\mathrm{T,w}} = \frac{q_{\mathrm{w}}}{\left(T_{\mathrm{w,int}} - 0.5(T_{p,+} + T_{p,-})\right)} = \frac{\lambda_{\mathrm{w}}/\Delta z_{\mathrm{w,TC}}\,(T_{\mathrm{w,ext}} - T_{\mathrm{w,int}})}{\left(T_{\mathrm{w,int}} - 0.5(T_{\mathrm{p},+} + T_{\mathrm{p},-})\right)} \qquad \text{(eq. 2)}$$

$0.5(T_{\mathrm{p},+} + T_{\mathrm{p},-})$ in eq. 2 represents a mean bed temperature at the height of a q_w measurement based on mean T_p above and below the wall measurement location. Eq. 2 is most sensitive to $T_{w,int}$, which impacts both the numerator and denominator. Care was taken to ensure that $T_{w,int}$ measurements were reliably measuring the internal wall temperature before including a local $h_{T,w}$ value in the assessment of Nu_{pc} correlations. Fig. 4 shows examples of measurements at relatively low T_p < 150°C for flow visualization during which the bed was externally heated on one wall only and operated in continuous mode at two different particle mass flow rates $\dot{m}_{p,in}$ with flow visualization.

The single-channel test rig received various upgrades throughout this project to improve operational capability and measurements. For example, a new sliding gate mechanism with computer-controlled, stepper-motor actuation (Teknic CPM-MCPV) was installed for better control of particle inlet and outlet flows during continuous flow operation. In Budget Period 2, a new single-channel heat transfer rig, as illustrated in Fig. 5a showing the external quartz lamp heating on one wall, was fabricated, and installed for testing higher T_p with an improved test section design illustrated in the drawings in Figs. 5b and 5c. The new test section improved the gas-particle separation above the channel test region with a wider freeboard zone above the channel that reduced the superficial gas velocity U_g above the rig and lowered the fluidization intensity in the freeboard zone for better gas-particle separation. The gas exited through a fine SS304 mesh above the freeboard zone, which kept the particles in the test section. The freeboard zone permitted fluidization over the entire height of the test section for better assessment of variations in $h_{T,w}$ as a function of channel height. This test section also provided a shallower angle exit beneath the injector to eliminate risks of non-fluidized zones near the bottom of the test section.

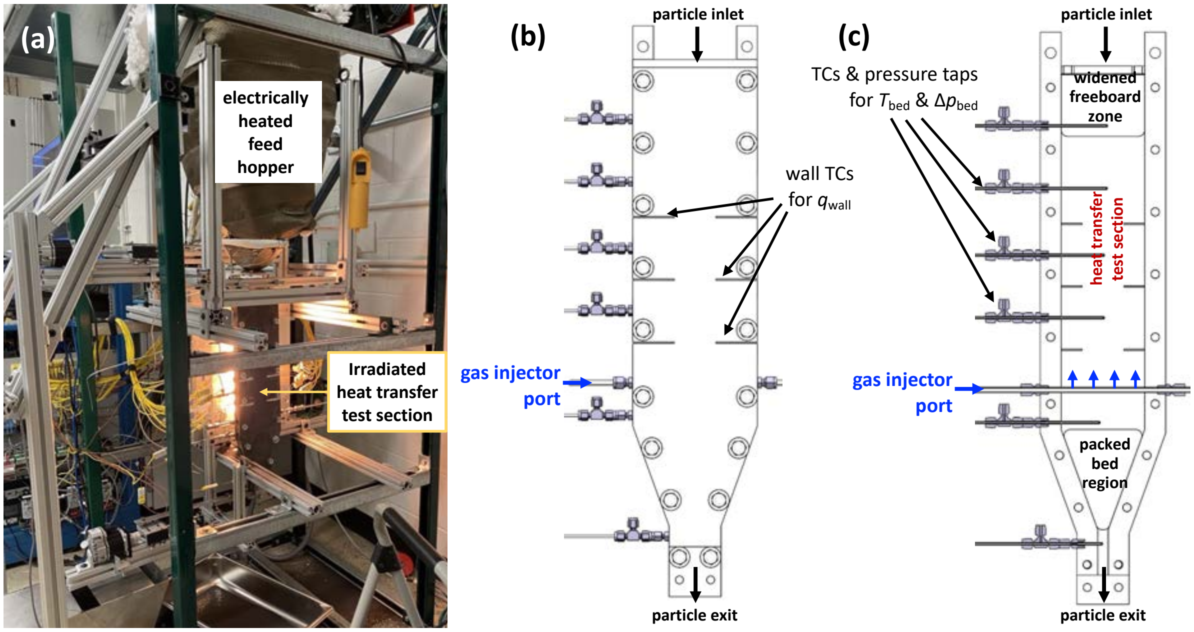

Figure 5. a) Photo of the new heat transfer rig with the near-IR lamp bank heating one external wall of the test section. b) Drawing of test section external surface showing location of wall thermocouples for local wall heat fluxes. c) Drawing of test section internal flow path with measurement locations for T_p and gas pressure Δp_g.

For continuous particle flow measurements, the particle feed system used a previously fabricated, electrically heated feed hopper (shown in Fig. 5a) from the CSP ELEMENTS project [49] and a new particle collection hopper. The collection hopper sat on a load cell for mass flow measurements. The initial rig relied on an electric winch to lift a full collection hopper along a track up above the feed hopper, where the particles were dumped, and recycled back into the electrically heated feed hopper. The feed hopper was upgraded with a total of 12 cartridge heaters (split tube heaters from Dalton Electric Heating) that occupy 5 different temperature zones with independent thermal control. Two smaller trim heaters about 75 mm above the hopper exit to the fluidized bed test section provided rapid response heating near the hopper exit to support finer control of $T_{p,in}$. A full hopper can be heated above 300°C in less than one hour. The improved hopper heating and controls enabled the hopper to reach $T_{p,in} > 500°C$, but not the target 600°C.

To support continuous particle flow testing for longer periods of time, the winch was replaced with a novel pneumatic particle recycling system that sucks particles up from the outlet collection hopper through a stainless-steel tube and into a separation cyclone before subsequent release back into the feed hopper. Figure 6a shows a photograph of the updated rig with the flow paths of the air and particles shown in the recycler. To facilitate return of hot particles at very high $T_{p,out}$, the recycle flow path for the particles is constructed entirely of stainless steel including the particle-gas cyclone separator and the intermediate storage hopper which holds the recycled particles until the vacuum is deactivated and a gate valve opens to drop the particles back into the insulated, electrically heated feed hopper. To support $\dot{m}_p$ measurements, the recycling system was only run intermittently at much higher particle flow rates than the $\dot{m}_p$ through the test section. Desired recycle flow rates, $\dot{m}_r$ around 200 g s^{-1} were achieved by developing a unique outlet collection hopper as illustrated in Figure 6b. The hopper has a wall with an opening slot at its bottom that feeds particles to the inlet of the recycle tube such that the

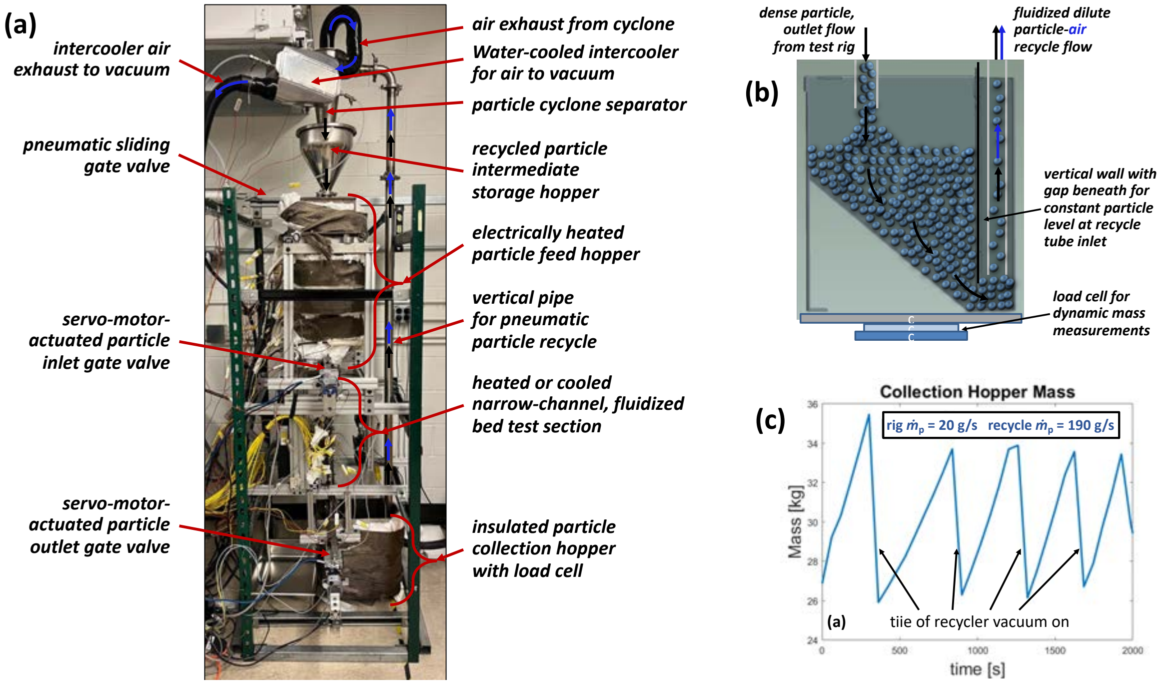

Figure 6: a) Single-channel, fluidized bed heat transfer test rig with upgrades including servo-motor-actuated gate valves for particle inlet and outlet flows and the particle recycler with pneumatic suction up through a cyclone particle-gas separator for returning the particles to the feed hopper. b) Illustration of outlet collection hopper showing separating wall that allows particles to be fed underneath it to the base of the recycler tube where they are sucked back up to the top of the rig and the particle-gas recycler. c) Plot of the collection hopper mass during a test with particle flow rate $\dot{m}_p$ = 20 g s^{-1} and the recycled particle flow rate $\dot{m}_r$ = 180 g s^{-1}. The mass rose when the vacuum was off and declined when the vacuum was activated.

negative pressure from the vacuum could consistently supply adequate $\dot{m}_r$. Figure 6c plots the mass of the collection during a 30+ min period of heat transfer rig operation. The periods of rapid mass drop are when the particle recycler is sucking particles out of the outlet hopper. To facilitate recycling, the air flow that is separated from the particles in the cyclone above the rig is cooled with an air-water intercooler to allow for the use of a standard shop vacuum. This rig remains functional and supports ongoing SETO-funded projects studying particle HX with Brayton Energy and particle receivers with NREL.

2.2. Single-channel fluidized bed heat transfer test results and analysis

Initial experiments in the earliest single-channel test rig tested fluidized CARBOBEAD CP 40/100 in both continuous flow and batch mode at mean bed temperatures T_p up to 420°C and superficial gas velocities U_g up to 0.75 $\mathrm{m\,s^{-1}}$. These measurements were complemented by a large number of $h_{T,w}$ measurements using CP 40/100 particles and larger HSP 40/70 particles in batch mode for $T_{p,in}$ up to 500°C as reported in a SolarPACES paper [45]. Eq. 2 for overall $h_{T,w}$ from the measurements provided a basis for analyzing how various parameters including T_p, $\dot{m}_p$, and excess fluidization velocity characterized by the non-dimensional $\hat{U}$ as defined in Molerus [20]

$$\hat{U} = (U_g - U_{mf})(\rho_p c_{p,p}/\lambda_g g)^{1/3} \qquad \text{(eq. 3)}$$

where U_{mf} is the minimum fluidization velocity derived from the Ergun equation, and ρ_p, $c_{p,p}$, λ_g, and g are the particle density, particle specific heat, gas thermal conductivity, and acceleration due to gravity, respectively. U_{mf} is on the order of 0.08 to 0.18 m/s for the CARBOBEAD particles tests with the magnitude decreasing with both T_p and d_p. For HSP 40/70, U_{mf} drops from 0.16 $\mathrm{m\,s^{-1}}$ at 100°C to 0.10 $\mathrm{m\,s^{-1}}$ at 500°C,

Early testing at $T_p < 300$°C utilized the conductive FTO window for flow visualization. Fluidized bed visualization as shown in Fig. 4 showed significant bubble coalescence as the bubbles rose through the narrow-channel bed. The bubble sizes increased with gas superficial velocities U_g. Mines proceeded with continuous particle flow heat transfer tests in the bed initially at lower $T_{p,in} < 250$°C (with the limits due to the FTO window for flow visualization). Early continuous flow experiments before the automated recycler system allowed for ≈ 45 min. at $\dot{m}_{p,in}$ = 9.4 $\mathrm{g\,s^{-1}}$ with the collection hopper capacity of approximately 30 kg. As such, there was value in taking data with batch mode testing for more rapid testing over a range of conditions. Steady-state operation in batch mode is achieved by matching heating on one wall with cooling to ambient on the other. Figure 7 compares batch mode and continuous-particle-flow mode $h_{T,w}$ measurements as a function of U_g for a range of T_p at all three heights in the test section. Scatter in the $h_{T,w}$ continuous-flow values likely arise from the increase in T_p as the particles are heated over the height of the bed. Nonetheless, similar $h_{T.w}$ for batch and continuous-flow bed operation at similar T_p suggests that the batch mode experiments provided a good measure of heat transfer performance with simpler and more rapid data collection.

Figure 8a shows typical measured bed-averaged $h_{T,w}$ from batch mode experiments as a function of $\hat{U}$ for HSP 40/70 particles in a bed with Δz_b = 12 mm. $h_{T,w}$ was calculated by eq. 2 from batch mode tests of the fluidized bed for T_p up to 500°C. $h_{T,w}$ has a shallow peak with respect to $\hat{U}$ near $\hat{U}$ = 75 ($U_g \approx 0.47$ $\mathrm{m\,s^{-1}}$ for $T_p \approx 500$°C), but a lower $\hat{U} \approx 40$

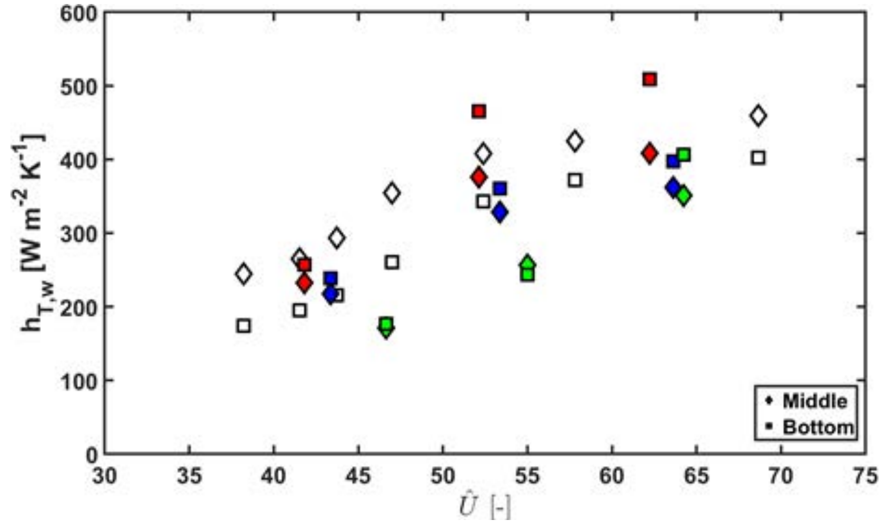

Figure 7: Measured $h_{T,w}$, vs. U_g for batch particle mode operation with average T_p = 121°C (open symbols) and continuous particle-flow operation (filled symbols) at the following flow conditions: red symbols: $\dot{m}_p$ = 4.5 g/s, $T_{p,in}$ = 128 – 144°C, blue symbols: $\dot{m}_p$ = 16.6 g/s, $T_{p,in}$ = 95 –118°C, green symbols: $\dot{m}_p$ = 9.4–10.3 g/s, $T_{p,in}$ = 21 – 82°C). The symbol shapes represent different locations above the gas injection in the bed: 62 mm (B), 120 mm (M), and 178 mm (T).

(i.e., $U_g \approx 0.30$ m s^{-1} at 500°C) can provide high $h_{T,w}$ > 90% of peak value with lower parasitic losses and reduced axial dispersion. The less dense, smaller CP 40/100 particles have U_{mf} that are≈ 50% of U_{mf} for HSP 40/70, and as such, required U_g for optimal $h_{T,w}$ with CP 40/100 is even lower. The shallow peak of $h_{T,w}$ at intermediate $\hat{U}$ arises because α_p decreases with increasing $\hat{U}$. Mean α_p calculated from eq. 1 decreases from its maximum value (Table 1) with increasing $\hat{U}$ and T_p. The shallow peaks in $h_{T,w}$ for these Geldart class B particles are consistent with earlier work [17, 19, 20] and suggests that mild bubbling fluidization provides optimal conditions for sustaining high $h_{T.w}$ while keeping parasitic loads low. In Figure 8a, the ratio of $h_{T,w}$ at $\hat{U}$ = 0 (≈ 100 W m^{-2} K^{-1}) to the peak value ≈ 570 W m^{-2} K^{-1} for T_p = 500°C demonstrates the potential for fluidization to lower particle-sCO$_2$ HX size and costs if axial dispersion can be mitigated, and high temperature differences maintained in the counterflow configuration.

To fit the measured data to a Nusselt number correlation, $h_{T,w}$ was broken up, as shown in eq. 4 into a particle-wall convective component $h_{T,w,conv}$, which was fitted to a correlation and a linearized radiative component $h_{T,w,rad}$, which was calculated as a gray body surface exchange assuming that the bed was optically thick.

$$h_{T,\mathrm{w}} = h_{T,\mathrm{w,conv}} + h_{T,\mathrm{w,rad}} = \frac{\mathrm{Nu_{pc}}\lambda_{\mathrm{g}}}{d_{\mathrm{p}}} + \frac{\sigma\left(T_{\mathrm{p}}^2 + T_{\mathrm{w,int}}^2\right)\left(T_{\mathrm{p}} + T_{\mathrm{w,int}}\right)}{\varepsilon_{\mathrm{w}}^{-1} + \varepsilon_{\mathrm{p}}^{-1} - 1} \qquad \text{(eq. 4)}$$

Analysis showed that $h_{T,w,rad}$ is below 5% of $h_{T,w}$ for T_p < 500°C [34], but becomes much more significant (> 10%) for T_p > 600°C. $h_{T,w,conv}$ dominates over the T_p range tested here.

Numerous $h_{T,w}$ measurements allowed for fitting a new Nu_{pc} correlation as a function T_p, $\hat{U}$, and particle and gas properties. $h_{T,w,conv}$ contributions from particle convection with the wall were evaluated and put into the dimensionless form as Nu_{pc} contributes where were then fit to forms following the work of Molerus [20, 22] where for Geldart type B particles as tested here, Nu_{pc} depends on laminar Archimedes number, Ar_{lam}, and the dimensionless excess superficial gas velocity $\hat{U}$,

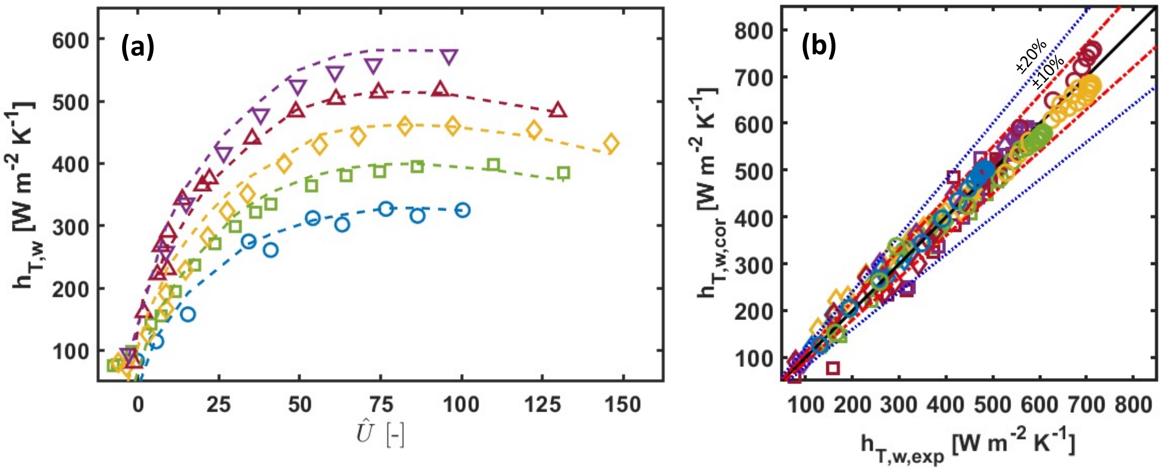

Figure 8: a) Measured average particle-wall $h_{\mathrm{T,w}}$ vs. non-dimensional excess fluidization velocity $\hat{U}$ for fluidized HSP 40/70 ($d_{\mathrm{p,mean}} \approx 408$ μm) in batch mode operation for a bed depth Δz_{b} = 12 mm and a range of average bed temperatures T_{p} up to 500ºC. Dashed curves show fitted correlations with radiation correction as a function of $\hat{U}$. b) Comparison of $h_{T,\mathrm{w}}$ calculated from correlation fits with radiation correction vs. experimental measured $h_{\mathrm{T,w}}$ for fluidized HSP 40/70 in narrow channels (Δz_{b} = 12 mm) and for fluidized CP 40/100 in different narrow channels (Δz_{b} = 12 mm and 18 mm) for average T_{p} up to 500ºC.

$$\mathrm{Nu}_{\mathrm{pc}}\left(1+\frac{\lambda_{\mathrm{g}}}{2c_{\mathrm{p.p}}\mu_{\mathrm{g}}}\right)=f(Ar_{\mathrm{lam}})f(\widehat{U}) \qquad \text{(eq. 5)}$$

$$Ar_{\mathrm{lam}} \equiv \sqrt{d_{\mathrm{p}}^{3}g(\rho_{\mathrm{p}}-\rho_{\mathrm{g}})}/\mu_{\mathrm{g}} \qquad \text{(eq. 6)}$$

Ar_{lam}, or an intermediate Archimedes number Ar_{int}, correlated more effectively with measurements depending on flow regimes (viscous/laminar, intermediate, or turbulent) [20, 22]. $f(\hat{U})$ was set to peak at 1.0 such that $f(Ar_{\mathrm{lam}})$ provides a measure for the peak Nu_{pc} as a function of T_{p} and d_{p} in a similar manner as Molerus [22]. The function form of $f(\hat{U})$ is given in eq. 7 where the constants are constrained for the maximum $f(\hat{U})$ = 1.0.

$$f(\widehat{U})=\left[c_{U,1}+c_{U,2}(\widehat{U})^{n_U}\exp(-\widehat{U}/c_{U,3})\right] \qquad \text{(eq. 7)}$$

During the first two years, a very large amount of data was collected for HSP 40/70 and CP 40/100 in single-channel beds of two different depths Δz_{b} = 12 mm and 18 mm. The data was used to derive fits for Nu_{pc} for each bed depth as shown in Fig. 9, which reveals that as Ar_{lam} increases with the larger HSP 40/70, there is a sudden transition in the dependence of $Nu_{\mathrm{pc,max}}$ on Ar_{lam} associated with a shift to a more turbulent particle heat transfer regime. This is consistent with Molerus approach although the transition here occurs at a higher $Ar_{\mathrm{lam}} > 2000$. Figure 9b show the dependence of $Nu_{\mathrm{pc}}/Nu_{\mathrm{pc,max}}$ vs. $\hat{U}$

for different d_p, T_p , and Δz_b. The data shows a consistent $f(\hat{U})$ for a fixed Δz_b over all the T_p. A functional form for $f(\hat{U})$ that fit $Nu_{pc}/Nu_{pc,max}$ as a function of $\hat{U}$ is given here.

Figure 9b shows two fits for $f(\hat{U})$, one for Δz_b = 12 mm and one for Δz_b = 18 mm, showed surprisingly reliable reproduction of the data with the fan plot in Fig. 8b showing that the correlation errors are within 10% of experimental $h_{T,w}$ except at the lowest values. $h_{T,w,conv}$ peaks at higher $\hat{U}$ for the deeper channel Δz_b = 18 mm, and the impact of Δz_b on $h_{T,w}$ remains a topic for further studies. Smaller Δz_b was shown to be critical for improving moving packed bed HX overall heat transfer [11, 18], and further studies with alternative injector designs to allow lower Δz_b can assess if similar benefits exist for fluidized bed HX. The fits in Fig. 9b were completed with the quoted nominal d_p values given in the legend.

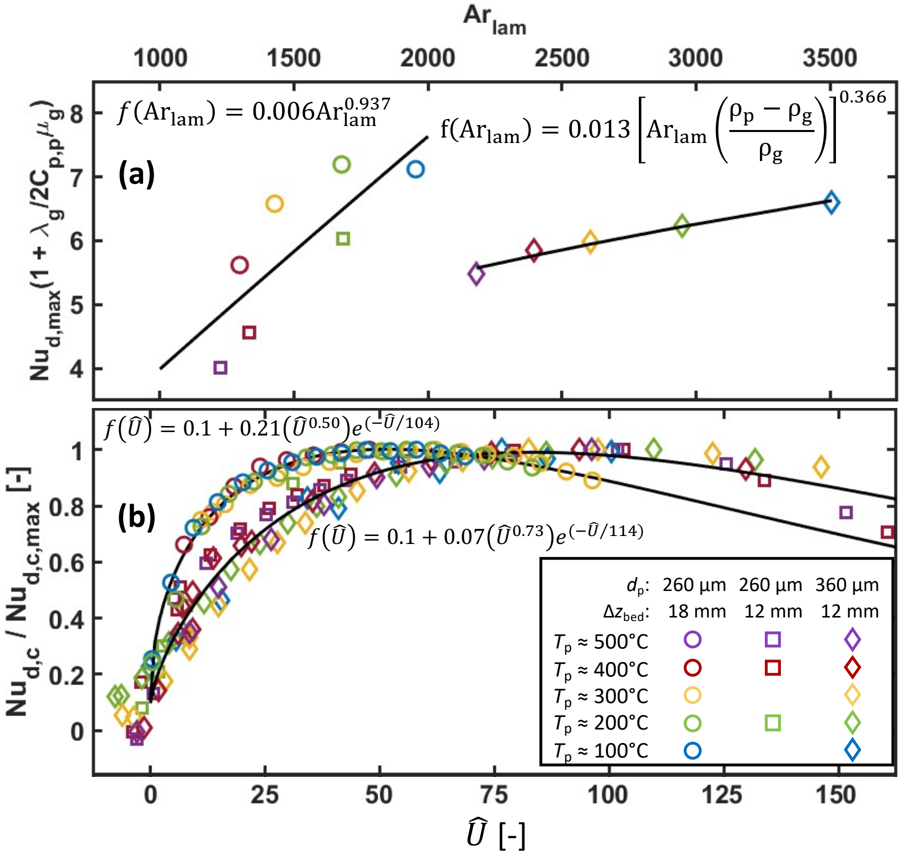

Figure 9: a) Fits of the maximum $Nu_{pc,max}$ as a function of Ar_{lam} for measured narrow-channel fluidized bed $h_{T,w}$ with CP 40/100 (nominal d_p = 260 µm, Ar_{lam} < 2000) and HSP 40/70 (nominal d_p = 360 µm, Ar_{lam} > 2000). The solid lines plot the two fitting functions for $Nu_{pc,max}$ vs. Ar_{lam} for the two particle regimes. b) $Nu_{pc}/Nu_{pc,max}$ vs. $\hat{U}$ for two Δz_b, CP 40/100 and HSP 40/70, and T_p up to 500°C. The curves and equations show the fits for $Nu_{pc}/Nu_{pc,max} = f(\hat{U})$.

Further improvements in the heat transfer rig over the last Budget Period led to revisiting the tests and additional batch mode testing of a larger range of particle sets including HSP 45/60 (properties in Table 1) which was the principal particle type tested in the demonstration HX. Smaller less dense SiO_2-based particles, notably AGSCO olivine

LE120 (measured $d_{p,\mathrm{mean}}$ = 160 μm, ρ_p = 3200 kg m^{-3}) and Covia silica W7020 (measured $d_{p,\mathrm{mean}}$ = 226 μm, ρ_p = 2650 kg m^{-3}), were also tested for the other programs but are shown here because there smaller size allows for the particles to meet the targeted milestone $h_{T,w}$ > 1000 W m^{-2} K^{-1} as shown in Fig. 10 for batch-mode, fluidized-bed heat transfer at $T_p \approx$ 450°C. The data in Fig. 10 shows that $h_{T,w}$ significantly increases with the smaller $d_{p,\mathrm{mean}}$ < 250 μm for olivine and silica with these particles showing $h_{T,w}$ > 1000 W m^{-2} K^{-1} even at 450°C. These values will go up further with T_p due to the increase in The data in Fig. 10 shows significant measurements below U_{mf} (i.e., $\hat{U} < 0$), where $h_{T,w}$ flattens out to a value similar to those measured in moving packed bed HX at similar conditions [46]. The flat $h_{T,w}$ at $\hat{U} < 0$ encouraged a revisiting of the $f(\hat{U})$ in the Nu_{pc} correlation where $c_{U,1}$ can now be interpreted as the fraction of the peak $h_{T,w,\mathrm{conv}}$ that is achieved at zero-fluidization.

$$f(\hat{U}) = \begin{bmatrix} c_{U,1} & \text{for } \hat{U} \leq 0 \\ c_{U,1} + c_{U,2}(\hat{U})^{n_U} \exp(-\hat{U}/c_{U,3}) & \text{for } \hat{U} > 0 \end{bmatrix} \quad \text{(eq. 8)}$$

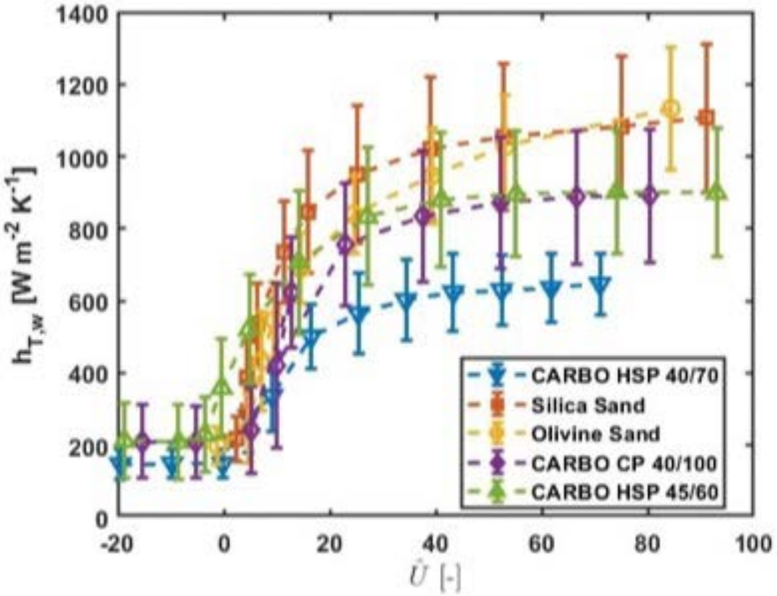

Figure 10: Plots of measured, bed-averaged $h_{T,w}$ vs. $\hat{U}$ for 5 different particles in a narrow-channel fluidized bed Δz_b = 12 mm operating in batch mode at a mean $T_p \approx$ 450°C. Magnitude of the error bars indicates the standard deviation of all wall measurements.

With the extensive measurements and with the new measured $d_{p,\mathrm{mean}}$, the new and old data for bed depth Δz_b = 12 mm were all consolidated into a new fit as shown in Fig. 11. The new data includes measurements from the olivine and silica particles for a broad range of $d_{p,\mathrm{mean}}$. The fits in Fig. 11 show that the peak $h_{T,w}$ which occurs around a $\hat{U}$ = 60 provides $h_{T,w}$ that are like 4× larger than the non-fluidized values. This provides a motivation for studying fluidized beds for enhanced heat transfer, but it does not address the challenge of axial dispersion in fluidized beds suppressing log-mean temperature difference (LMTD) and thus losing the advantage of higher $\underline{h}_{T,w}$. To this end, continuous flow tests with these particles were performed to assess axial dispersion.

Continuous flow experiments in the single-channel flow rig with the particle recycling and improved feed hopper heater controls. Tests were done with $T_{p,in} \approx 300°C$ in a HX mode where multiple fans provided cooling on both external walls of the narrow-channel bed.

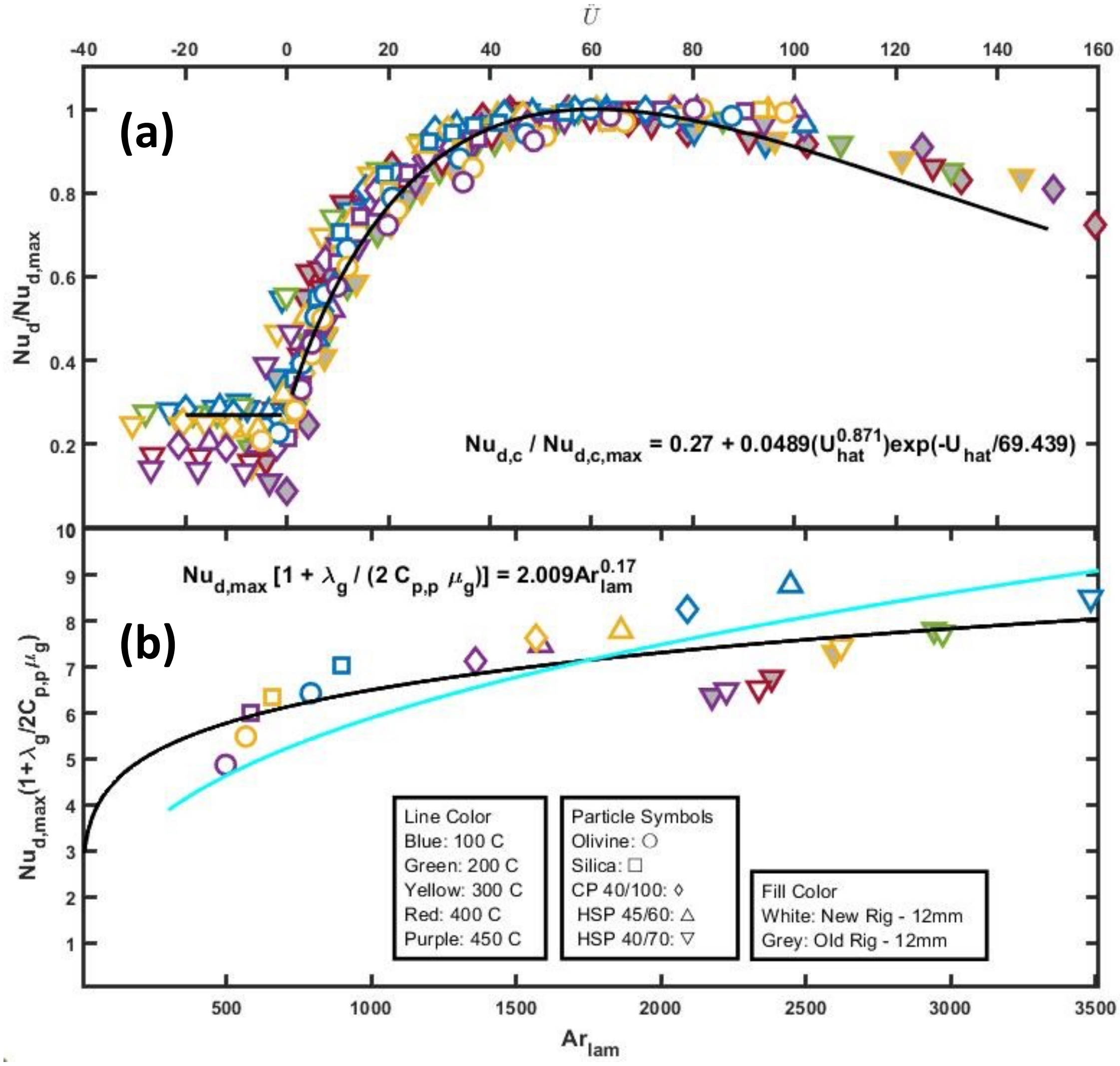

Figure 11: a) Local $Nu_{pc}/Nu_{pc,max}$ vs. $\hat{U}$ from -30 to 150 for 5 different particle types, CARBO HSP 40/70, CARBO HSP 45/60, CARBO CP 40/100, Covia silica W7020, and AGSCO olivine LE1200 over a range of T_p up to 450C. The correlation following eq. 8 is displayed with the black line. b) Dependence of $Nu_{pc,max}$ vs. Ar_{lam} for the 5 different particles for the same dataset in a). The black curve shows the current fit, and the blue curve shows the fit of Molerus [22], which closely follows the new data .

Examples of results are shown in Figure 12. Figure 12a presents T_p for different locations in the test rig including $T_{p,in}$ and $T_{p,out}$ as well as the central bed temperature $T_{p,mid}$. The drop in T_p with height begins in the freeboard zone where the difference $T_{p,in} - T_{p,fb}$ indicates that inlet particles are mixing with cooled particles rising up in the bed into the freeboard zone due to axial particle dispersion [50, 51]. The dispersion does lower the particle to cooling temperature driving force and thus reduces overall q_w from the particles, but the dispersion does not significantly impact average $h_{T,w}$ other than through changes

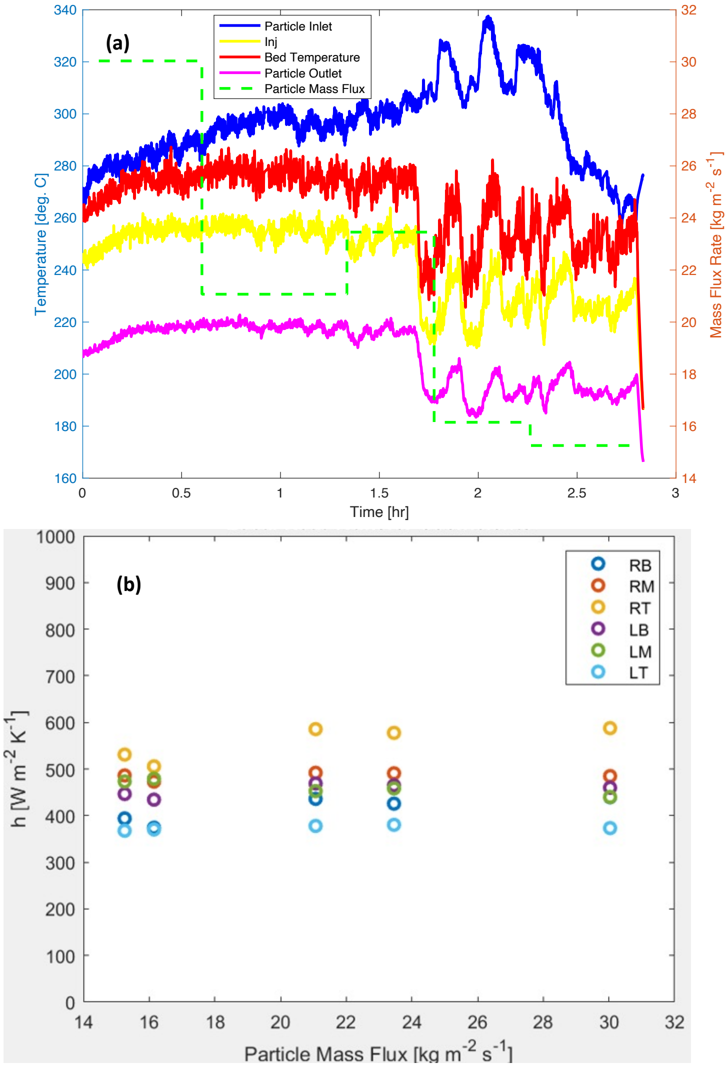

Figure 12: a) Measured particle temperatures (inlet, freeboard zone, middle bed in the single channel test rig with $T_{\mathrm{p,in}} \approx$ 300°C for various net particle mass fluxes through the $\dot{m}''_{\mathrm{p}}$. The gas mass flux is fixed where $\dot{m}''_{\mathrm{g}} \approx 0.18$ kg m^{-2} s^{-1}. b) Time-averaged $h_{\mathrm{T,w}}$ vs. $\dot{m}''_{\mathrm{p}}$ at the 6 instrumented wall locations within the fluidized bed (L – left, R – right, T – top, M – middle, and B – bottom) at $T_{\mathrm{p,in}} \approx$ 300°C and $\dot{m}''_{\mathrm{g}} \approx 0.18$ kg m^{-2} s^{-1}. Particles for both plots are CARBOBEAD HSP 40/70.

in the T_{p} profile vs. height. Figure 12b shows the time-averaged $h_{\mathrm{T,w}}$ at different wall positions, both left and right locations along the wall at the top, middle, and bottom of the bed. $h_{\mathrm{T,w}}$ is plotted vs. downward particle mass flux $\dot{m}''_{p}$ through the bed, and although the spread is as high as 200 W m^{-2} K^{-1} over the different positions, the limited variation in $h_{\mathrm{T,w}}$ at each position vs. $\dot{m}''_{\mathrm{p}}$ suggests that the reasonableness of the general supposition in our previous modeling of fluidized bed heat exchangers that $h_{\mathrm{T,w}}$ is largely independent of $\dot{m}''_{\mathrm{p}}$ [52]. The values of $h_{\mathrm{T,w}}$ between 380 and 600 W m^{-2} K^{-1} are because of the relatively low T_{p} in the bed relative to primary HX operating conditions. The gas mass flux in Fig. 12 was fixed at $\dot{m}''_{\mathrm{g}} \approx 0.18$ kg m^{-2} s^{-1} which is < 1% of the larger $\dot{m}''_{\mathrm{p}}$ values which meets the targeted $\dot{m}''_{\mathrm{g}}/\dot{m}''_{\mathrm{p}}$ ratios of < 2%.

Continuous flow experiments in the single-channel test rig provided critical insight into how increased axial solid-phase dispersion, often characterized by a vertical solid dispersion coefficient D_{sv} (units of m^2/s), which plays a significant role in fluidized bed HX T_{p} profiles and thus heat transfer performance. The classic reference by Kunii and Levenspiel [53] summarizes models for D_{sv} where for counterflow beds, typically D_{sv} is considered to vary nearly linearly with either upward gas bubble velocity or superficial gas velocity. A more recent study shows that D_{sv} can be derived from a near constant Peclet number based on excess fluidization velocity [54], which is of course proportional to $\hat{U}$. Increased D_{sv} with increased $\hat{U}$ tends to flatten bed particle temperature profiles which dampens the temperature driving force. This is illustrated by the different T_{p} and $T_{\mathrm{w,int}}$ vertical profiles in Fig. 13 for two continuous flow cooling tests at different $\hat{U}$ in the single-channel heat transfer rig. Although the higher $\hat{U}$ = 20 provides a higher hT,w value by about 100 W m^{-2} K^{-1} than $\hat{U}$ = 10, the increased dispersion at $\hat{U}$ = 20 flattens the Tp profile including lowering the $T_{\mathrm{p,fb}}$ which negatively the average q_{w} down the channel. As such the reduction in D_{sv} at lower $\hat{U}$ compensates for the lower hT,w by providing a higher average $T_{\mathrm{p}} - T_{\mathrm{w,int}}$ such that the two cases give very similar overall heat transfer.

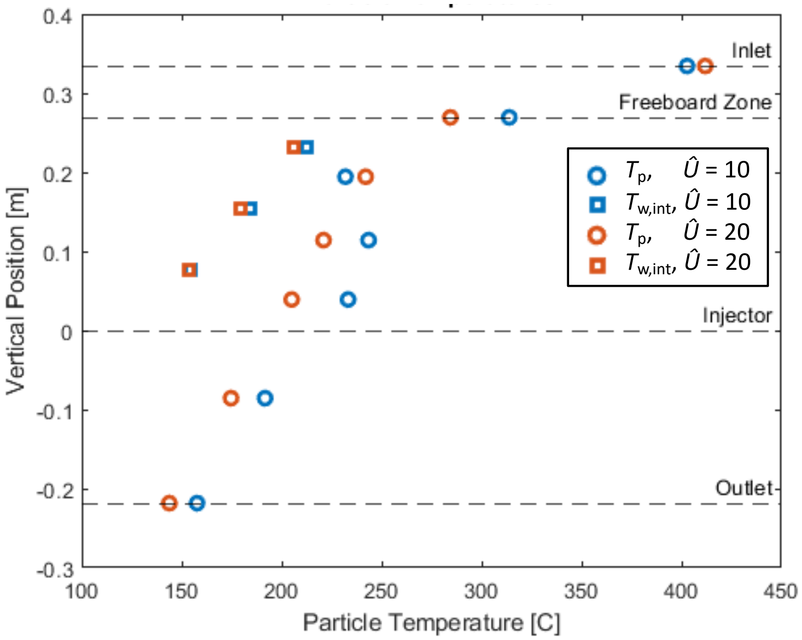

Figure 13: Vertical profiles of T_{p} and $T_{\mathrm{w,int}}$ for two continuous flow experiments in the single channel test rig at the same $T_{\mathrm{p,in}}$ = 400°C with CARBO HSP 40/70 flowing at the same $\dot{m}''_{\mathrm{p}}$ = 10 kg m^{-2} s^{-1} but different $\hat{U}$ = 10 and 20.

Efforts to establish a well characterized model for D_{sv} in fluidized bed models calibrated from the continuous flow experiments remains a critical work in progress for this study. The recent model where D_{sv} is assumed to model linearly with excess fluidization velocity [54] (i.e., $\hat{U}$) is being calibrated with measurements and will be discussed further with respect to the demonstration HX tests presented below.

2.3. Experiments on particle attrition and wall wear in fluidized beds

Bubbling fluidization may present challenges for particle abrasion and wall wear due to oxide scaling. Particle-wall wear testing of CARBOBEAD HSP 40/70 has shown that scaling and degradation of protective oxide layers are principal mechanisms for wall wear [41]. The oxide formed during oxidation in a quiescent furnace may differ significantly from subsequent oxides that form during wear at high temperatures [41]. To study the importance of this issue, one channel wall plate for the single-channel heat transfer test section was designed with cylindrical cavities to place wear coupons (19.75 mm in diameter, 1.86 mm thick) at four different locations on the inner wall (two at 5 cm above the gas injector and two at ≈ 15 cm above the injector). 100-h batch mode tests at T_p = 500°C were performed on the Haynes 230 (H230) and SS316 coupons.

Wear sample coupons were characterized before and after oxidation in air at 800°C for 12 h. The samples before and after surface oxidation were assessed for hardness with a 10 N force and 10 s dwell and Vickers hardness results. Surface oxidation improved hardness, but a principal mechanism for wear is likely to be oxide scaling, which may depend not only on the metal but also the temperature and time of the surface pre-oxidation. Mass and thickness measurements had a resolution of 0.0001 g and 0.001 mm, respectively. Surface roughness was measured with a MFP3D Atomic Force Microscope (Asylum Research) with the TAP190EG-10 tip in AC Air mode or with profilometry with a KLA Tencor D-600. 20 μm x 20 μm AFM scans were taken at three dispersed locations on each sample, and average roughness of each scan area was calculated from six 20 μm line profiles. A Tescan S8252G scanning electron microscope (SEM) or an FEI Quanta 600i Environmental SEM provided high-resolution views of surface features to assess wear impact on surface grain structure. EDX with the SEM provided surface oxide compositions and their evolution over wear tests.

Figure 14 shows photographs of the exposed surfaces of the coupons after two different 100-h including SS316 and H230 samples that were not initially oxidized and those that were. SS316 coupons show evidence of oxide scaling and significant discoloration. H230 samples, exhibited an iridescence after wear testing, but in general their appearance after testing is a dull brownish gray without evidence of scaling. Table 2 presents a summary of the results of the mass, thickness, and surface roughness measurements taken before and after the samples were worn under the 100-h fluidized bed test condition.

In general, mass measurement uncertainty was on the same order of magnitude as the mass change. SS316 samples in general gained around 1.0 mg of mass with the exception of pre-oxidized sample from the top of the bed which lost ≈ 2.0 mg. This loss may be attributed to oxide-layer scaling as this sample had the least thickness gain. Initially unoxidized SS316 coupons gained surface roughness with oxidation whereas pre-oxidized coupons lost surface roughness likely due to removal of high points in the original oxide layer. Even with T_p at 500°C, the relatively poor performance of SS316 as indicated by the surface finish in Fig. 14 suggests that alternative treatments are needed for SS316 wall long-term stability. The literature shows that heat treatments not only soften steels but can increase ductility and erosion resistance [55-57]. It is clear that the formation of a robust oxide layer on SS316 that may be produced in operando, a more thorough study beyond the scope of this work is required to address that.

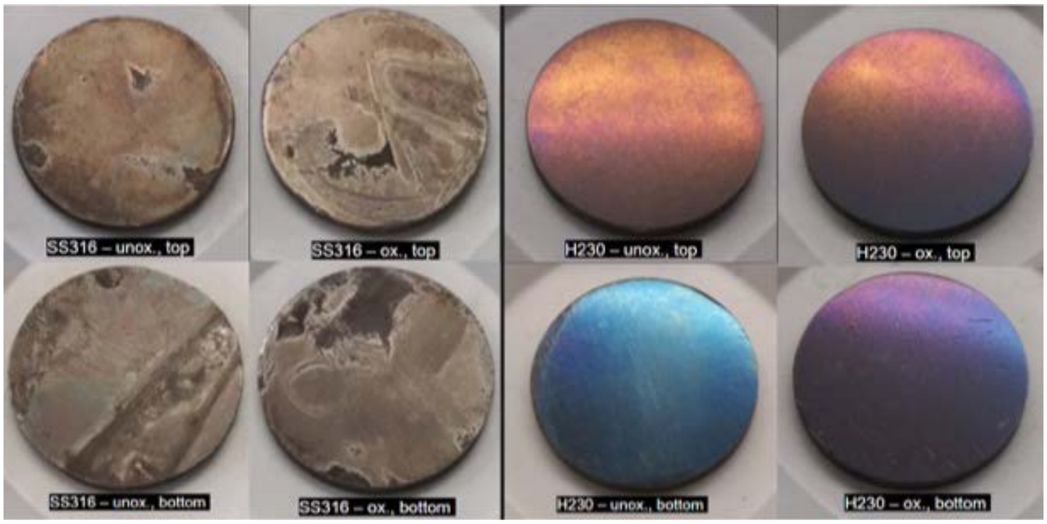

Figure 14: Photos of 8 coupon samples after 2 separate 100-h wear tests with particle bed temperatures $T_p \approx 500°C$. Coupons include 2 SS316 samples on far left were unoxidized before testing, and 2 SS316 samples in middle left were oxidized before testing, 2 H230 samples in middle right were unoxidized before testing, and 2 H230 samples on far right were oxidized before testing.

Table 2. Summary of mass, thickness, and surface roughness changes of coupons after 100-h wear tests in fluidized beds at $T_p \approx 500°C$
(*Averaged across 12 AFM scans (six each per sample) , ^{p} Profilometer data)

Sample ID, location in bed wall	Mass change Δm (mg)	Thickness change Δz (µm)	Surf. roughness $\Delta\varepsilon_w$ (nm)
SS316 - unox., top	1.0 ± 0.1	7.0 ± 4.0	2.0^p ± 2.8 CI
SS316 - unox., bottom	-2.1 ± 0.4	2.0 ± 3.0	2.5^p ± 3.9 CI
SS316 - ox., top	0.9 ± 0.2	11.0 ± 6.0	-1.1^p ± 2.2CI
SS316 - ox., bottom	0.6 ± 0.2	4.0 ± 4.0	-1.9^p ± 2.4 CI
H230 - unox., top	-3.9 ± 0.2	16.0 ± 7.0	-8.3 ± 6.8*
H230 - unox., bottom	-2.0 ± 0.1	10.0 ± 7.0	
H230 - ox., top	-4.6 ± 0.1	11.0 ± 9.0	-11.2 ± 6.1*
H230 - ox, bottom	-2.4 ± 0.1	6.0 ± 10.0	

Both oxidized and unoxidized H230 loss more mass than SS316 (still < 5.0 mg) but gained 6-16mm of thickness. This may indicate the growth of a low-density, porous oxide layer on the coupon surface. All the same, the mass loss, 0.7 – 15 mg/cm^2 over the 100 h, met the wear milestone target of < 0.02 mm/1000 h. The roughness of all the H230 samples decreased over time and the images in Fig. 14 indicate that bed exposure had a polishing effect on the H230 oxide surface.

SEM images shown in Fig.15 of the SS316 and H230 wear samples before and after testing indicate differences between the pre-oxidized and unoxidized (i.e., in operando oxidized) samples form surfaces. The SEM images reveal that the initially unoxidized surfaces tend to form a surface with similar form as the pre-oxidized for SS316 but with less surface irregularities for H230. The SEM is consistent with the reduction in surface roughness of the H230 after wear.

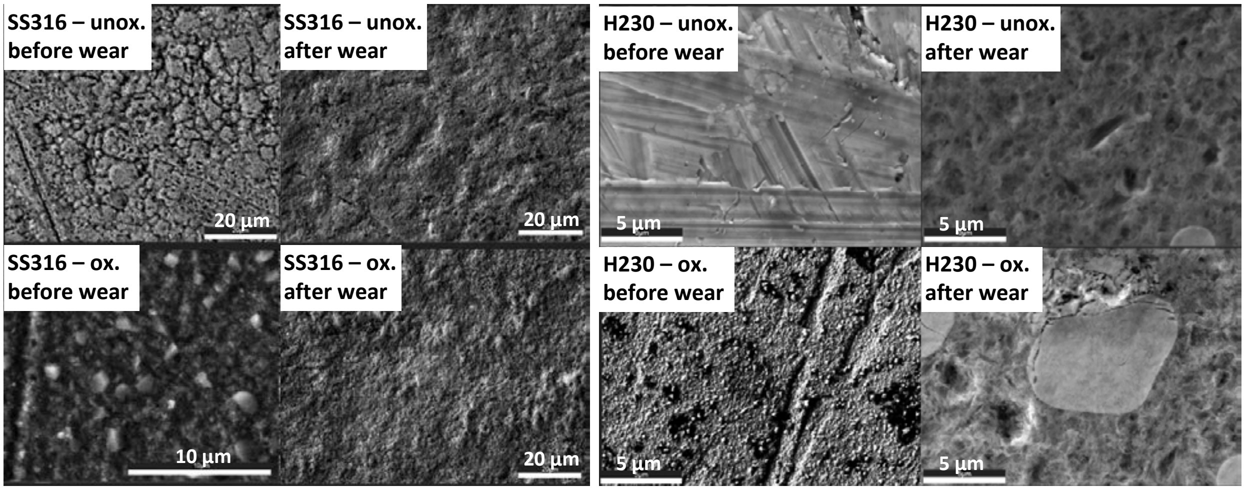

Figure 15: SEM images of the exposed surfaces of SS316 wear samples, both unoxidized and pre-oxidized before and after wear tests and H230 wear samples, both unoxidized and pre-oxidized before and after wear tests. These samples were mounted at the top of the heat exchanger. Note the different scales for the images.

EDX on the SS316 surface after wear showed two distinct phases:1) uniform in morphology, rich in Fe and O with moderate Cr and Mn levels and 2) Discrete extrusion rich in Al and O and deficient in Fe. These extrusions were likely due to abrasive fluidized Al_2O_3-dominant oxide particle fines embedding themselves into the SS316 surface [58, 59]. These embedded oxide particles may improve wear resistance but evidence of scaling on the SS316 oxide layer shown in Fig. 14 suggests that this may not be the case.

For H230, EDX revealed islands of a tungsten rich phase both in unworn and worn samples due to precipitates formed during original material production [60]. After wear testing of the oxidized sample, the base oxide and the tungsten-rich phase increased in cation content and decreased in O content. In general, the H230 shows removal of areas of high surface roughness, but the unoxidized phase shows less prominent features associated with the tungsten-rich phase. In general, the tests suggest that oxidation of H230 in a fluidized bed may produce the most robust oxide surface.

After wear testing, histograms of particle diameter distribution profiles shown in Fig. 16 suggest a loss of smaller particles, likely due to their escape through the mesh above the freeboard zone. There is evidence of particle fracture as the fresh particles had higher sphericity than worn particles. This could accelerate particle degradation due to the loss of roundness over time. In general, smaller particles not only improve $h_{T,w}$, but may reduce wear and particle fracture risks [39]. Tests with smaller HSP 45/60 may be beneficial to quantify reduction in wall wear and changes in d_p distribution.

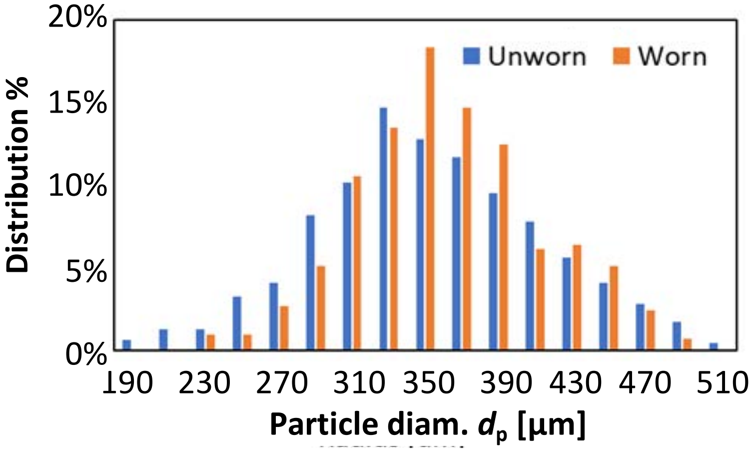

Figure 16: Particle diameter d_p histogram of CARBOBEAD HSP 40/70 before and after wear testing. The shift toward larger diameters in the wear tests is due to losses of smaller particles by their escaping through leaks in the mesh at the top of the rig.

3. Exploring issues of fluidized bed HX and indirect particle receiver operability

Many issues beyond just heat transfer are important for making fluidized beds a feasible solution for TES subsystems in CSP applications. For example, issues related to manufacturability and cost-effective scale-up of materials and designs are critical for making fluidized beds part of a viable pathway for future CSP. This program had specific tasks that looked briefly at two such issues related to: 1) optimal particle manufacturing and 2) indirect receiver passive coatings to protect leading edges of cavity indirect particle receivers. These small tasks are briefly summarized here.

3.1. Designing particle properties for optimal fluidized bed heat transfer

CARBO Ceramics (CARBO), Mines and Sandia discussed preferred particle properties for a TES subsystem using a fluidized bed HX. These discussions are informed by results from the SETO-sponsored work on particle wear at Boise State Univ. [41] and Sandia's Gen-3 particle pilot plant receiver heat exchanger and receiver [4, 46]. CARBO supplied Mines with 50 kg of both CP 40/100 and HSP 40/70 for testing and provided Sandia with 227 kg sacks of HSP 40/70 for the demonstration HX testing at NSTTF. CARBO developed new higher-density smoother particles and supplied Mines with 2 kg samples. These particles had a less than desirable $d_p \approx 450$ µm, which will reduce their effective $h_{T,w}$, but CARBO expects these smoother particles are more wear-resistant in a fluidized bed with better flow properties for inlet and outlet hoppers.

To hit the target particle-wall $h_{T,w} \geq 1000$ W m^{-2} K^{-1}, $d_{p,mean}$ must be < 250 µm (as suggested by Fig. 10). CARBO explored ways to adjust their particle manufacturing processes for the smoother particles to make $d_p < 250$ µm, but due to pandemic-driven, economic challenges CARBO's willingness to do that development under this project was limited. In the end, CARBO took standard HSP 40/70 and applied finer sieving to the baseline low-cost 40/70 material to produce a tighter particle size distribution (HSP 45/60) with a smaller measured $d_{p,mean} = 333$ µm (relative to 408 µm for HSP 40/70). The smaller HSP 45/60 demonstrated the same roundness/sphericity as the HSP 40/70 as shown in

Fig. 17 and a tighter d_p distribution than both CP 40/100 and HSP 40/70 as seen in Fig. 17d. As highlighted earlier in Fig. 10, the lower d_p of HSP 45/60 increased peak $h_{T,w}$ at T_p = 450°C to close to 900 W m^{-2} K^{-1} which is almost 50% higher than that of HSP 40/70. This is also achieved at lower fluidization gas flows due to lower $d_{p,mean}$. For these benefits, CARBO provided the 227 kg sacks of HSP 45/60 for the demonstration HX tests at Sandia as discussed below.

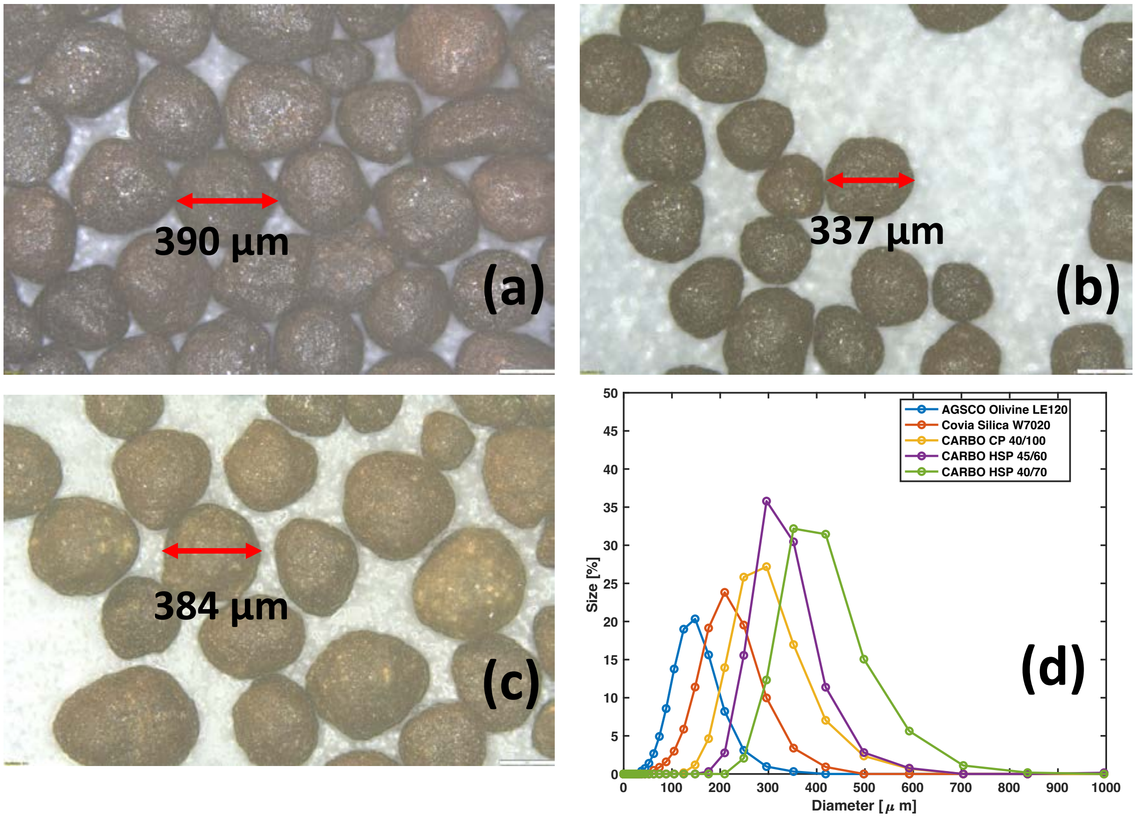

Figure 17: Photos from optical microscope showing CARBO particles tested in this program: a) HSP 40/70, b) HSP 45/60, and c) CP 40/100. d) Particle diameter distribution for the three CARBO particles and the olivine and silica tested in the single-channel heat transfer rig.

3.2. Passive material coatings for receiver tip thermal management

Reliable operation of indirect cavity particle receivers with fluidized beds will require some form of thermal management of the exposed receiver wall leading-edge. Mines spent some effort in this project focused on exploring methods to design and deposit protective oxide coatings for an indirect receiver leading-edge. The objective was framed within the context of designing a robust coating that could thermally spread normal solar heat fluxes away from the leading edge and could optically scatter a fraction of the radiation into the receiver cavity without the significant efficiency penalty associated with reflection. Mines identified spinel coatings [61, 62] as robust oxide structures that might be tailored structurally to achieve the objectives of the leading-edge barrier coating.

Initial work on optical/thermal barriers for receiver leading edges with scalable dip-coating of porous oxides. Coating application as highlighted in Fig. 18a were adopted from methods for depositing porous $BaTiO_3$ on oxidized Inco 718 and SS304. Suspensions of $BaTiO_3$ powder (mean particle diameter 1 μm) in a toluene-methanol azeotrope were dip coated on SS304 coupons and tubes, which were pre-oxidized at either 500°C or 1100°C for 1 h in air. The coatings were fired in a closed saggar buried in coarse activated carbon at 1100°C for 3 h in air. The carbon reduced the O_2 partial pressure during firing. About 100 formulations were tested for adhesion with thermal cycling. Rapid thermal cycling tests with ramps of 25°C/min to 900°C of the $BaTiO_3$ consistently showed spallation and poor adhesion for all process conditions. Coatings shifted to $CuCr_2O_4$ and $MnFe_2O_4$ spinels with processing routes like $BaTiO_3$ although sintering temperatures were higher for the spinels, 1200°C or higher.

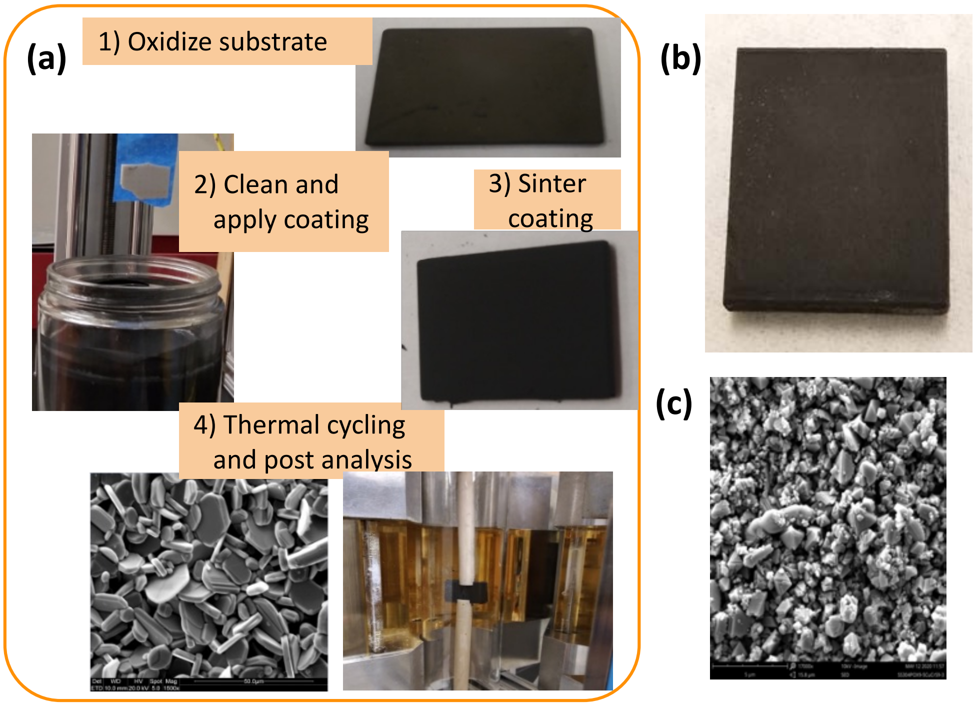

Figure 18: a) Schematic showing the steps for applying and testing protective oxide coatings on oxidized metal substrates. b) Photograph showing a SS304 plate coated with $CuCr_2O_4$, after 10 thermal cycles to 900°C. c) Scanning electron micrograph showing a SS304 plate coated with $CuCr_2O_4$, after 40 thermal cycles to 900°C at 100°C /min. No delamination or cracking was observed in the coating.

Dip coatings of $CuCr_2O_4$ and $MnFe_2O_4$ resulted in a highly adherent porous coatings prior to sintering. These spinels are thermodynamically stable at 1100°C with high absorptivity and emissivity [61]. Pre-oxidized Haynes 230 and SS304 coupons and tubes were dipped into the spinel powder slurries at a controlled speed for 10 s. Coated samples were fired in a closed saggar at 1100 °C for 1 to 3 h in air and formed highly porous surface coatings. Thermal testing of the dip coatings involved first heating to a steady 900°C and 1100°C at 10°C/min. Several $CuCr_2O_4$ coatings were tested in a furnace with ramp rates at 25°C/min and 100°C/min to 900°C, hold for 10 min, ramp to 700°C, ramp to 900°C, ramp to 100°C with repetition either 10 or 40 times. No mass loss was observed for all samples sintered at 900°C after both thermal cycling runs and no changes in the visual appearance of the coatings. Figure 18b) shows an image of one the samples after the 25°C/min heat treatment for 10 cycles. Figure 18c) shows an SEM image of one of the samples after the 100°C/min heat treatment for 40 cycles. If coatings survived those tests they were tested with rapid cyclic heating in a near-IR lamp furnace (Ulvac VHT-44) with heating rates of 100°C/min up to 1000°C for 10 to 40 cycles. Over 100 different samples were tested via thermal aging and rapid thermal cycling. The porous coatings did not prevent severe oxidation of the underlying metal above 1100°C.

Mines changed coating methods to use reactive Pechini methods that produce microporous $CuCr_2O_4$ structures that were applied to oxidized high-temperature alloys such as Haynes 230. To explore ideal coatings, $CuCr_2O_4$ coatings on pure Al_2O_3 substrates and free-standing coatings were sintered at temperatures up to 1450°C. With these ideal conditions, dense coatings formed flake-like microstructures shown in Fig. 18a, which have the potential to support anisotropic conductivity with high conductivity in plane and low conductivity normal to the bonding surface. This is desirable because it may spread solar irradiation fluxes normal to the surface of the receiver leading edge. Although the porous $CuCr_2O_4$ dip coatings survived rapid thermal cycling (10 cycles) up to 1100°C, these coatings on their own did not sufficiently protect the substrate from surface oxide scaling during high-temperature sintering. An alternative approach to produce spinel coatings via a simple chemical precursor Pechini method that lowers the sintering temperature. The Pechini method allowed for coatings on oxidized metals without significant underlying metal oxidation. However, funding constraints led to this task being terminated after Budget Period 2 before a reliable process design could be established for using the Pechini method on oxidized H230 substrates.

4. Models for fluidized bed characterization and HX design

Model development served three principal purposes in this research and development effort. Firstly, reduced-order 1-D HX and receiver models that were calibrated against experimental measurements were needed to assist in design and simulation of concepts for demonstration. This was particularly true for designing the fluidized-bed particle-sCO_2 HX that was demonstrated at NSTTF. A second purpose of the modeling effort involved the identification of pathways for improving performance that would direct further research and test plans that might achieve challenging Milestones. Finally, higher fidelity 3-D models were pursued to understand how the governing physics in the narrow-channel counterflow fluidized beds. The difficulty in using non-intrusive measurements in bubbling fluidized beds places more importance on detailed models that are calibrated against measurable performance metrics such as T_p, α_p, and $h_{T,w}$ can provide key insight into important processes related to particle wall interactions.

Initially, Mines created a reduced-order 1-D model of a single-channel fluidized bed with sCO_2 microchannels in the bounding walls to simulate a multi-channel counterflow fluidized bed, particle-sCO_2 HX. This model adopts fluidized bed momentum, mass, and thermal energy transport models that have been presented in previous models [63, 64] and applies them to the narrow-channel geometry for comparing to rig performance and for designing a multi-bed 40-kW_{th} demonstration HX. The fluidized bed model did not initially incorporate an axial dispersion model and work is ongoing to calibrate a dispersion model to continuous flow experiments in both the single-channel heat transfer rig and the demonstration 40-kW$_{th}$ particle-sCO$_2$ HX. This model served as a basis for establishing design parameters of that particle-sCO$_2$ HX, which informed the design and fabrication of the actual core in collaboration with Sandia and VPE, whose diffusion-bonded plate fabrication is well-suited for our proposed multi-bed design approach and used in the Sandia moving packed bed plate HX design [10]. The single-channel test rig experiments provided correlations to calculate $h_{T,w}$ for the 1-D modeling and furthermore, those models with the correlation have been used to identify operating conditions and particle properties that satisfy the target average $h_{T,w}$ > 1000 W m^{-2} K^{-1} for $T_{p,in}$ = 600°C and $\dot{m}_{g,in}/\dot{m}_{p,in}$< 2%. Mines used the 1-D model fluidized bed HX model for extensive studies for designing the 40-kW$_{th}$ particle-sCO$_2$ HX and assessing its performance over a broad range of operating conditions including test conditions expected at Sandia's NSTTF particle-sCO$_2$ ($T_{p,in}$ up to 630°C) and operating conditions characteristic of a full-scale TES subsystem coupled to an sCO2 power cycle (with $T_{p,in}$ approaching 750°C). These HX modeling and design studies were presented at the ASME Conference on Energy Sustainability and at SolarPACES 2021 with a corresponding SolarPACES paper accepted for publication [27]. The model results provide a comprehensive assessment of the tradeoffs in HX design and operation.

In addition to the 1-D design modeling, Mines and Sandia also developed 3-D Eulerian-Eulerian models to simulate counterflow fluidizing flows to evaluate bubble-wall dynamics in narrow-channel beds. Both Mines and Sandia build independent 3-D Eulerian-Eulerian model development in ANSYS Fluent to assist in understanding impacts of bed structure on fluidized bed heat transfer. Multi-physics modeling at Sandia coupled the fluidized bed and sCO$_2$ flow modeling to wall thermal and stress calculations to evaluate the viability of the HX design with respect to thermodynamic stability.

4.1. 1-D model development for particle-sCO$_2$ HX design

The reduced order 1-D HX model coupled a narrow-channel, counterflow fluidized bed to a plug flow model of the counterflow sCO$_2$ in microchannels with finned wall heat transfer through the solid wall matrix to provide the single repeat unit for simulating a full particle-sCO$_2$ HX to support design and performance assessment of full-scale HX. Updated Nu_{pc} correlations presented earlier were implemented into the reduced-order 1-D fluidized bed HX models to design of the particle-sCO$_2$ HX and assess its expected performance over a range of operating conditions. The reduced order model has been presented at SolarPACES [27] and will be published in multiple venues both through AIP proceedings, other journal articles, and Mines dissertations currently under preparation. The detailed governing equations for the fluidized bed can be found in those references. To date only preliminary sub-models of axial dispersion have been incorporated into the 1-D model fluidized bed governing equations. To date, these models which are derived from HX analysis and the literature overpredict the observed flattening of the vertical T_p profile. The uniqueness of the narrow-channel bed may not be well captured by the models for axial dispersion developed for much larger beds, and the Mines' team continues to work on this for further HX modeling and design.

To date, the 1-D particle-sCO$_2$ HX model has been used to explore design and operating condition trade-offs with respect to TES subsystem performance and costs. parameters were explored as function of particle-sCO$_2$ HX geometric parameters and HX operating conditions with the reduced order 1-D HX model. Baseline geometric design and operating parameters used in modeling the prototype particle-sCO$_2$ HX assumed a core height of $\Delta y_b = 0.40$ m and the number of channels to range from 10 to 13. Figure 19 plots 1-D modeling results for a HX with 13 parallel beds with $\Delta z_b = 12$ mm. The profiles in Fig. 19 do not capture axial dispersion and thus show steeper gradients and low particle outlet approach temperatures $T_{p,out} - T_{CO2,in} < 20°C$. Relatively low gas pressure drops across the fluidized bed (not including the injector) are achieved with a low inlet superficial gas velocity $U_{g,in} = 0.38$ m s^{-1}.

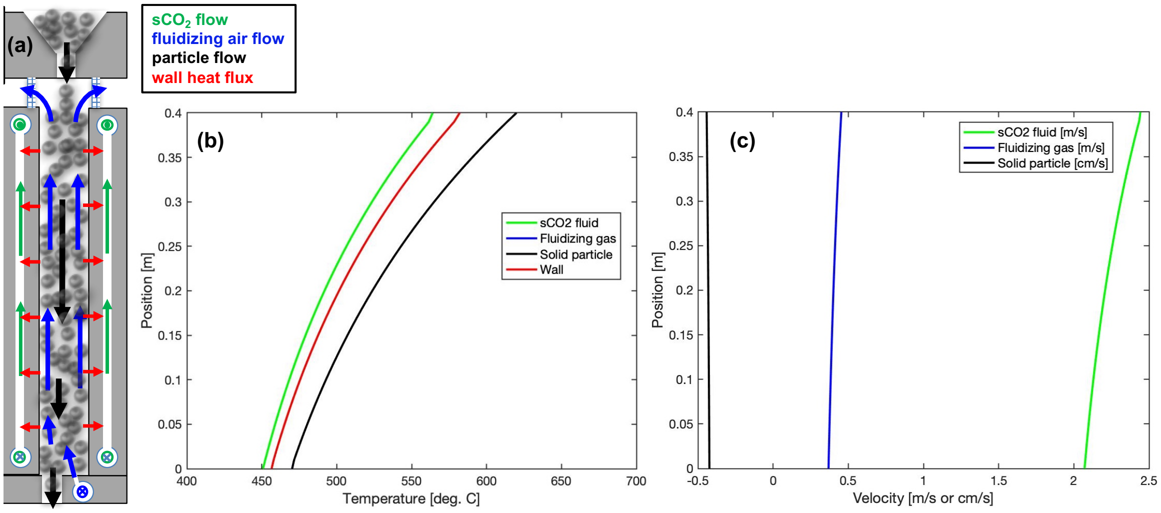

Figure 19: a) Schematic (not to scale) of narrow channel, counterflow fluidized bed with downward particle flow exchanging heat with upward sCO$_2$ flow. b) Temperature and c) velocity profiles from the reduced-order 1-D model results at $T_{p,in} = 620°C$. $T_{CO2,in} = 400°C$, and $\dot{m}_g/\dot{m}_p = 0.015$ with $d_p = 260$ µm. Mean overall $U = 605$ W m^{-2} K^{-1}.

The performance of different HX designs were compared based upon average $h_{T,w}$, the overall particle-sCO$_2$ U, the particle outlet approach temperature $T_{p,out} - T_{CO2,in}$, total heat transfer rate $\dot{Q}_{HX}$, heat exchanger effectiveness ϵ_{HX}, and a heat recovery efficiency (η_{HX}) as performance metrics. overall U is calculated as the surface-average coefficient eq. 9.

$$U = \frac{1}{\frac{1}{h_{T,w}} + \frac{\Delta z_w}{\lambda_w} + \frac{1}{\eta_{0,fin} h_{T,sCO2} (A_{fin}/A_{base})}} \qquad \text{(eq. 9)}$$

The overall particle-sCO$_2$ U accounts for thermal resistances due to particle-wall heat transfer, conduction through the intermediary wall, and finned wall convection to sCO$_2$ flowing through embedded micro-channels with fin effects from the walls that separate the micro-channels. The heat transfer coefficient between the microchannel walls and sCO$_2$ flow $h_{T,sCO2}$ is generally very high for the 0.75 mm deep and wide channels used in the demonstration HX design. Using sCO$_2$ thermodynamic properties from Span and Wagner [65] and transport properties from Vesovic et al. [66], the model predicted $h_{T,sCO2}$

of 2000 W m^{-2} K^{-1} and higher. Considering the three thermal resistances in the denominator in eq. 9, the largest resistance by far is $1/h_{T,w}$ associated with the particle-wall heat transfer, which is why increasing $h_{T,w}$ is critical to reducing HX size and costs.

The total heat transfer ($\dot{Q}_{\mathrm{HX}}$) is found by calculating the enthalpy rise of the sCO_2 over the length of the HX core. HX effectiveness ϵ_{HX} is the ratio of the total amount of heat transfer to the sCO_2 to the maximum possible heat transfer, where the maximum possible heat transfer is the minimum enthalpy change of the particles or sCO_2 over the maximum possible temperature change ($T_{\mathrm{p,in}} - T_{\mathrm{CO2,in}}$). For design cases considered, the particle flow represented the minimum enthalpy flow and therefore was used to define the maximum possible heat transfer. Finally, optimizing the design of the particle-sCO_2 HX requires a cost function for the overall TES subsystem (in \$/kWh_{th}) and/or HX (in \$/kW_{th}). An initial optimization methodology in this study employed heat recovery efficiency η_{HX}, which is the ratio of net electric work potential of heat captured in the sCO_2 $\dot{W}_{\mathrm{elec,avail}}$ to thermal energy available from the particle flow $\dot{Q}_{\mathrm{p,max}}$.

$$\eta_{\mathrm{HX}} = \frac{\dot{W}_{\mathrm{elec,avail}}}{\dot{Q}_{\mathrm{p,max}}} \qquad \text{(eq. 10)}$$

$\dot{W}_{\mathrm{elec,avail}}$ is the power generated from the sCO_2 power cycle based on its efficiency minus the parasitic energy needed to pump the sCO_2 and fluidizing gas through the HX.

$$\begin{aligned}\dot{W}_{\mathrm{elec,avail}} = \eta_{\mathrm{cyc,elec}}\left(T_{\mathrm{sCO2,out}}\right)\dot{Q}_{\mathrm{HX}} - \frac{N_{\mathrm{bed}}\dot{m}'_{\mathrm{f}}}{\eta_{\mathrm{elec,f}}\eta_{\mathrm{s,f}}}\int_{P_{\mathrm{f,out}}}^{P_{\mathrm{f,in}}} v_{\mathrm{f}}\, dP_{\mathrm{f}} \\ - \frac{N_{\mathrm{bed}}\dot{m}'_{\mathrm{g}}}{\eta_{\mathrm{elec,g}}\eta_{\mathrm{s,g}}}\int_{P_{\mathrm{g,out}}}^{P_{\mathrm{g,in}}} v_{\mathrm{g}}\, dP_{\mathrm{g}}\end{aligned} \qquad \text{(eq.11)}$$

The electrical efficiency of the power cycle ($\eta_{\mathrm{cyc,elec}}$) and the electrical (η_{elec}) and isentropic (η_{s}) efficiencies of the sCO_2 and fluidizing gas pumps are taken from previous references [47]. Similarly, the electric and isentropic efficiencies of the fluidizing gas pump are taken as $\eta_{\mathrm{elec,g}}$ = 0.70 and $\eta_{\mathrm{s,g}}$ =0.75 [2]. From a previous reference, $\eta_{\mathrm{cyc,elec}}\left(T_{\mathrm{f,out}}\right) = 0.3433\ln\left(T_{\mathrm{sCO2,out}}\right) - 1.8441)$ [67].

The impact of fluidized bed channel depth, Δz_b (from 8 to 21 mm) and gas-particle mass flow ratio $\dot{m}'_{\mathrm{g,in}}/\dot{m}'_{\mathrm{p,in}}$ (from 0.5% to 2.5%) on performance of the multi-bed particle-sCO_2 HX are shown in Fig. 20 using the correlations from Fig. 9. The results illustrate a region in Δz_b and $\dot{m}'_{\mathrm{g,in}}/\dot{m}'_{\mathrm{p,in}}$ that maximizes heat transfer and corresponds to a $\hat{U} \approx 50$. For a given $\dot{m}'_{\mathrm{g,in}}$, $\hat{U}$ increases with decreasing Δz_b. The highest heat transfer and optimal ϵ_{HX} and η_{HX} are found at the smallest Δz_b = 8.0 mm with $\dot{m}'_{\mathrm{g,in}}/\dot{m}'_{\mathrm{p,in}}$= 1.25%. The optimal overall $U \approx 600$ W m^{-2} K^{-1} was achieved with less $\dot{m}'_{\mathrm{g,in}}$ but the same narrower Δz_b.

No conditions in Fig. 20 reached the target surface-averaged $h_{T,w} > 1000$ W m^{-2} K^{-1}. Thus, with the initial $h_{T,w}$ correlations presented in Fig. 9, HX modeling explored how smaller d_p for down to 160 μm and $T_{p,in}$ up to 740°C can enable such high $h_{T,w}$. Results illustrate improvements in metrics with increased $T_{p,in}$ and lower d_p. Dropping d_p has a larger influence on $h_{T,w}$ and ϵ_{HX}, while raising $T_{p,in}$ more strongly impacts overall U.

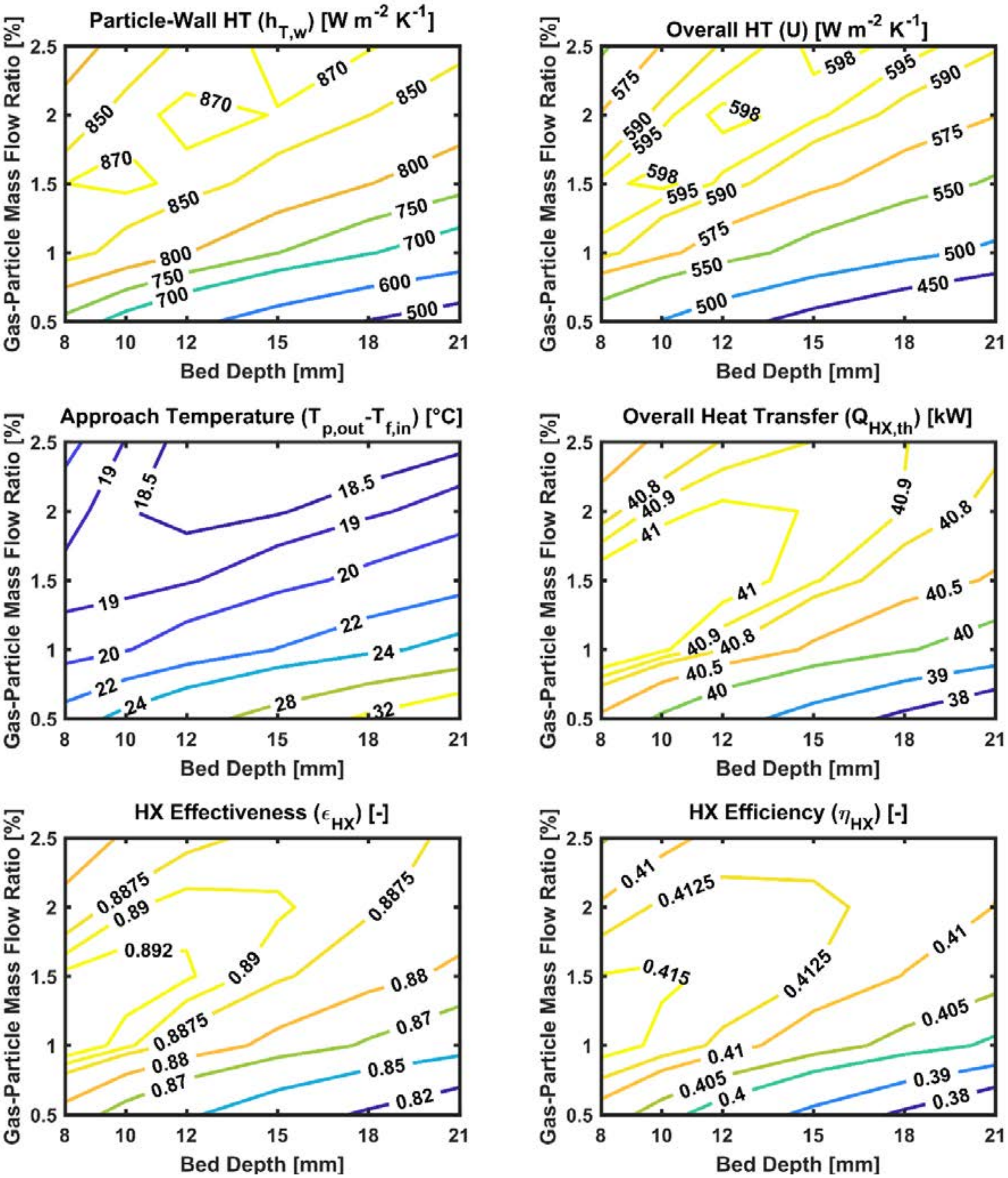

Figure 20: Contour plots of HX performance metrics for a range of Δz_b and $\dot{m}'_{g,in}/\dot{m}'_{p,in}$ relevant for operation of the 40-kW$_{th}$ particle-sCO$_2$ HX to be designed with $T_{p,in}$ = 620°C and d_p = 260 μm. No conditions reach $h_{T,w} \geq 1000$ W m^{-2} K^{-1} target.

With the $h_{T,w}$ correlations, Mines used the 1-D reduced order models to design the nominal 40-kW$_{th}$, particle-sCO$_2$ HX based on parallel narrow-channel, fluidized beds and diffusion bonded plates with embedded sCO$_2$-flow microchannels similar in design to Sandia's moving packed bed HX walls [11]. Design operating conditions were selected based on using low-cost stainless steel for this first prototype and thus, $T_{p,in}$ was limited to 600°C. The 1-D fluidized bed HX models predict profiles of gas temperature T_g, T_p,

T_w, T_{sCO2}, pressures p_g, p_{sCO2}, and solids volume fraction, α_p, and the phase velocities for gas and solids in the bed, and sCO$_2$ in the microchannels. These model results met a go/no-go milestone of a simulated design that predicts $T_{p.out} - T_{sCO2,in} < 30°C$ and average $h_{T,w} \geq 1000$ W m^{-2} K^{-1} for a 40-kW$_{th}$ primary HX operating at $\dot{m}_{g,in}/\dot{m}_{p,in} < 2\%$.

The particle-sCO$_2$ HX model assessed bed designs and operating conditions for the prototype 40-kW$_{th}$ HX with HSP 40/70 particles at flowrates close to 20 g s^{-1} per channel bed to achieve the targeted $\Delta T_p > 150°C$ and > 40-kW$_{th}$ heat transfer for $\Delta y_b = 0.4$ m and width $\Delta x_b = 0.2$ m. Table 3 presents 4 columns of conditions for parametric studies of the 12-bed prototype particle-sCO$_2$ HX at fixed height, width and inlet T and P for the particle, air, and sCO$_2$. With 12 bed channels, the bed-wall surface area in the HX core $A_{w,tot}$ = 1.92 m^2 and average core heat flux > 20.8 W m^{-2} achieves 40 kW$_{th}$ heat transfer. Columns 1 and 3 present parametric studies for the contour plots of Figs. 21 and 22.

Table 3: Single bed operating conditions and geometric parameters for various parametric studies to identify design and operating conditions for 40-kW$_{th}$ prototype HX.

Model Input Parameter	**HSP 40/70, high $\dot{m}_p$**	**HSP 40/70, low $\dot{m}_p$**	**HSP 40/70, high $\dot{m}_g$**	**CP 40/100 high $\dot{m}_g$**
particle flow rate $\dot{m}_{p,in}$	21.9 g s^{-1}	18.7 g s^{-1}	[10 – 40] g s^{-1}	[10 – 40] g s^{-1}
particle inlet temp. $T_{p,in}$	620°C	620°C	620°C	620°C
HSP 40/70 mean diam. d_p	322 μm	322 μm	322 μm	260 μm
fluidizing air flow rate $\dot{m}_{g,in}$	[0.025 – 0.700] g s^{-1}	[0.025 – 0.700] g s^{-1}	0.40 g s^{-1}	0.35 g s^{-1}
fluidizing air inlet temp. $T_{g,in}$	450°C	450°C	450°C	450°C
sCO$_2$ flow rate, $\dot{m}_{sCO2,in}$	26.2 g s^{-1}	22.4 g s^{-1}	[10 – 40] g s^{-1}	[10 – 40] g s^{-1}
sCO$_2$ inlet pressure, $P_{sCO2,in}$	17 MPa	17 MPa	17 MPa	17 MPa
sCO$_2$ inlet temp, $T_{sCO2,in}$	450°C	450°C	450°C	450°C
bed height, Δy_{bed}	0.4 m	0.4 m	0.4 m	0.4 m
bed width, Δx_{bed}	0.2 m	0.2 m	0.2 m	0.2 m
bed depth, Δz_{bed}	[5 – 20] mm	[8 – 20] mm	12 mm	12 mm
number of sCO$_2$ micro-channels per wall n_{chan}	160	160	160	160
hydraulic diam. of sCO$_2$ micro-channels, $d_{h,chan}$	0.75 mm	0.75 mm	0.75 mm	0.75 mm

Figure 21 shows contour plots detailing how variations in $\dot{m}_{g,in}$ and Δz_b impact the particle-sCO$_2$ HX performance. For the relatively high $\dot{m}_{p,in}$ and $\dot{m}_{sCO2,in}$ in Figure 2.5, adequate mean heat flux > 20.8 kW m^{-2} target to achieve 40 kW$_{th}$ with 12 bed channels occurs over a wide range of gas flow rates $\dot{m}_{g,in}$ and Δz_b. Necessary gas flow rates increase with bed depth to sustain U_g for high $h_{T,w}$. However, large d_p of HSP 40/70 does not provide $h_{T,w}$ > 800 W m^{-2} K^{-1} at these conditions and limits predicted overall U < 600 W m^{-2} K^{-1}. Raising $h_{T,w}$ > 1000 W m^{-2} K^{-1} requires a d_p below 260 μm and higher operating T_p. Smaller Δz_b enables lower $\dot{m}_{g,in}$ to achieve comparable overall U and total heat flux, but it remains to be seen if the thinner beds can maintain uniform fluidization over the narrow channel.

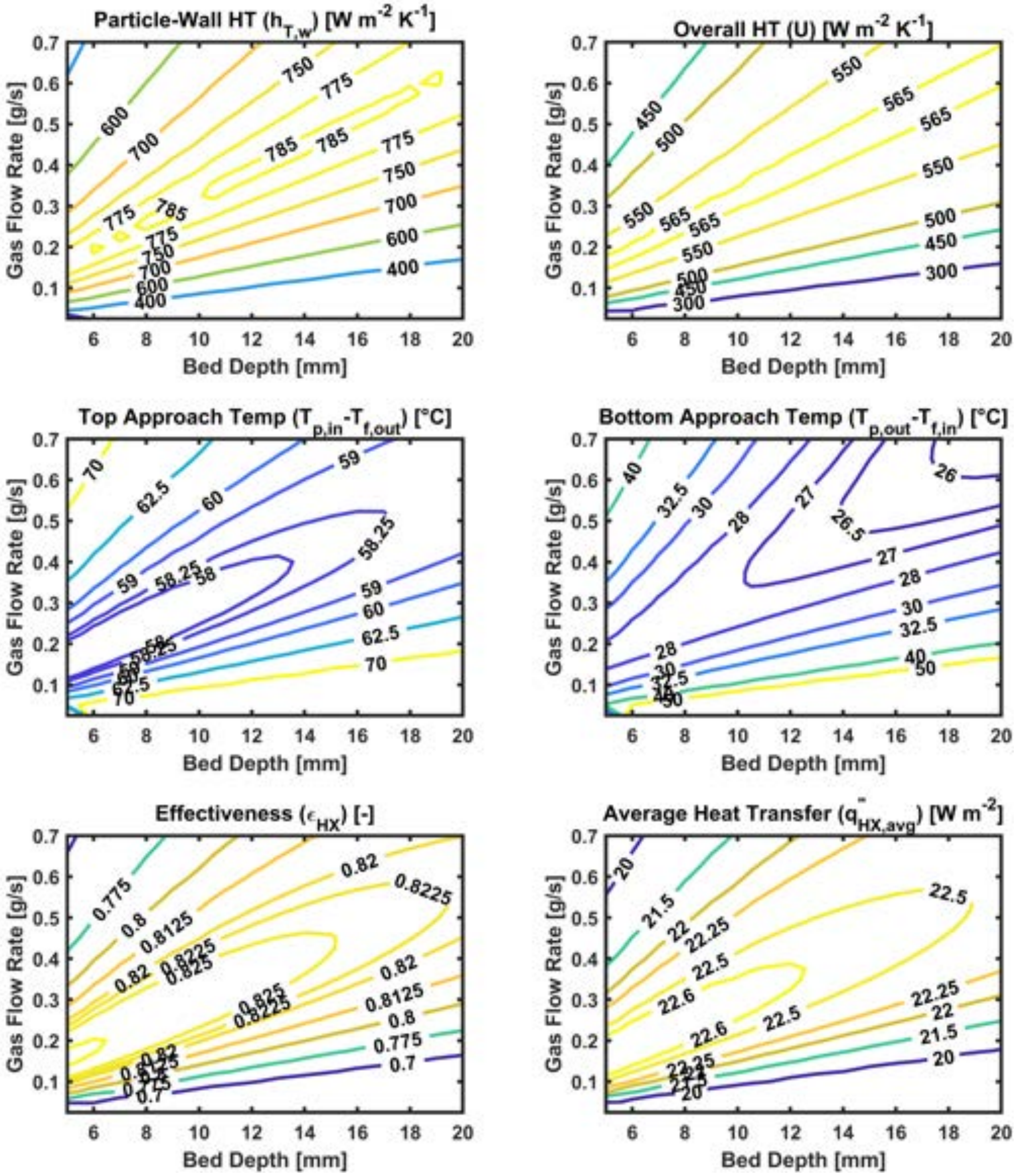

Figure 21: Contour plots vary fluidizing air mass flow rate per channel $\dot{m}_{g,in}$ and bed depth Δz_b. The six plots show $h_{T,w}$, sCO$_2$ outlet approach temperature ($T_{p,in} - T_{sCO2,out}$), HX effectiveness ε_{HX}, overall heat transfer coefficient U, particle outlet approach temperature ($T_{p,out} - T_{sCO2,in}$), and average wall heat flux. Single-bed simulation conditions and bed geometry are highlighted in Table 3 and include a fixed particle flow rate of 21.9 g s^{-1} of HSP 40/70 per bed.

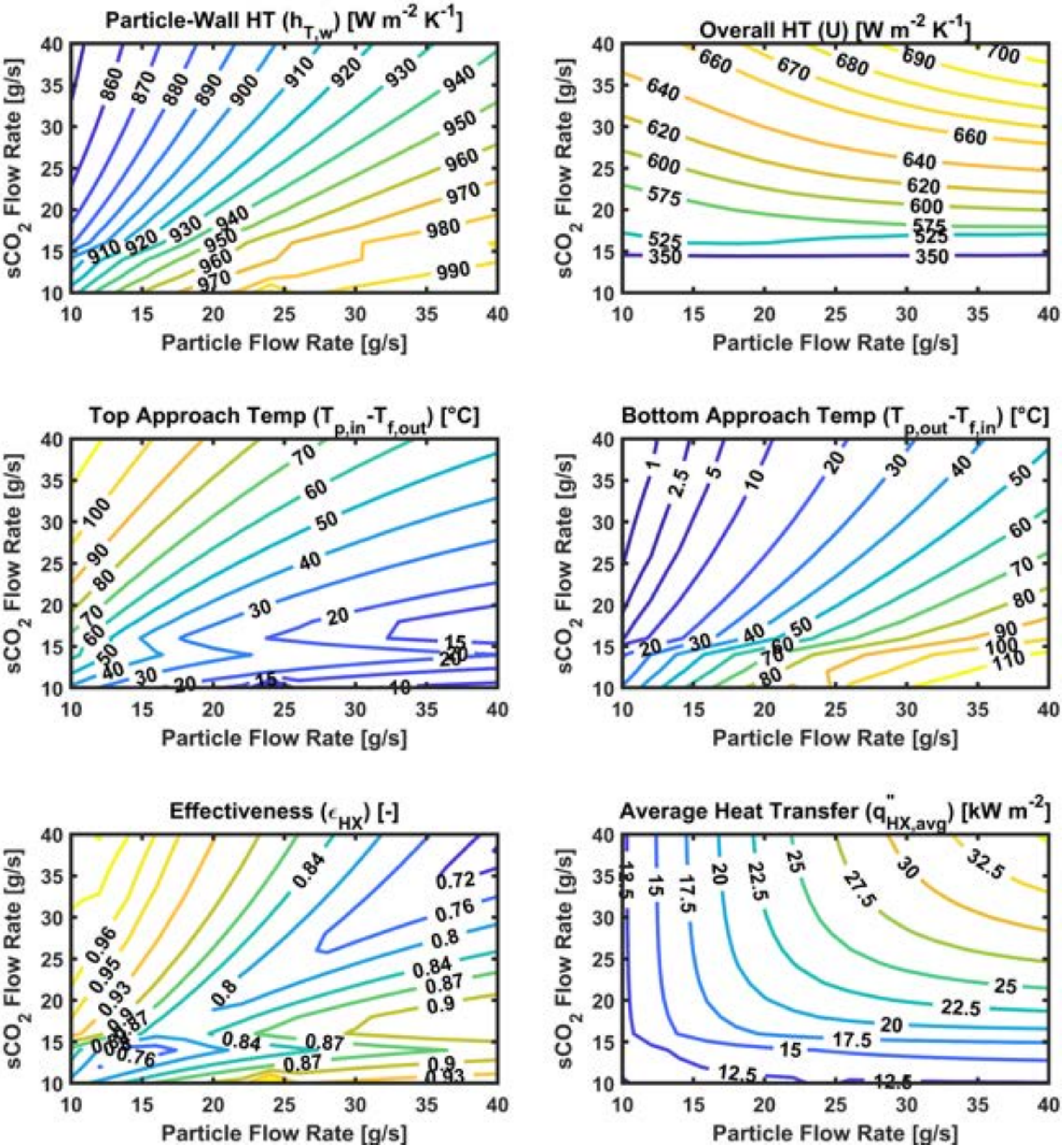

Figure 22: Contour plots vary fluidizing air mass flow rate per channel $\dot{m}_{sCO2,in}$ and particle mass flow rate per channel $\dot{m}_{p,in}$ with reduced diameter (d_p = 260 μm) HSP 40/70. The six plots show particle wall heat transfer coefficient $h_{T,w}$, sCO$_2$ outlet approach temperature ($T_{p,in}$ – $T_{sCO2,out}$), HX effectiveness ε_{HX}, overall heat transfer coefficient U, particle outlet approach temperature ($T_{p,out}$ – $T_{sCO2,in}$), and average wall heat flux. Single-bed simulation conditions and bed geometry are highlighted in Table 3 and include a fixed air flow rate of 0.35 g s^{-1} per channel bed.

The smaller d_p of HSP 45/60 and CP 40/100 gives a pathway to achieving surface $h_{T,w}$ > 1000 W m^{-2} K^{-1} at actual primary HX if the correlations from the single-channel experiments translate to higher T_p. To assess this, the 1-D HX model was ran over a range of $\dot{m}_{g,in}$ at the fixed $\dot{m}_{p,in}$ = 21.9 g s^{-1} and $\dot{m}_{sCO2,in}$ = 26.2 g s^{-1} per channel for Δz_b = 12 mm and $T_{p,in}$ = 600°C and 750°C. Figure 23 indicates a maximum predicted U > 600 W m^{-2} K^{-1}., and wall heat flux with $\dot{m}_{g,in}/\dot{m}_{p,in} \approx$ 1% for d_p = 260 μm.

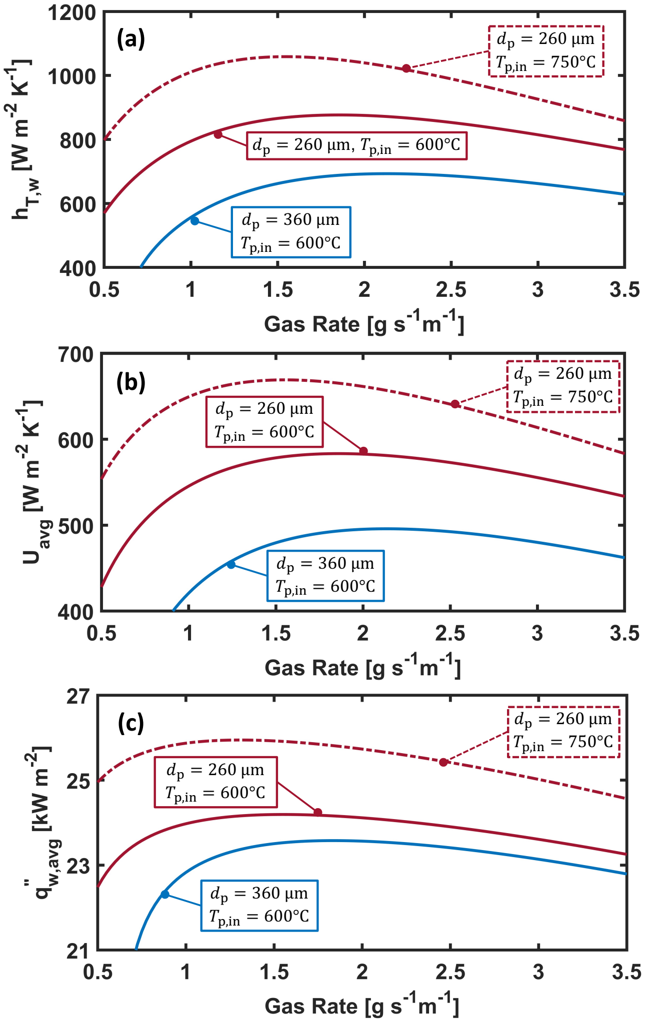

Figure 23: Plots of HX performance vs. fluidizing gas flow per m of bed width in terms of a) $h_{T,w}$, b) overall U, and c) average wall heat flux as predicted by the reduced-order 1-D HX model. Results are for HSP 40/70 at a fixed $\dot{m}_{p,in}$ and $\dot{m}_{sCO2,in}$ specified in the first column of Table 3. Performance improves with reduced d_p = 260 μm and with increasing $T_{p,in}$ to 750°C characteristic of an sCO$_2$ power cycle.

4.2. 1-D model development for indirect particle receiver design

The quasi-1-D numerical model of the fluidized bed was adopted for indirect receiver including convection and radiation on the external and internal wall surfaces, and conduction along the wall. The radiation modeling of the external wall assumed cavity surfaces angled to an aperture solar flux such that directly irradiated cavity surfaces receive normal fluxes around 200 kW m^{-2}. The baseline case here involves a fluidized bed depth of 12 mm, width of 0.1 m, and height of 0.25 m., which simulates rig conditions for the single-channel heat transfer rig. Figure 24 shows temperature and α_p profiles for HSP 40/70 and HSP 45/80 at nominal d_p. The results predict external wall $T_{w,ext} < T_p + 100°C$ all the way up to $T_{p,out} = 800°C$ for a fluidized bed gas pressure drop $\Delta P_g < 10$ kPa.

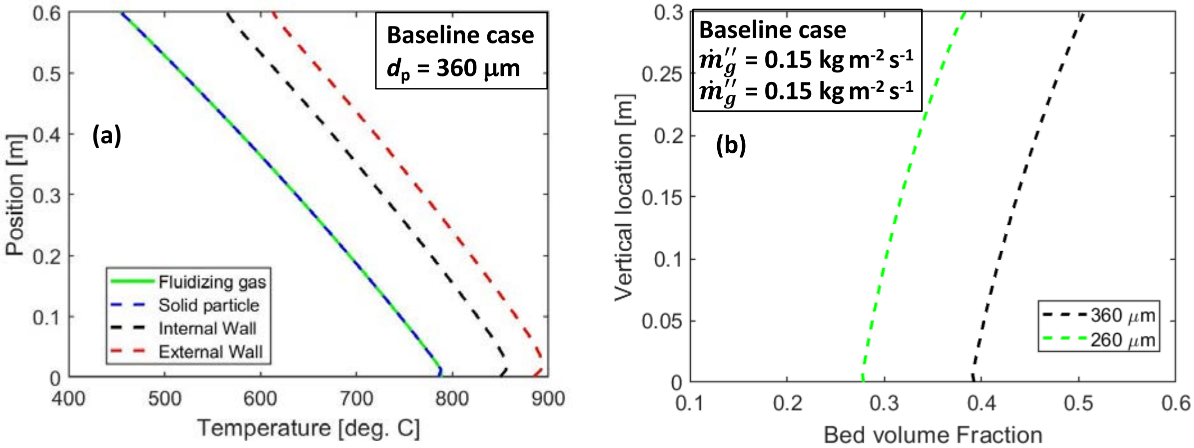

Figure 24: 1-D model indirect receiver model a) gas, solid, and wall temperature profiles for CARBOBEADHSP 40/70 and , and b) solid volume fraction α_p profiles for two different d_p. Model conditions are $T_{p,in} = 400°C$ and $q_w \approx 200$ kW/m^2.

A parametric study for both the larger and smaller d_p with respect to gas and particle mass fluxes provided a basis for understanding how the average particle-wall $h_{T,w}$ and the solar efficiency η_{solar} vary over a range of operating conditions. Figure 25 shows contour plots for both $h_{T,w}$ and η_{solar} showing that relatively low gas fluxes $\dot{m}''_g \approx 0.1$ kg m^{-2} s^{-1} can achieve optimal $h_{T,w}$ for a given $\dot{m}''_p > 80\dot{m}''_g$. These conditions can achieve η_{solar} while maintaining $T_{w,ext} < 1000°C$ on the angled surface. This does not consider the risks of extremely high $T_{w,ext}$ on leading edges, which Mines is addressing in 2-D multi- models as presented in a poster at SolarPACES 2022.

The modeling results presented in Figs. 20-24 do not incorporate axial dispersion which was observed int the continuous flow experiments. Dispersion, which can be modeled by a vertical dispersion coefficient D_{sv} for the solid phase, will certainly lower the HX performance from the model predicted values not by lowering $h_{T,w}$ but by dropping the magnitude of the temperature difference between the particles and the wall ($T_p - T_{w,int}$). This is particularly problematic for the counterflow particle-sCO$_2$ HX where the lower HX will reduce the effective log-mean-temperature difference as soon as the particles enter the HX bed channels. This will lower the overall $\dot{Q}_{HX}$ and the effective U based on $T_{p,in}$, On the other hand, for the indirect particle receiver, the flattening of the temperature profile by axial dispersion may provide some benefit by reducing thermal gradients in the hot external walls. Furthermore, because the particle receivers are not explicitly counterflow HX, the negative impact on $\dot{Q}_{rec}$ is not as severe as $\dot{Q}_{HX}$. Mines is actively integrating models for D_{sv} into the governing equations of the solid mass, heat, and

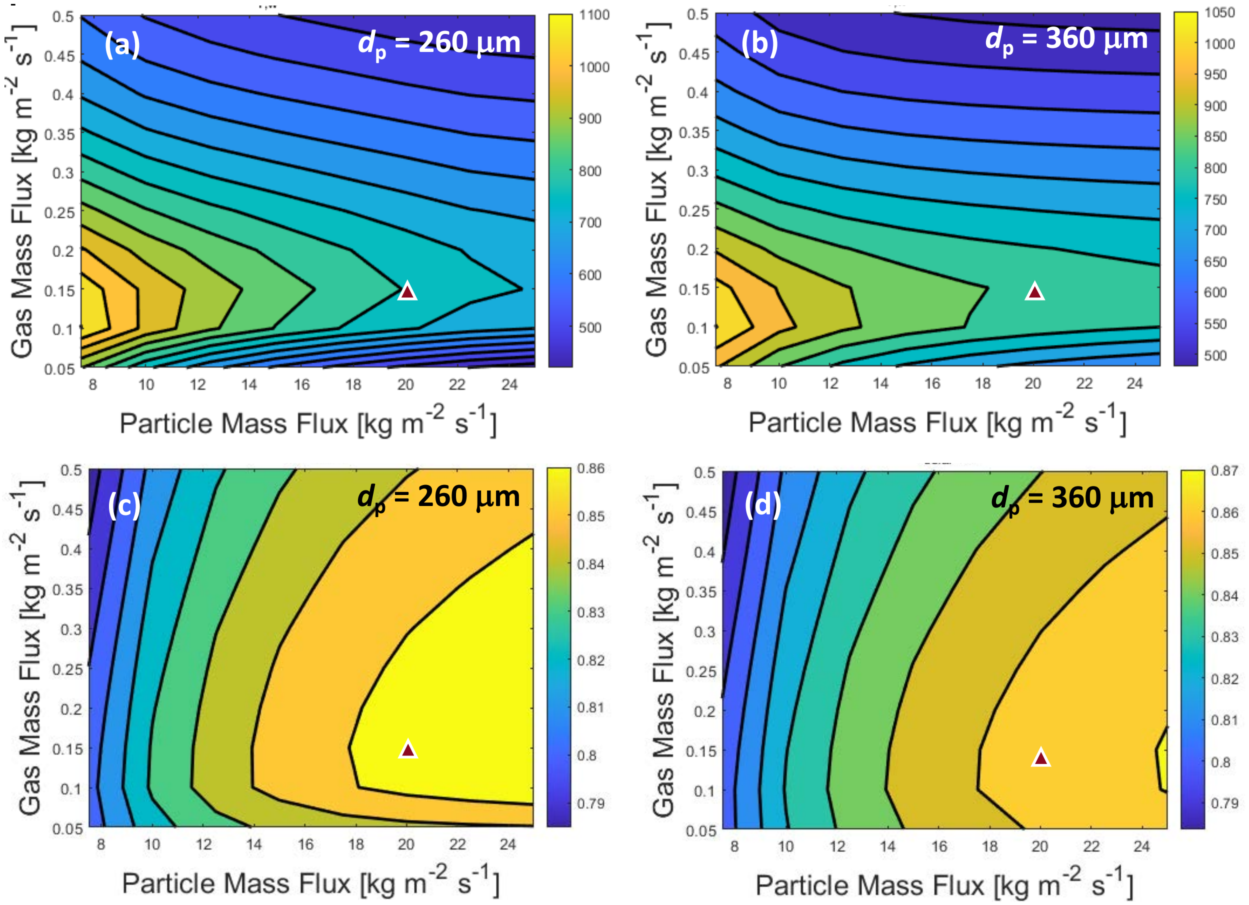

Figure 25: Contour plots of 1-D model predicted a) average $h_{T,w}$ for mean d_p = 260 μm, b) average $h_{T,w}$ for mean d_p = 360 μm, c) η_{solar} for mean d_p = 260 μm gas, and d) η_{solar} for mean d_p = 360 μm. Model conditions are $T_{p,in}$ = 400°C and $q_w \approx 200$ kW/m^2.

momentum conservation to improve the 1-D models for both the indirect receiver and particle-sCO$_2$ HX. Existing literature models as reviewed well in the early 2000s [68] do not as of yet capture the behavior observed in the unique counterflow narrow-channel beds studied here. Further exploration of models where D_{sv} is a $f(\hat{U})$ are being tested against single-channel tests still ongoing at Mines.in conjunction with other SETO-funded programs.

4.3. 3-D modeling for particle-sCO$_2$ HX analysis

Initial 3-D CFD models coupled to thermomechanical stress models were developed to explore the stresses in a particle-sCO$_2$ HX plate for the fluidized bed HX. To this end, Sandia developed 3-D models of the HX walls and coupled them to the 1-D reduced-order models of the fluidized bed and the sCO$_2$ microchannel flows to characterize T_w distributions in the HX plates. These enabled calculations of the thermomechanical stresses imposed on the 40-kW$_{th}$ particle-sCO$_2$ HX structure under expected test conditions. Both nominal Von-Mises stress distributions and fatigue life due to repeated cycling of the HX are of interest. Thermomechanical stresses are primarily generated by

1) the fluid pressure differential across the HX walls between the sCO_2 (up to 20 MPa) and the fluidized bed (near 0.1 MPa) and 2) uneven thermal expansion of the metal plates and bounding surfaces. A time-averaged thermal solution of the metal under nominal operation is required to calculate thermal stress components. The thermal solutions were generated using the heat transfer solver ARIA within Sandia's SIERRA computational Multiphysics suite. After generating a mesh for a single symmetric half-bank of the HX, thermal boundary conditions were coupled to a 1-D advective model for the microchannel sCO_2 flows using the Gnielinski Nusselt number correlation for the sCO_2 heat transfer coefficient. Simulations as shown in Fig. 26 were run for $T_{sCO2,in}$ = 400°C and $T_{p,in}$ = 600°C to approximate expected demonstration HX test conditions.

Time-averaged $h_{T,w}$ from the particles to the wall were calculated as a function of bed height in the reduced-order 1-D fluidized bed model with the Nu_{pc} correlations in Fig. 9 and the resulting steady T_w field is shown in Fig. 26. The mechanical simulation has been set up and run, and there were no indications of concerns about stress failures from steady state thermomechanical stresses. However, some refinements to the solution process are necessary to generate the Von-Mises stress distribution. These models did not resolve risks of creep failure or cyclic fatigues which might be a consideration for a future study.

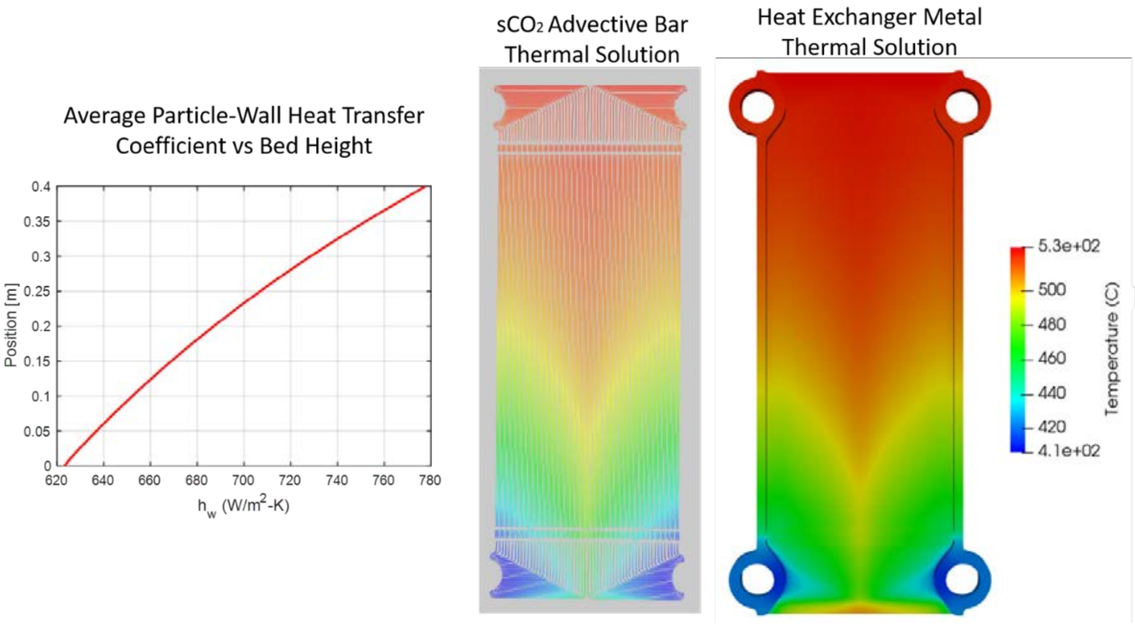

Figure 26: Steady-state temperature distributions for the demonstration HX at nominal operating conditions for estimating thermomechanical stress in the diffusion-bonded sCO_2 microchannel plates at demonstration HX operating conditions.

Mines pursued 3-D fluidized bed heat transfer simulations using Eulerian-Eulerian models in ANSYS Fluent to simulate heat transfer in narrow-channel fluidized beds operating in batch mode to match experimental tests over a range of U_g (i.e., $\hat{U}$). Wall heat transfer is simulated by applying a heat flux q_w on one side of the bed and calculating the average heat transfer across the bed at the particle-wall interfaces for a set average bed temperature T_b. To facilitate finer mesh resolution, simulations have been done on slight smaller beds 10 cm tall × 5 cm wide with an additional 20 cm of low-resolution grid above the fluidized bed region. The simulated bed depth is 10 mm and in the bed region cells of 1 mm cube are used to provide adequate resolution across the width of the bed to predict heat transfer. These simulations have been used to fit various closure terms in the two-fluid conservation equations to calibrate the models to batch mode experimental measurements with CP 40/100. Figure 27 compares measured $h_{T,w}$ vs. time-averaged model-simulated $h_{T,w}$ values over 5+ s for different average T_p with wall fluxes q_w = 25 kW m^{-2}. The model results in Fig. 27 use a particle-bed thermal conductivity from Syamlal and Gidaspow [69] through a user-defined function (UDF) in ANSYS Fluent. These simulations utilized a k-ε turbulence model and a fitted particle-wall restitution coefficient. Results show that the model does an extremely good job of predicting the shape and peak of $h_{T,w}$ vs. $\hat{U}$ and efforts are not ongoing to use the 3-D models to simulate continuous flow heat transfer in HX operation.

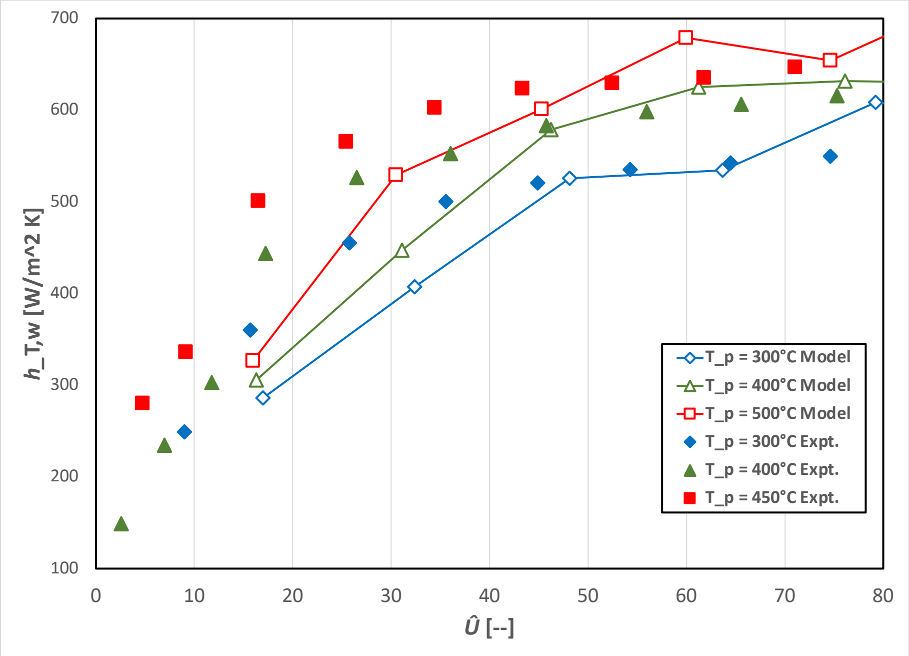

Figure 27: Comparison of experimental $h_{T,w}$ measurements for CP 40/100 in batch mode from single-channel fluidized bed heat transfer with simulated $h_{T,w}$ from a 3-D Eulerian-Eulerian model in ANSYS Fluent with adjusted model parameters with respect to particle-wall interactions to improve calibration with measured values.

Figure 28 shows snapshots over a range of time of solid volume fractions for two simulations of batch-mode fluidization for CP 40/100 at two different $\hat{U}$ = 30 and 45. These simulations are performed with average wall heat flux at 25 kW m^{-2} on the hot side and –25 kW m^{-2} on the cold wall for a fixed bed mean T_p = 400°C. Simulations show bed height growth with increased $\hat{U}$ due to a drop in mean α_p. In addition, the models show how the higher $\hat{U}$ leads to significantly higher frequency of bubble generation. The side view for $\hat{U}$ = 45 simulations show the concentration of bubbles/voids near the walls that may impact heat transfer. These 3-D models are being used to explore freeboard and injector design for future fluidized bed HX design efforts.

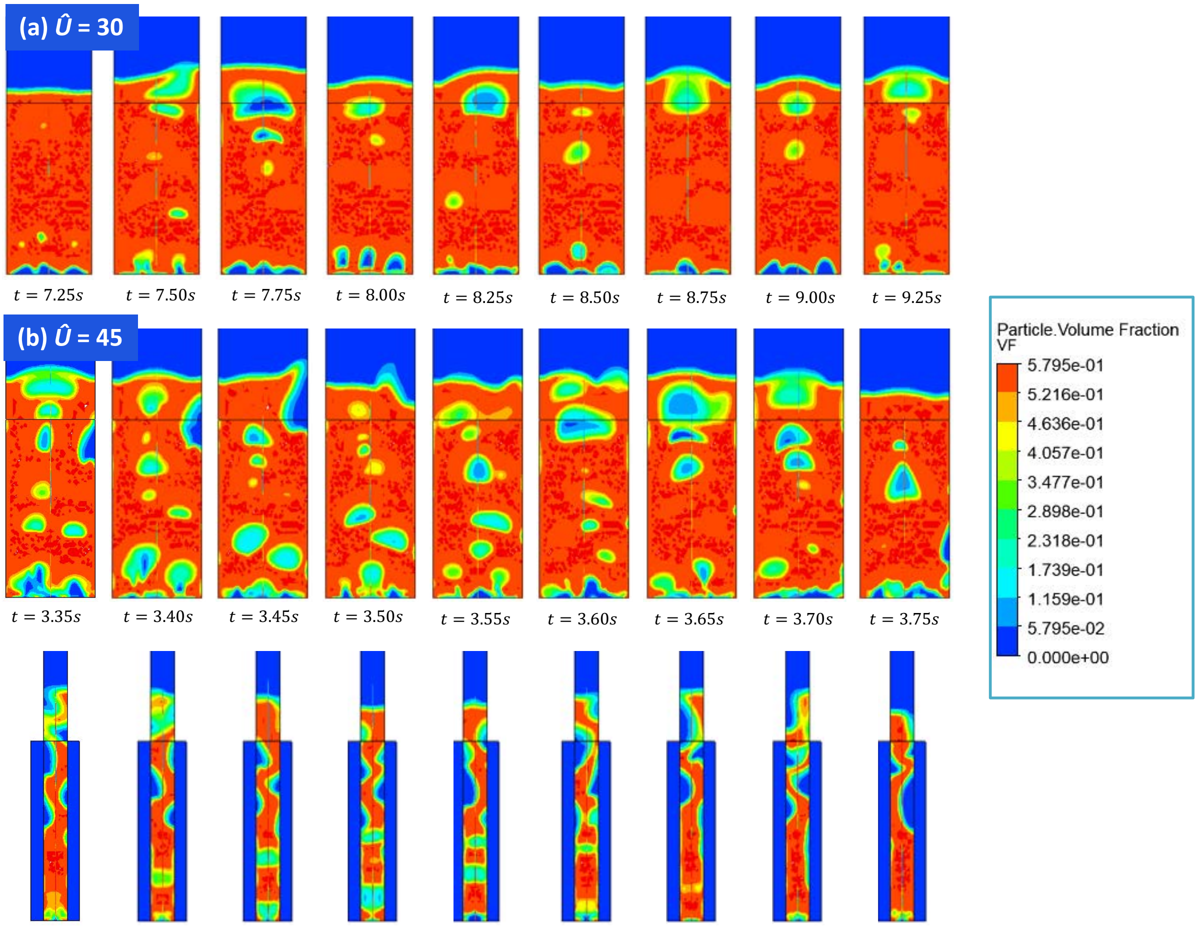

Figure 28: Instantaneous snapshots of simulated center-plane solid volume fractions α_b for a 10 cm high × 5 cm wide × 1 cm deep fluidized bed operating in batch mode at an average T_p = 400°C for two excess fluidization velocities a) $\hat{U}$ = 30 and b) $\hat{U}$ = 45. Simulations are completed as one continuous run in ANSYS Fluent with 1 mm cube cell sizes in the fluidized bed region.

5. Demonstrating prototype 40-kW$_{th}$ multi-channel particle-sCO$_2$ HX

The modeling results presented for Task 2.1 provided the basis for designing a fluidized bed particle-sCO$_2$ HX core for fabrication and eventual testing at NSTTF. Mines with Sandia's advice agreed to have VPE fabricate a multi-channel, shell-and-plate HX with VPE's proprietary microchannel etching and diffusion-bonding processes. VPE has done similar work for Sandia’s moving packed-bed HX core [70]. Design and fabrication of a 40-kW$_{th}$ fluidized bed particle-sCO$_2$ HX core in partnership with VPE was complemented by significant preparation work for testing at Sandia including 1) upgrading the sCO$_2$ and particle flow loops at Sandia, 2) installing new gas feeds and extensive instrumentation for measuring temperatures and pressures throughout the test rig, and 3) designing and fabricating inlet and outlet flow hoppers and control actuators for the HX tests at Mines. Sandia's upgrades enabled higher $\dot{m}''_{\mathrm{sCO2}}$ and $\dot{m}''_{\mathrm{p}}$ and better $T_{p,in}$ and $T_{sCO2,in}$ control.

During fabrication of an initial 40-kW$_{th}$ particle-sCO$_2$ HX core, a crack formed during the welding of the sCO_2 manifold connecting the HX core sCO_2 microchannels to the sCO_2 outlet flow pipe, and thus this first HX was only used to assess particle flow and fluidization at room temperature at Mines. VPE agreed to build a second HX core with a revised design that integrated the sCO_2 manifold into the diffusion-bonded plates. Supporting components included a wedge feed hopper, a unique particle feed control mechanism, a freeboard zone above the core with particle-gas separation, a downstream exit hopper, and the air manifold for the fluidizing gas. VPE finished fabrication of the second HX core near the end of Budget Period 2. Pushing the demonstration fluidized bed HX tests to Budget Period 3 allowed for upgrades to Sandia's NSTTF particle-sCO_2 HX test facility. The tests as summarized below achieved some performance Milestones, but failed to significantly outperform moving packed bed HX with narrower bed channels [10], because the drop in LMTD offset the higher $h_{T,w}$ values with fluidization. All the same the tests did provide some unique insight on how to operate a multi-channel fluidized bed HX with stable flows through all the parallel channels, and there are pathways to improving performance by suppressing dispersion and increasing $h_{T,w}$ with extended surfaces as now being pursued in a follow-on program with Brayton Energy and Mines.

5.1. Fabrication and assembly of 40-kW$_{th}$ particle-sCO$_2$ HX and test facility

The modeling study with the reduced order 1-D model of the particle-sCO_2 HX core as highlighted in Figs. 20-22 led to choosing 12 parallel fluidized beds with a core heat transfer region height Δy_b = 0.4 m and width Δx_b = 0.2 m, and bed channel depth Δz_b = 0.012 m. The HX core integrated inlet and outlet manifolds for the sCO_2 flows and locations for injector tubes for the fluidized gas into each channel. The 12 narrow-channel fluidized beds are bounded on the sides by spacer strips. which are diffusion bonded to walls composed of two 16-gauge SS304 solid sheets and 2 16-gauge sheets with etched-microchannels in a zig-zagged configuration for upward sCO_2 flows with effective $h_{T,sCO2}$ on the order of 2000 W m^{-2} K^{-1} (based on VPE models). This provides 2 sCO_2 microchannel plates per fluidized bed channel. The outer walls of the core are composed of additional 16-guage thick walls to ensure mechanical robustness during high-pressure sCO2 flows at p_{sCO2} > 17 MPa.

The first HX core had fluidized bed channels with an average Δz_b = 12.7 mm in thickness, but changes in fabrication for the second HX core made the average $\Delta z_b \approx$ 10.4 mm, which lowers required gas flows for optimal $h_{T,w}$. With the sCO_2 microchannel walls and bounding walls, the full HX core depth was 0.214 m. The width of each bed channel is 0.2 m, and the spacer walls add 0.01 m on each side such that the total core width is 0.22 m. Figure 29 shows an assembly drawing and photo of the second HX core tested at NSTTF. The HX core height extends 0.4 m above the fluidizing gas injector ports to the top outlet of the sCO_2 vertical zig-zagged microchannels. VPE's proprietary sCO_2 manifold designs balance pressure across 130 microchannels per plate at the inlet and outlet and connect the manifolds on the HX core sides as shown in Fig. 29. An additional 0.09 m above and below the core is needed for the microchannel plates to incorporate flow distribution through inlet and exhaust manifolds which direct the heated sCO_2 in and out through curved passages into the two opposing pipes embedded in the sides of the core width. The total core height (0.58 m) gives an overall core volume under 28 liters. For the target 40 kW$_{th}$, the demonstration HX core transfers$\approx$ 1.45 kW$_{th}$ per liter.

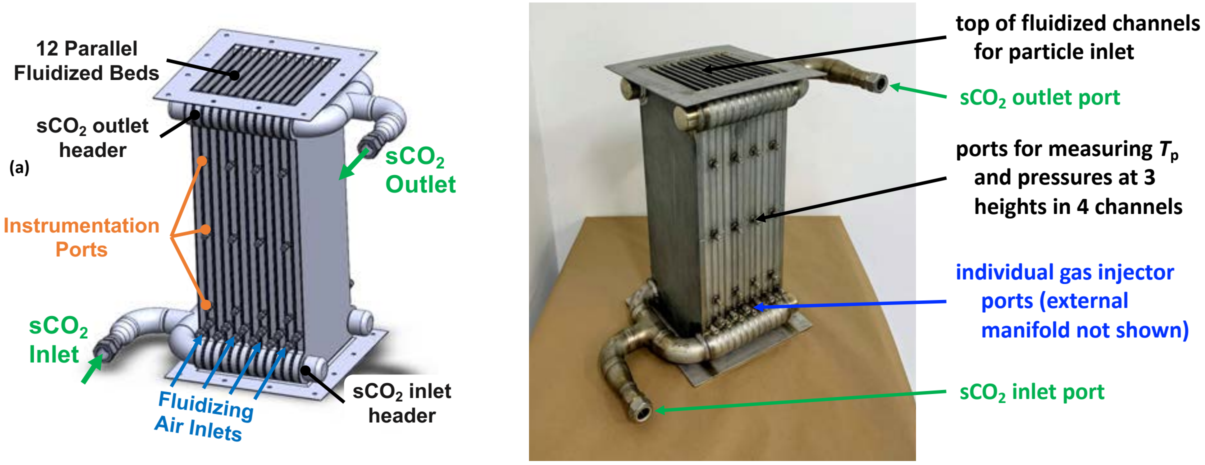

Figure 29: a) SolidWorks assembly drawing of prototype HX core with sCO_2 inlet and outlet manifolds at the top and bottom corners of the core, air injector ports just above the bottom sCO_2 inlet manifolds, and b) photo of the second HX core before delivery to Mines.

Fluidization is achieved with 6.35 mm OD injector tubes inserted across each channel near the bottom of the core as shown in Fig. 29, like the single-channel, heat transfer rig tests. The fluidized gas injectors are inserted at staggered heights in the core as shown in Fig. 29. Gas injection was tested at Mines in the single channel rig verified that uniform fluidization could be established with single injection ports on one side of the 0.1 m wide bed (half the width of the demonstration HX core). To explore the possibility of relying on single injection ports on one side of the 0.2 m wide beds of the demonstration bed, Mines developed a model for injector pressure drop for an injector with 500 evenly spaced orifices of diameter of 127 μm. Compressible flow models through orifices [71] predicted mass flow rates through the individual orifices as a function of location from the inlet port, and variation in orifice flow rates due to pressure drop along the 0.2 m length of the injector tube a variation in orifice mass flow rates vary by < 2% for total tube fluidizing gas flow rates ($\dot{m}_{\mathrm{g,in}} \approx 0.2$ g/s). National Jet provided injector tubes with the modeled geometry for the demonstration HX.

Mines completed construction and integration of the balance of plant components as shown in the assembly drawing and photo in Fig. 30. The assembly includes a free-board zone above the core where increased cross-sectional flow area in the freeboard zone lowers U_g and thus, the intensity of fluidization. A unique rotating scoop gate provides flow across the depth of the freeboard zone. The design of the freeboard zone cover enables reliable particle-gas separation with the gas flowing up through porous meshes in the air outlets as illustrated in Fig. 30a. Mild fluidization in the freeboard zone provides pressure equilibration at the inlet of all 12 fluidized bed channels. Room temperature tests of the effectiveness of maintaining some fluidization above the core in this zone demonstrated that the concept works well because the reduced U_g in the freeboard zone can be maintained at low $\hat{U}$ where fluidization is very mild.

Mines designed the feed hopper and the outlet hopper in consultation with Sandia to fit within the allowable height of the test facility at Sandia's NSTTF although some

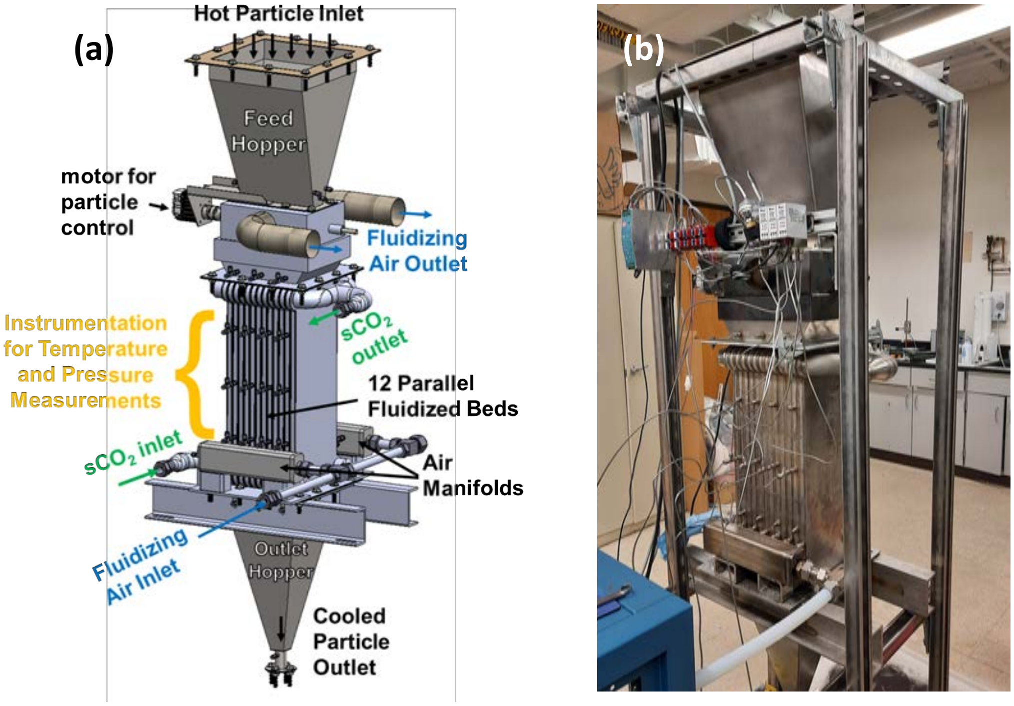

Figure 30: a) SolidWorks assembly drawing of the manifolds at the top and bottom corners of the core, the air injectors just above the bottom sCO_2 inlet manifolds, and an array of thermocouples and pressure taps to provide the basis for getting particle and wall temperatures and particle solid volume fraction vs. operating conditions. b) Photo of the HX core and the feed and outlet hoppers, the rotating scoop particle flow control, and instrumentation for room-temperature testing.

extensions on the outlet hopper exit forced Sandia to reduce the height of the transition to the outlet hopper to their outlet control gate to fit within the test stand at NSTTF. The hopper angles fall within guidelines regarding valley angle based on shear cell data for HSP 40/70 particles, but these measurements at room temperature underestimated the risk of funnel flow at higher $T_{p,in}$ when the particle have higher stiction. The bottom exit of the feed hopper (210 mm by 5 mm rectangle) can support $\dot{m}_{\mathrm{p,in}} > 0.45$ kg s^{-1}.

Particle flow into the fluidized bed HX is controlled by the angle of the scoop at the feed hopper exit. In the closed position, the scoop allows particles resting at their angle of repose to shut off flow behind the lip of a scoop as shown in Fig. 31. The scoop connects to an off-axis rotating shaft whose angle is controlled by a Teknic CPMV servo motor with a 10 to 1 gearbox (CGI) for finer control. The servo motor and gearbox were mounted outside of the hot particle flow path. The shaft passes through high temperature ceramic bushings to enable smooth rotation at high temperatures, and counterweights provide passive scoop closing to shutoff particle flow in the case of loss of system control. This rotary scoop avoids challenges with sliding gate mechanisms, which require high linear actuation forces and tight tolerances to overcome solid-to-solid friction forces, galling due to particles between moving components. The mechanism provides a particle curtain that spans the depth of the HX entrance as shown in Fig 31d) and 31e). Steady-state flow tests calibrated the particle flow rate as a function of motor position (i.e., scoop position) using a load cell underneath a collection bin. The scoop-enabled particle flow rate has a maximum feed hopper exit flow of 525 g s^{-1}. The scoop and shaft were oxidized along with the housing and maintained their shape and structural integrity for testing at temperature at NSTTF.

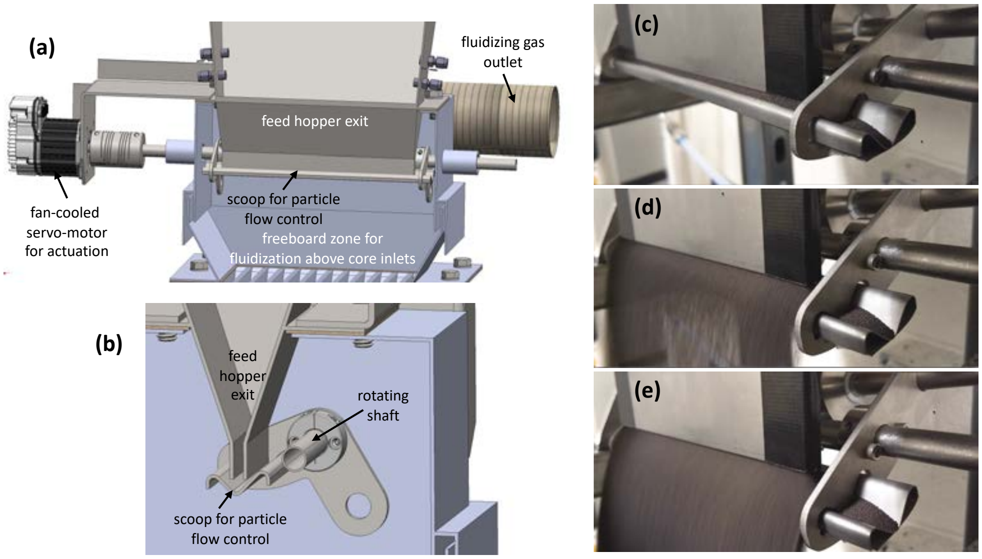

Figure 31: Solid model cutaway view of the particle flow control mechanism a) as viewed looking perpendicular to the scoop axis and b) parallel to the scoop axis. Photos of the particle scoop mechanism at the feed hopper exit c) in the closed position, d) in a partially opened position, and e) in the fully opened position.

The particle exit hopper below the HX core reduces from the cross section of the HX core and transitions from a square cone to a 1-inch schedule 10 pipe that matched the existing outlet particle flow control mechanism at the NSTTF. A 3 x 3 array of K-type sheathed thermocouples monitors outlet temperatures and uniformity of particles exiting the bottom of the HX core.

The demonstration HX is designed to operate with particles mildly fluidized in the freeboard zone. Pressure taps and thermocouples at the bottom of the freeboard zone assess the height of the fluidized bed (preferably 10 - 30 mm) in the freeboard zone. These measurements were used to manually adjust particle $\dot{m}_{\mathrm{p,in}}$ with the servo motor to keep the freeboard zone bed at a fixed height as determined by the pressure drop. Sandia provided the sliding control gate at the bottom of the exit hopper to control the $\dot{m}_{\mathrm{p}}$ through the HX core.

The 40-kW$_{\mathrm{th}}$ fluidized particle-sCO$_2$ HX was installed in the NSTTF test facility, which was upgraded with flow rates and operating temperatures presented in the right column of Table 4. Sandia installed a vertical particle skip hoist for automated recycling of particles from the collection hopper back to the electric particle preheater as shown in the facility photo in Figure 32. In addition, Sandia installed a recuperator and electric heater in the sCO$_2$ flow loop (as shown in Figure 32) that can provide $T_{\mathrm{sCO2,in}}$ > 400ºC. In addition, a new electronically controlled, pressured air supply with an air preheater supports fluidizing gas flows at temperatures to 400ºC for the fluidized bed HX tests.

Table 4: Flow capabilities for upgraded particle-sCO_2 HX test facility at NSTTF with increased sCO_2 and particle flow rates and added fluidized gas flow capabilities

Metric	sCO_2 flow	Particle flow	Fluidized gas flow
Flow rate	0 - 250 g/s	0 - 250 g/s	0 - 300 slpm
Temperature range	0 - 200°C	0 - 600°C (limited to 520°C due to heater)	0 - 250°C
Pressure range	up to 20 MPa	HX dependent	40 kPa

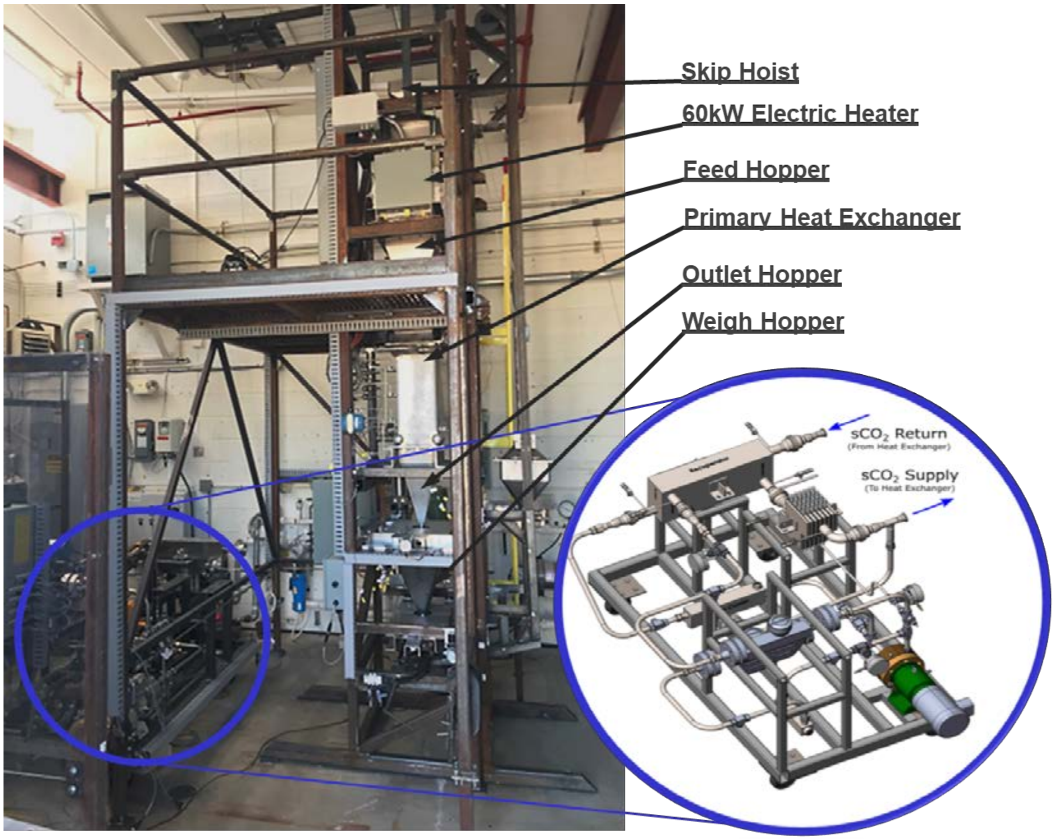

Figure 32: Labelled photograph of 40-kW_{th} fluidized bed particle-sCO_2 heat exchanger installed in the test facility at NSTTF at Sandia National Laboratories showing the particle skip hoist, the upstream particle electric heater and the outlet and weigh hoppers for measuring mass flow. The improved sCO_2 flow loop is shown in the assembly drawing to the right.

The NSTTF HX facility represents a small scale testbed for particle-sCO_2 HX prototypes. The test stand has seven different particle, CO_2, air, and glycol flow loops for precise control of system pressures, densities, flow rates, and temperatures as presented in the process flow diagram in Fig. 33. The particle flow loop is vertically integrated for creating gravity driven flow with heated particles passing through a large bank of electric cartridge heaters before entering the wegde feed hopper for the particle-sCO_2 HX core. The wedge feed hopper caused some funnel flow at higher $T_{p,in}$ and to protect the 60-kW_{elec} preheater from particle flow dead zones, $T_{p,in}$ was limited to 520ºC for the HX test campaign.

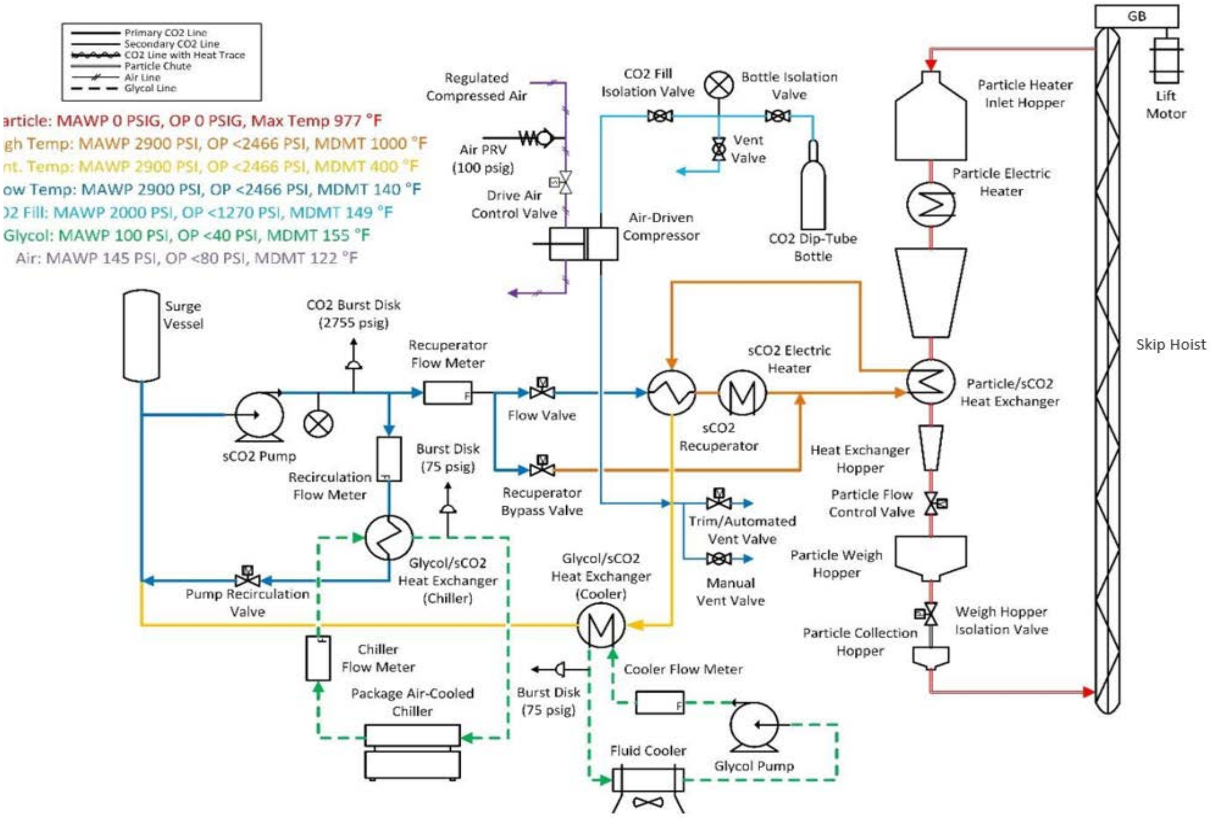

Figure 33: Process flow diagram for the particle-sCO$_2$ HX test facility at NSTTF with upgrades for improved particle and sCO$_2$ flow control and fluidization gas supply.

To start up, the sCO$_2$ flow loop is filled with CO$_2$ using 250 ft^3 K-type siphon tube bottles at 600 psig. A single stage, double acting gas booster with a 20:1 compression ratio for CO$_2$ service is used to increase the system pressure to supercritical values. Required supercritical pressure varies with atmospheric, system, and bottle temperatures, but generally supercritical conditions occur at 31 °C and 1071 psig. Density and flow are monitored with two inline Coriolis flow meters. When system pressures reach 1500 psig, sCO$_2$ density is typically above 850 kg/m^3 and a fluid flow pump is activated for circulation of sCO$_2$. Inline flow control valves are used in combination with the sCO$_2$ pump to vary the flow rates up to 250 g/s. Once circulating, sCO$_2$ temperatures are increased with a 20-kW$_{elec}$ heater with controlled variable power input. T_{sCO2} is monitored at the HX inlet with thermocouples. To control sCO$_2$ loop temperatures, multiple flow paths are available for outlet sCO$_2$ from the heat exchanger. Both inlet and outlet sCO$_2$ pass through the same recuperator, after which outlet sCO$_2$ can also pass through a glycol-cooled recirculation loop with both a glycol/sCO$_2$ cooler and chiller. Recuperator bypass and recirculation valves are used to control the flow rate of sCO$_2$ through these loops, influencing the inlet temperature of sCO$_2$ into the heat exchanger. Temperature control within the sCO$_2$ loop is achieved by manipulating heater power and flow configuration. Varying sCO$_2$ flow rate through the HX, the recirculation loops, and the recuperator bypass loop controls the $T_{sCO2,in}$ and $T_{sCO2,out}$.

The particle loop is electrically heated with a 60-kW_{elec} heater to provide $T_{p,in}$ up to 600 °C and flow rates of 250 g/s. The electric heater power is monitored for control of thermal inlet and particle temperature. Recirculation of the particle flow is accomplished using a skip hoist and collection bin. A skip hoist was selected for recirculation due to the higher operating temperature capabilities compared to screw augers and bucket elevators. The particle flow path from top to bottom consisted of an inlet hopper, a particle heater, a fluidized bed, the particle/sCO_2 heat exchanger, an outlet weigh hopper, and the particle collection bin. The particle flow rate is controlled at four points with the speed of the skip hoist and motorized slide gates at the fluidized bed, heat exchanger outlet, and the weigh hopper outlet. By varying the speed of the skip hoist and the position of the slide gates, the flow rate was controlled between 0-250 g/s. Other instrumentation included the weigh hopper for measuring particle flow rate. The fluidized bed was supplied with compressed air up to 300 slpm. An electric heater brought the fluidization gas up to 250°C.

Instrumentation in the test system mainly comprise of temperature, density, mass flow, and pressure measurements. Temperature readings at the inlet and outlet of all main components are collected and used for defining states of the system such as sCO_2 flow, recirculation, and recuperator bypass valve positions. Pressure is monitored across the heat exchanger and across various points in the sCO_2 flow loop. Vent valves and burst disks are in place to control the pressure and prevent a hazardous overpressure scenario.

5.2. Demonstration testing of the 40-kW_{th} particle-sCO_2 HX

Mines assembled the particle feed hopper, particle flow control with the rotating scoop gate, the particle exit hopper, and the air injectors with manifold into a room-temperature shakedown test stand. A single air manifold on one side of the HX core was installed to feed the injectors rather than two manifolds on opposite sides of the HX. Visualization of the freeboard zone from above the HX during room-temperature batch-mode fluidization tests above the heat exchanger core suggested no clear bias across the length of the injectors. For shakedown testing, Mines installed pressure transducers for the demonstration tests from Sandia such that 4 of the 12 parallel channels (channels 2, 5, 8 and 11) could be monitored for bed pressure drops Δp_g and thus α_p over the core height. fluidized bed channels are instrumented with 3 pressure/temperature taps such that these channels can be monitored for particle inventory based on average α_p and heat transfer based on rise in particle bed temperature ΔT_p. In these shakedown tests reported without heat transfer, only Δp_g and thus α_p could assess uniformity of inventory across the channels during filling and during steady-state batch mode operation. Because the feed hopper volume was only big enough to support ≈ 30 s of continuous flow, only heat exchanger filling experiments and batch mode fluidization tests were completed.

Above the HX core, the freeboard zone provided expansion in the gas flow area to reduce the superficial gas velocity U_g. The HX is designed to operate with a small number of particles mildly fluidized in the freeboard zone such that the curtain falling from the scoop feed rapidly distributes over the full cross-sectional area of this zone above. Pressure and temperature taps in the freeboard zone assess the height and temperature of the fluidized bed in the freeboard zone. Mines programmed a data acquisition program in NI LabView to read in Δp_g measurements and calculate α_p for all instrumented channels.

Measurements of Δp_g during HX core filling with HSP 40/70 with continuous fluidization were performed in two room-temperature experiments: 1) with two central channels fully instrumented such that evolution of the filling process could be observed for both channels, and 2) with four channels with Δp_b measurements at the bottom of the channel beds. Evolution of α_b during both filling experiments is measured at a near design $\dot{m}_{p,in} \approx 0.2$ kg s^{-1} with a constant $\hat{U} \approx 50$ in the channels. Figure 34 presents results from the first filling test with the two fully instrumented channels and shows a rise in particle inventory to a near steady average for the bottom, middle, and top regions of both channels with a fill time of approximately 2 min. The freeboard zone α_b represents the pressure drop associated with the height of the bed above the freeboard pressure taps. Results indicate < 10 s difference in filling times of the two channels. Figure 34c shows how gage pressure in the manifold and the channel bed itself rises during filling. Gauge pressure in the gas manifold exceeds 25 kPa at $\hat{U} = 50$ with ≈ 8-10 kPa coming from the bed and the mesh that blocks particles from escaping with air exhaust.

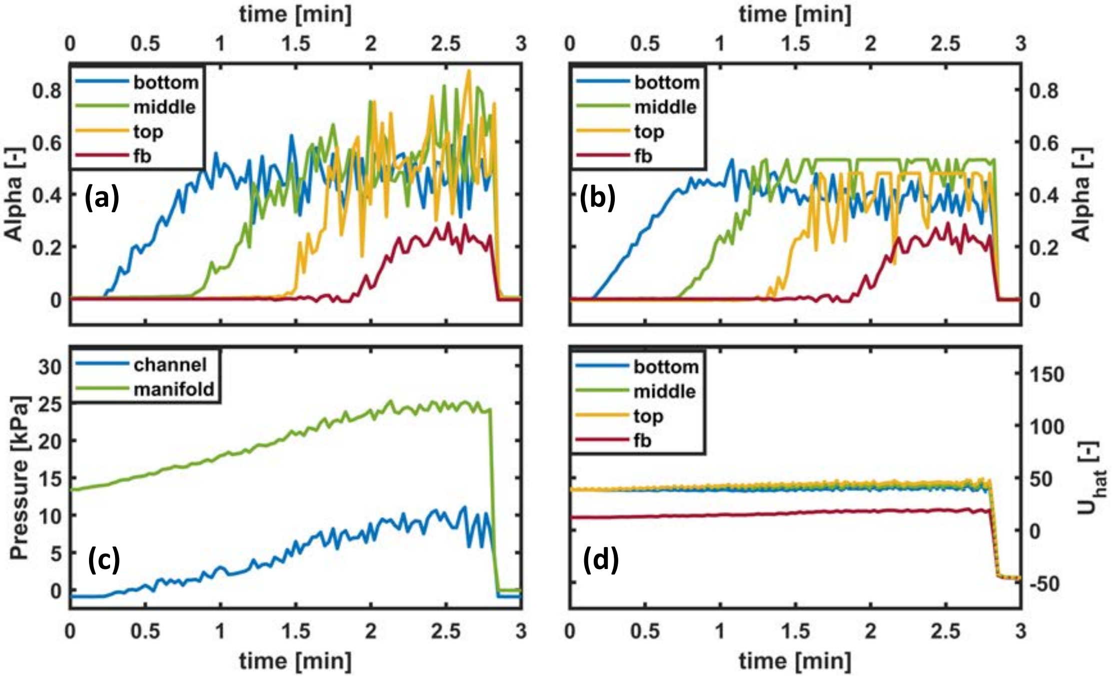

Figure 34: Plots of a) channel 5 and b) channel 8 α_b evolution during HX core fill test at $\dot{m}_{p,in} \approx 0.2$ kg s^{-1} and $\hat{U} \approx 50$. Plots show rising particle inventory in the channels as the bed height rises into freeboard (fb) zone above the bed. Measurements in channel 8 cut-off at $\alpha_b \approx 0.5$ due to limitations on maximum Δp of available transducer. c) gauge pressure in the fluidizing gas manifold and the bed channel as a function of 5, d) Plot of $\hat{U}$ in the channel and freeboard zone vs. time.

Shakedown testing of the fluidized-bed, particle-sCO$_2$ heat exchanger at NSTTF revealed several challenges in the original fabrication of the fluidized bed heat exchanger. Sandia had to redesign the exit of the outlet collection hopper because the height when assembly was too long. Sandia completed those modification and began room temperature tests which revealed leaks around some injectors and the bottom flange of the heat exchanger.

These leaks were significant because the air pressure below the injectors equaled the pressure to push the air up through the weight of the fluidized bed. Thus, the various leaks below the air injectors minimize the fraction of fluidization air that did not pass up through the bed. After initial low-temperature testing revealed the vertical meshes in the horizontal exhaust flows tended to collect particles and increase pressure within the freeboard zone, the air exhausts were turned upward and meshes in a horizontal direction were installed such that stray particles in the air would fall back into the freeboard zone. A slip joint with ceramic insulation seal above the freeboard zone permitted independent vertical growth of the HX and the electric preheater and feed hopper above the HX core.

Early low-T_p tests at the NSTTF showed that particle inventory in the HX core could be sustained by monitoring p_g in the freeboard zone and adjusting the rotary scoop inlet valve to supply particle flow into the freeboard zone that closely matched the particle flows out through the outlet hopper exit valve. The need for two flow control valves differs from moving packed bed designs, which use a single particle flow control at the HX outlet hopper. These early tests further confirmed the relatively uniform fluidization through the bed but now under conditions with downward particle flow rates.

The fluidized bed HX tests at NSTTF operated initially with $T_{p,in} \leq 440°C$ but otherwise at the test conditions listed in Table 5 using the smaller HSP 45/60 particles. The particle inlet mass flow rate $\dot{m}_{p,in}$ varied from 0.10 to 0.20 kg s^{-1} whilst the sCO$_2$ flow rate was generally fixed at $\dot{m}_{sCO2,in}$ = 0.20 kg s^{-1} and the fluidizing gas flow rate was varied to give desired $\hat{U}$ and $\dot{m}_{g,in}$ was usually set to £ 0.005 kg s^{-1}. Tests near the end of the campaign raised $\dot{m}_{p,in}$ and $\dot{m}_{sCO2,in}$ to 0.24 kg s-1 to explore how overall heat transfer and axial dispersion were influenced by higher particle flow rates.

Figures 35 and 36 show how mass flow rates, pressure drops, and temperatures in the demonstration HX evolve with time during a typical test with HSP 45/60 particles at steady-state $T_{p,in} \approx 430°C$ and $T_{sCO2,in} \approx T_{g,in} \approx 200°C$. As seen in Fig. 35, test conditions start with a relatively high $\dot{m}_g$ corresponding to a $\hat{U} \approx 36$ and then after reaching steady state, $\dot{m}_g$ (i.e., $\hat{U}$) are incrementally decreased down to $\hat{U} \approx 5$. The incremental decrease in $\hat{U}$ lowers axial dispersion in the HX core and thus, results in less back mixing to the

Table 5: Fluidized bed particle-sCO$_2$ HX actual test and design flow conditions for the demonstration tests at NSTTF.

HX Flows	Property	Tested conditions	Design test conditions
CARBOBEAD HSP particles	mean diam. $d_{p,mean}$	333 mm	360 mm
	bulk density r_p	3650 kg m^{-3}	3650 kg m^{-3}
	inlet temp., $T_{p,in}$	≤ 520°C	≤ 600°C
	mass flow rate, $\dot{m}_p$	≤240 g s^{-1}	≤ 250 g s^{-1}
fluidizing air	inlet temp., $T_{g,in}$	≤ 320°C	≤ 400°C
	mass flow rate, $\dot{m}_g$	≤ 5.3 g s^{-1}	2.0 to 4.0 g s^{-1}
supercritical CO$_2$	inlet temp., $T_{sCO2,in}$	320°C	400°C
	mass flow rate, $\dot{m}_{sCO2}$	≤ 240 g s^{-1}	250 g s^{-1}
	inlet pressure, $P_{sCO2,in}$	17 MPa	17 MPa

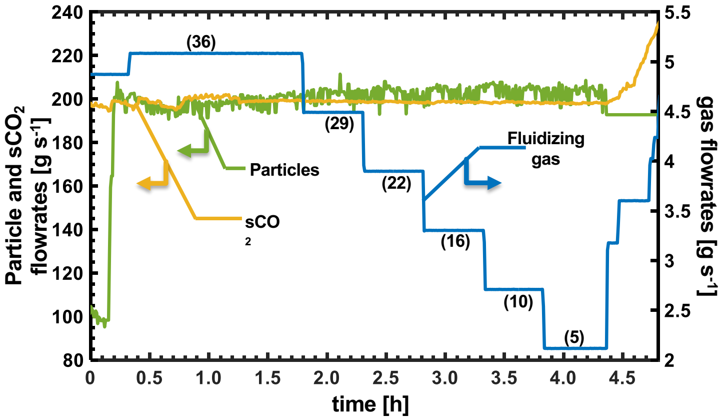

Figure 35: Particle, sCO$_2$ and fluidizing gas mass flow rates for a test of the demonstration particle-sCO$_2$ HX using HSP 45/60 with varying $\hat{U}$ as indicated for each jump in gas flow by the number in parentheses. Steady inlet temperatures after t = 1.0 h were $T_{sCO2,in} \approx T_{g,in} \approx 200$°C and $T_{p,\,in} \approx 430$°C.

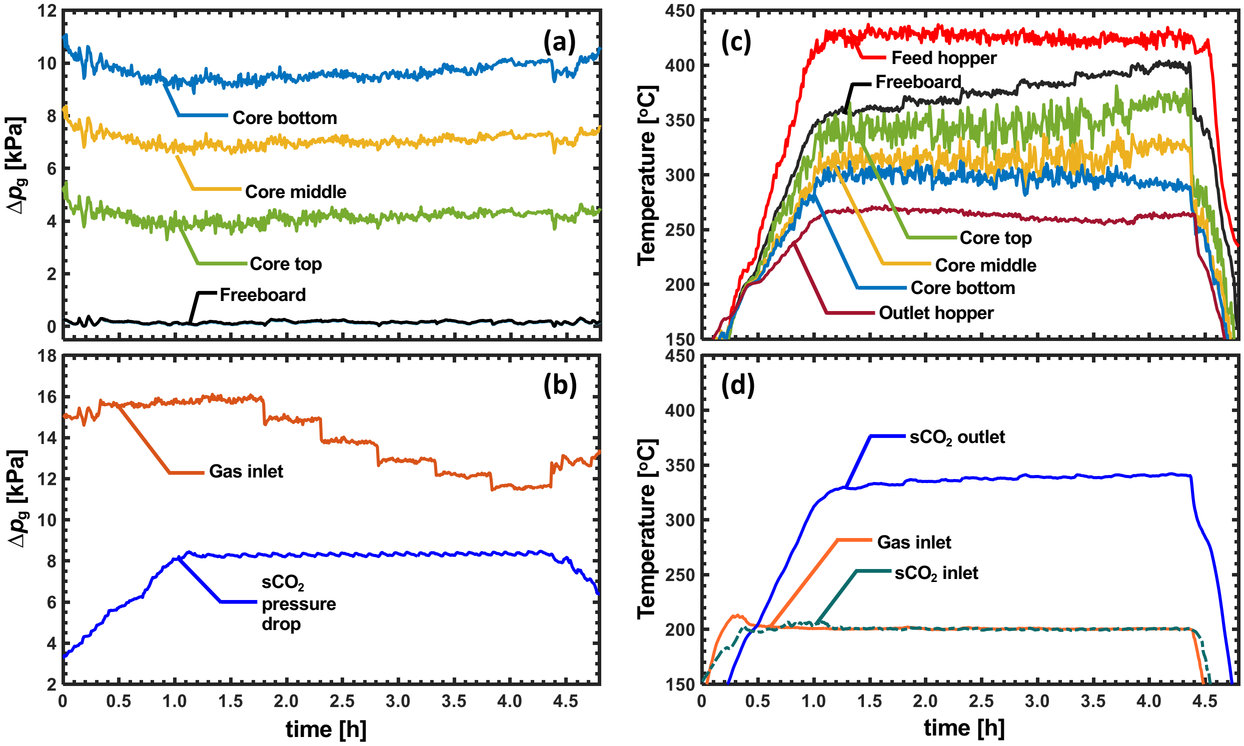

Figure 36: a) Typical variation in pressure drops, Δp_g during a HX test using HSP 45/60 at fixed $\dot{m}_p$» 0.20 kg s^{-1} and $\dot{m}_{sCO2}$» 0.20 kg s^{-1} during startup and steady-state. b) Plots of gas injector manifold upstream gage pressure and sCO$_2$ upstream gage pressure during HX operation with $\dot{m}_g$dropping in increments over time to lower $\hat{U}$. c) Variation in T_p values from the feed hopper to the outlet hopper The step changes up in the freeboard zone $T_{p,fb}$ coincides with reductions in fluidizing gas flow rates $\dot{m}_g$and thus a reduction in $\hat{U}$. d) Variation in $T_{sCO2,in}$, $T_{sCO2,out}$, and $T_{g,in}$ during a typical HX test. The increases in $T_{sCO2,out}$ indicate that the reduction in $\hat{U}$ lowers axial dispersion and causes an improvement in LMTD that more than offsets drops in $h_{T,w}$ at lower $\hat{U}$.

freeboard zone. Thus, as $\hat{U}$ decreased, $T_{\mathrm{p,fb}}$ increased closer to $T_{\mathrm{p,in}}$. as shown in Fig. 36c. Figure 36d shows that with the reduced back mixing also increased $T_{\mathrm{sCO2,out}}$ indicating an increase in overall heat transferred to the sCO$_2$, $\dot{Q}_{\mathrm{HX}}$. This arises even though the single-channel tests establish well that $h_{\mathrm{T,w}}$ will decrease significantly as $\hat{U}$ decreases from 36 to 5 as shown in Fig. 35. The effective overall heat transfer coefficient U_{eff} for a given test condition based on the feed hopper inlet $T_{\mathrm{p,in}}$ is derived from eq. 12 where h_{sCO2} represents the specific enthalpy of sCO$_2$ which is derived from T_{sCO2} and p_{sCO2} using the CO$_2$ thermodynamics of Span and Wagner [65].

$$\begin{aligned}\dot{Q}_{\mathrm{HX}} &= \dot{m}_{\mathrm{sCO2}}\left(h_{\mathrm{sCO2,out}} - h_{\mathrm{sCO2,in}}\right)\\ &= U_{\mathrm{eff}} A_{\mathrm{w,tot}}\left[\frac{\left(T_{\mathrm{p,in}} - T_{\mathrm{sCO2,out}}\right) - \left(T_{\mathrm{p,out}} - T_{\mathrm{sCO2,in}}\right)}{\ln\left(\left(T_{\mathrm{p,in}} - T_{\mathrm{sCO2,out}}\right)/\left(T_{\mathrm{p,out}} - T_{\mathrm{sCO2,in}}\right)\right)}\right]\end{aligned} \qquad \text{(eq. 12)}$$

The term in square brackets in eq. 12 represents the effective overall log mean temperature difference ($LMTD_{\mathrm{eff}}$). This U_{eff} based upon $T_{\mathrm{p,in}}$ provides a metric for HX performance that allows for comparison of the fluidized-bed particle-sCO$_2$ HX with similarly applied moving packed bed HX. All the same, U_{eff} does not reflect the value that would be derived by using eq. 9 to define U because a more representative $LMTD_{\mathrm{fb}}$ in the core would be based on the freeboard temperature $T_{\mathrm{p,fb}}$, which represents the actual particle temperature entering the fluidized bed channels. This leads to an alternative definition of U (i.e., U_{fb}) that is more closely tied to the definition of U in eq. 9 and tied more directly to the average particle-wall $h_{\mathrm{T,w}}$.

$$\dot{Q}_{\mathrm{HX}} = U_{\mathrm{fb}} A_{\mathrm{w,tot}}\left[\frac{\left(T_{\mathrm{p,fb}} - T_{\mathrm{sCO2,out}}\right) - \left(T_{\mathrm{p,out}} - T_{\mathrm{sCO2,in}}\right)}{\ln\left(\left(T_{\mathrm{p,fb}} - T_{\mathrm{sCO2,out}}\right)/\left(T_{\mathrm{p,out}} - T_{\mathrm{sCO2,in}}\right)\right)}\right] \qquad \text{(eq. 13)}$$

The $LMTD_{\mathrm{fb}}$ based on $T_{\mathrm{p,fb}}$ in eq. 13 is lower than $LMTD_{\mathrm{eff}}$ based on $T_{\mathrm{p,in}}$ in eq. 12, and this shows how axial dispersion due to fluidization negatively impacts particle-sCO$_2$ HX performance by mixing cooler particles from within the core with incoming particles from the feed hopper, thereby lowering $LMTD_{\mathrm{eff}}$ and $\dot{Q}_{\mathrm{HX}}$. As seen in Figs. 35c) and 35d), the rise in $T_{\mathrm{p,fb}}$ with lower $\hat{U}$ at later times led to an increase in $LMTD_{\mathrm{fb}}$ that more than offset the reduction in the overall U_{fb} and resulted in a slight increase in $\dot{Q}_{\mathrm{HX}}$.

The energy balance within the HX for the tests in Figs. 35 and 36 closes to within 2 to 3% with only a very small fraction (≈ 1%) of the thermal energy extracted from the particles going to fluidizing air flow. The plots in Fig. 37 shows the energy balance for that particular test and indicate that the target of $\dot{Q}_{\mathrm{HX}}$ = 40 kW$_{\mathrm{th}}$ was not achieved at these lower $T_{\mathrm{p,in}} \approx 430$°C despite the low $T_{\mathrm{sCO2,in}} \approx 200$°C. The particle mass fluxes $\dot{m}_p''$ = 7.9 kg m^{-2} s^{-1} were below expected values and subsequent tests, discussed below, with higher $\dot{m}_p''$ were able to achieve the targeted $\dot{Q}_{\mathrm{HX}}$ = 40 kW$_{\mathrm{th}}$. The ≈1% energy loss to the gas shows how the bubbling fluidization has a very minor impact upon the effectiveness of the energy recovery to the sCO$_2$ in the fluidized bed particle-sCO$_2$ HX. This commonly expressed concern regarding fluidized bed HXs for TES fails to recognize how small gas flows are needed to drive significant improvements in particle-wall heat transfer. Furthermore, with the negative impact of dispersion at higher $\hat{U}$, preferred operating conditions will likely be only slightly above the flow rate required for minimum fluidization.

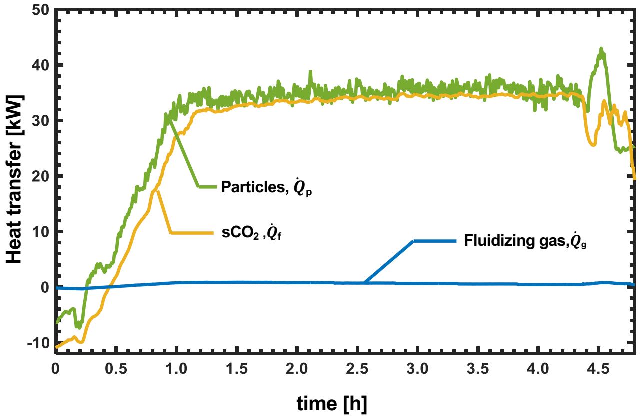

Figure 37: Thermal energy transfer in the particle-sCO_2 HX tests using HSP 45/60 with varying $\hat{U}$ for $T_{\mathrm{sCO2,in}} \approx T_{\mathrm{g,in}} \approx 200$°C and $T_{\mathrm{p,in}} \approx 430$°C after steady state at $t = 1.0$ h.

Some tests on the demonstration particle-sCO_2 HX that looked at how variations in $\dot{m}_{\mathrm{p}}$ for fixed $\dot{m}_{\mathrm{sCO2}}$. Fig. 38a shows how T_{p} in the HX rose with time through the bed as $T_{\mathrm{p,in}}$ increased from 200°C to 400°C and the particle mass flow increased from an initially low $\dot{m}_{\mathrm{p,in}} \approx 0.10$ kg s^{-1} for the first 90 min after which $\dot{m}_{\mathrm{p,in}}$ was raised to ≈ 0.15 kg s^{-1} until 135 min. After that increase, $\dot{m}_{\mathrm{p,in}}$ was increased to ≈ 0.20 kg s^{-1}. The large temperature difference between the feed hopper and the freeboard zone $T_{\mathrm{p,in}} - T_{\mathrm{p,fb}}$ in Fig. 38a is a result of the axial dispersion associated with fluidization. $T_{\mathrm{p,in}} - T_{\mathrm{p,fb}}$ drops from ≈100°C at $\dot{m}_{\mathrm{p,in}} = 0.1$ kg s^{-1} to close to 60°C at $\dot{m}_{\mathrm{p,in}} = 0.2$ kg s^{-1} likely because the increased downward particle mass flux reduces the back mixing of dispersion caused by bubbling fluidization. The temperatures within the HX sections are close together from the top to the bottom with a bigger difference in temperature between the bottom of the HX below the injector and the outlet hopper. In that region, particles act as a moving packed bed without fluidization, but also with very low axial dispersion.

With each increase in $\dot{m}_{\mathrm{p}}$, overall heat transfer to the sCO_2 $\dot{Q}_{\mathrm{HX}}$ increases reaching a maximum of 34.0 kW_{th}. The increase with $\dot{m}_{\mathrm{p}}$ is driven in part by reduced dispersion and the associated increase in log-mean temperature difference $LMTD_{\mathrm{fb}}$ based on $T_{\mathrm{p,fb}}$ in eq. 13. Studies in the single-channel test rig showed that $h_{\mathrm{T,w}}$ and thus overall U_{fb} should not change significantly with higher $\dot{m}_{\mathrm{p}}$ in this range, but the higher $\dot{m}_{\mathrm{p}}$ keeps T_{p} higher across the height of the HX, and thus may indirectly raise $h_{\mathrm{T,w}}$ and thus, U_{fb}. This increase in $\dot{m}_{\mathrm{p}}$ does lower HX effectiveness $\varepsilon_{\mathrm{HX}}$ to 0.65, well below the milestone target value of 0.80.

U_{fb} values can be used to estimate an average $h_{\mathrm{T,w}}$ in the narrow-channel beds (including the fluidized regions and the packed bed region beneath the injectors).

$$h_{\mathrm{T,w}} \approx \left[1/U_{\mathrm{fb}} - \Delta z_{\mathrm{w}}/\lambda_{\mathrm{w}} - 1/h_{\mathrm{T,sCO2,eff}}\right]^{-1} \qquad [14]$$

Average particle wall $h_{\mathrm{T,w}}$ is estimated using an effective $h_{\mathrm{T,sCO2,eff}} \approx 2000$ W m^{-2} K^{-1} based on VPE's design. An estimate for $h_{\mathrm{T,w}}$ from eq. 14 is 325 W m^{-2} K^{-1} for the HX at $\dot{m}_{\mathrm{p,in}} =$ 0.2 kg s^{-1}, which is lower than values observed in the single channel test rig at Mines. This may in part be because of the 17% of $A_{\mathrm{w,tot}}$ is exposed to a moving packed bed. $h_{\mathrm{T,w}}$ would increase with higher T_{p} characteristic of a primary HX for sCO_2 Brayton cycle.

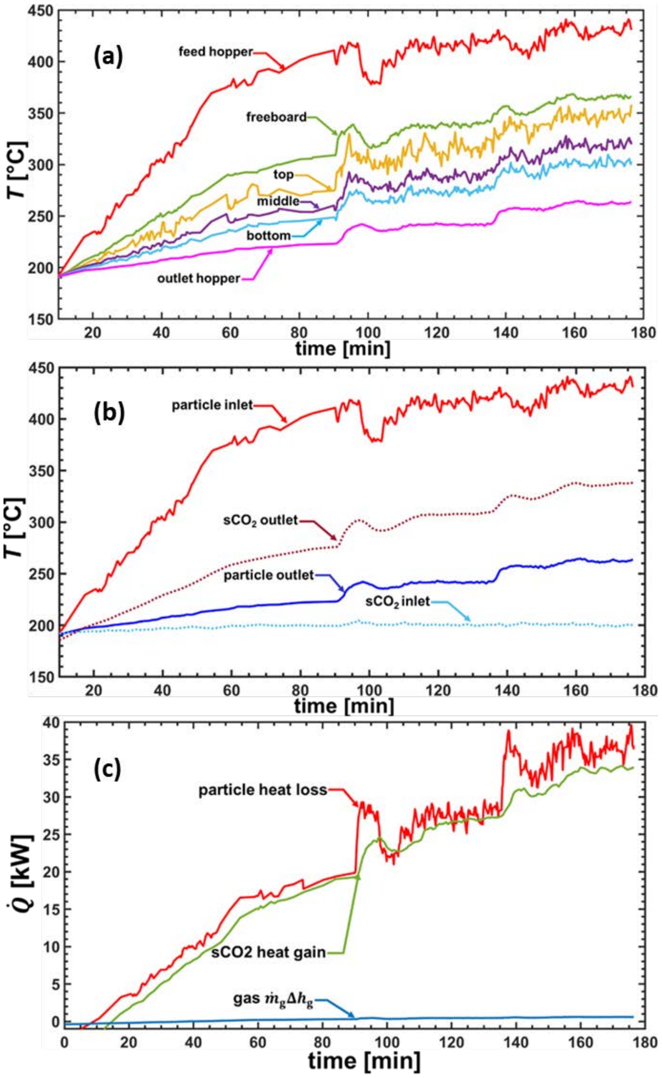

Figure 38: a) Average T_p in the feed and outlet hopper, the freeboard zone, and across the instrumented channels in the fluidized-bed, particle-sCO$_2$ HX during testing at the NSTTF. Flow conditions followed those listed in the third column of Table 1 with $\dot{m}_p \approx$ 0.1 kg s^{-1} for the first 90 min., $\dot{m}_p \approx$ 0.15 kg s^{-1} for the next 45 min. and the design flow rate $\dot{m}_p \approx$ 0.2 kg s^{-1} for the final 45 min. b) Average $T_{p,in}$ leaving the feed hopper. $T_{p,out}$ entering the outlet hopper, and $T_{sCO2,in}$ and $T_{sCO2,out}$ during the same tests. c) Energy balance in particle-sCO$_2$ HX showing the heat transferred from the solid particle flow, into the supercritical carbon dioxide, and fluidizing gas.

Over the latter half of 2022 and early in 2023, numerous demonstration tests were run for the 40-kW$_{th}$ fluidized bed particle-sCO$_2$ HX primarily with HSP 45/60 particles although a few cases were run with the larger HSP 40/70. The most common condition was $\dot{m}_p \approx$ 0.2 kg s^{-1} and $\dot{m}_{sCO2} \approx$ 0.2 kg s^{-1} with $T_{p,in} \approx 430^\circ$C and $T_{sCO2,in} \approx T_{g,in} \approx 200^\circ$C. Table 2 summarizes the numerous steady-state points of HX operation over a 10 min averaging

Table 6: Summary of fluidized bed particle-sCO$_2$ HX steady-state test results at the stated test condition (for > 10 min) using HSP 45/60 or HSP 40/70 (shaded rows).

$\dot{m}_\mathrm{p}$ [g s^{-1}]	$\dot{m}_\mathrm{sCO2}$ [g s^{-1}]	$\dot{m}_\mathrm{g}$ [g s^{-1}]	$T_\mathrm{p,in}$/$T_\mathrm{p,out}$ [°C]	$T_\mathrm{sCO2,in}$/$T_\mathrm{sCO2,out}$ [°C]	LMTD [°C]	$\dot{Q}_\mathrm{HX}$ [kW$_\mathrm{th}$]	U_eff [W m^{-2} K^{-1}]	ε_HX [-]
202	205	4.9	97/32	24/44	24.5	10.0	155	0.78
202	198	5.5	212/52	27/80	63.8	28.3	168	0.77
101	199	4.9	315/113	101/159	55.3	20.6	141	0.91
148	198	4.9	301/124	100/176	60.0	25.7	162	0.83
149	198	4.9	310/125	101/182	62.7	26.8	162	0.82
198	199	4.9	264/125	100/167	52.6	23.2	167	0.70
197	198	4.9	329/144	100/212	75.0	35.3	178	0.74
198	198	5.9	339/154	101/216	82.3	35.9	165	0.71
98	199	4.9	407/224	200/273	64.1	18.5	109	0.82
151	199	4.9	416/247	200/307	73.1	26.7	138	0.74
203	199	4.9	424/268	201/331	79.4	32.3	154	0.64
198	200	4.9	422/263	201/325	78.2	31.0	150	0.64
199	199	5.1	428/269	201/332	81.7	32.6	151	0.65
202	199	4.5	429/267	201/336	79.1	33.5	160	0.65
202	199	3.9	426/264	200/338	75.3	34.0	171	0.67
203	199	3.3	425/259	200/339	71.6	34.4	182	0.68
204	198	2.7	423/258	200/340	69.7	34.5	187	0.68
203	198	2.1	425/263	200/341	72.2	34.6	181	0.68
200	199	4.2	517/367	300/427	77.6	30.8	150	0.61
202	198	3.0	518/362	300/435	71.6	32.6	172	0.64
201	198	1.7	523/365	300/442	72.9	34.1	177	0.65
200	199	4.2	431/264	201/333	79.1	32.6	156	0.64
201	222	4.2	428/257	200/324	78.5	34.9	168	0.68
201	248	4.2	422/250	200/312	76.1	34.6	172	0.70
201	200	2.2	412/260	200/329	70.1	32.1	173	0.69
198	200	3.8	425/262	200/333	75.6	33.0	165	0.67
198	199	4.5	428/267	200/333	80.6	32.8	154	0.65
198	198	5.3	435/272	200/333	85.9	32.7	144	0.63
251	247	1.5	424/308	200/310	110.4	33.9	116	0.54
250	246	2.2	413/266	200/322	78.1	37.4	181	0.64
250	248	2.9	423/262	200/331	76.3	40.6	201	0.66
246	248	3.7	427/264	199/330	79.7	40.5	192	0.65
247	247	4.4	431/267	199/329	83.5	40.2	182	0.63
246	247	5.2	435/272	199/329	88.7	40.1	171	0.62
103	202	5.3	401/224	200/275	60.9	19.0	118	0.84
199	199	5.3	410/259	201/321	73.1	29.8	154	0.65
202	198	4.3	412/258	200/327	70.3	31.2	168	0.66
202	198	3.4	414/255	201/330	67.8	32.0	179	0.67
201	198	2.4	413/266	200/329	74.9	31.8	161	0.67

when flow conditions remained constant. The number of tests is indicative of relatively robust operation of the multi-channel fluidized bed HX by controlling the particle inventory with pressure drop in the freeboard zone. Trends in Table 2 are not particularly easy to visualize, but the following bulleted list highlights some key insights gained from the data.

- The particle-sCO$_2$ HX operates stably over a range of $\dot{m}_g/\dot{m}_p$ ratios and can achieve the milestone target $\dot{Q}_{\mathrm{HX}}$ of 40 kW$_{th}$ with HSP 45/60 at $\dot{m}_p \approx 0.25$ kg s^{-1} and $\dot{m}_{sCO2} \approx 0.25$ kg s^{-1} with inlet conditions $T_{p,in} \approx 430°C$ and $T_{sCO2,in} \approx T_{g,in} \approx 200°C$.
- Simultaneously increasing $T_{p,in}$ from 430°C to 520°C and $T_{sCO2,in}$ from 200°C to 300°C does not have a marked change in HX performance either with respect to $\dot{Q}_{\mathrm{HX}}$ or U_{eff}.
- Overall heat transfer coefficient U_{eff} based on $T_{p,in}$ remains very low reaching a maximum of ≈ 200 W m^{-2} K^{-1} for the higher $\dot{m}_p \approx 0.25$ kg s^{-1} and $\dot{m}_{sCO2} \approx 0.25$ kg s^{-1} and at low fluidization $\dot{m}_g \approx 1.2\%$ of $\dot{m}_p$. U_{eff} remain far below desired values > 600 W m^{-2} K^{-1}.
- For plain wall fluidized bed channels, there is a significant trade-off with respect to excess fluidization velocity as characterized by the non-dimensional $\hat{U}$. Lower $\hat{U}$ down to a minimum value > 5 improves the fluidized bed log-mean temperature difference $LMTD_{fb}$ but lowers the U_{fb} due to poorer particle-wall $h_{T,w}$.

Efforts were pursued to see how T_p and $\dot{m}_p$ might impact the observed trade-offs between increasing U_{fb} while simultaneously decreasing $LMTD_{fb}$ with higher $\hat{U}$. The test results from Table 6 are further summarized in Fig. 39 which plots various performance metrics notably $\dot{Q}_{\mathrm{HX}}$, ε_{HX}, U_{eff}, U_{fb}, as a function of $\hat{U}$ for all the different test conditions listed in Table 6. The symbols in Fig. 39 are colored by the particle mass flow $\dot{m}_p$ to elucidate trends in performance metrics with increasing $\dot{m}_p$. For example, clearly $\dot{Q}_{\mathrm{HX}}$ does not greatly change with $\hat{U}$ except at very low values < 5 when $\dot{Q}_{\mathrm{HX}}$ drops off due to minimal or no fluidization. At higher $\hat{U}$, the tradeoff between higher $h_{T,w}$ and more axial dispersion keep $\dot{Q}_{\mathrm{HX}}$ relatively constant. On the other hand, the symbols show the significant increase in $\dot{Q}_{\mathrm{HX}}$ with higher $\dot{m}_p$ as expected. However, the increase in $\dot{Q}_{\mathrm{HX}}$ is not linear with $\dot{m}_p$, and thus HX effectiveness ε_{HX} falls with increasing $\dot{m}_p$ as shown in Fig. 39b.

The plots in Figs. 39c and 39d show how the different definitions of the HX overall heat transfer coefficient U_{HX} and U_{fb} behave very differently with respect to $\hat{U}$. Both increase with higher $\dot{m}_p$ because higher particle flow rates maintain higher T_p throughout the bed. However, because increasing $\hat{U}$ lowers the freeboard zone $T_{p,fb}$ due to axial dispersion the effective heat flux q_w between the particles and the sCO$_2$ drops. U_{HX} does not account for the change in $T_{p,fb}$ and thus just accounts for this by having a lower value. On the other hand, U_{fb} uses $T_{p,fb}$ in the $LMTD$ and thus actually increases with $\hat{U}$ because the particle-wall $h_{T,w}$ does increase significantly as $\hat{U}$ rises from 5 to 40. According to the single channel test rig data, this can be by as much as 4×. Because the other two thermal resistances for the HX do not change with $\hat{U}$, the value for U_{fb} only increases by about 40% over that range of $\hat{U}$ which is not enough to overcome the drop in $LMTD_{fb}$.

The HX test results were disappointing because axial dispersion suppressed the effective *LMTD* and thus did not allow for the HX to take advantage of the significant increase in $h_{T,w}$ associated with mild fluidization. It does appear to be clear that a very small amount

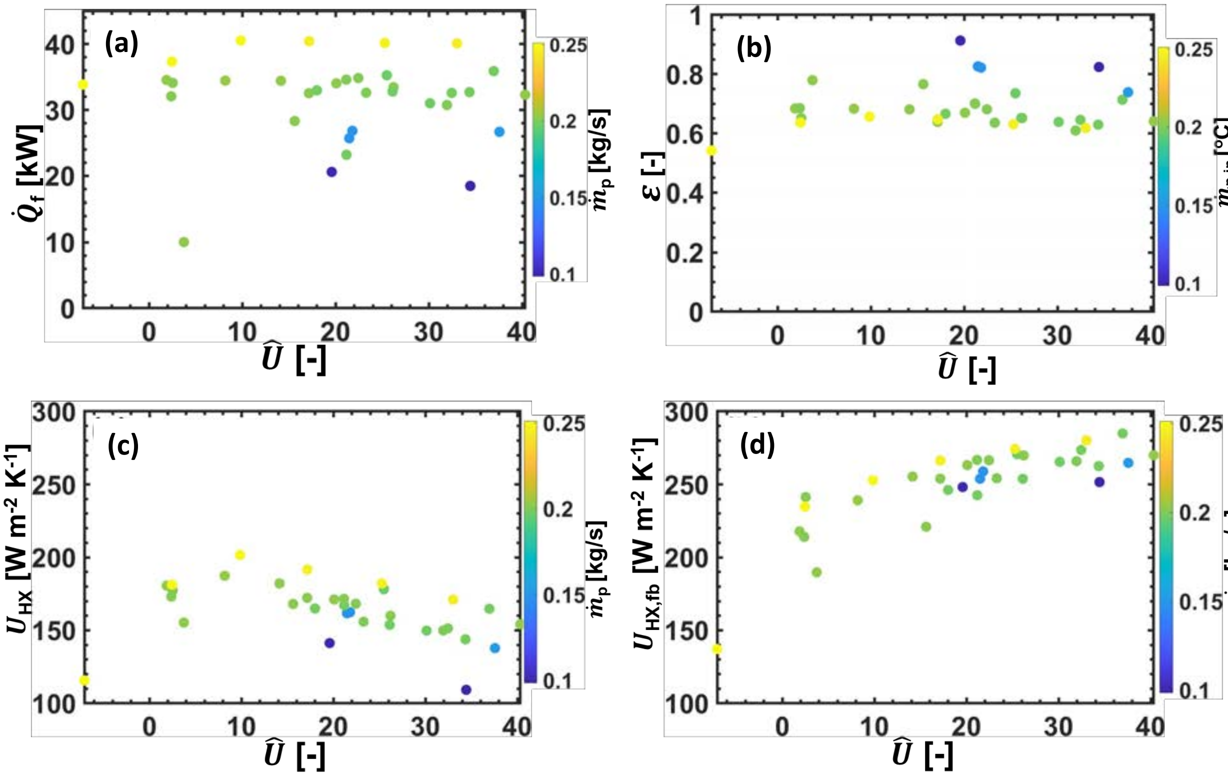

Figure 39: Fluidized bed particle-sCO$_2$ HX performance metrics – notably $\dot{Q}_{\mathrm{HX}}$, $\varepsilon_{\mathrm{HX}}$, U_{eff}, U_{fb}, as a function of non-dimensional excess fluidization velocity $\hat{U}$ for all the different test conditions listed in Table 6. Symbols are colored by the particle mass flow $\dot{m}_p$ to elucidate trends in performance metrics with increasing $\dot{m}_p$.

fluidization improves $\dot{Q}_{\mathrm{HX}}$ over none for the wide bed depth used in this study, but these improvements as shown in Fig. 39a. These results also place an importance on updating the 1-D models with well calibrated models of axial dispersion coefficient D_{sv}. To this end, the freeboard zone temperature drop from the inlet temperature ($T_{p,in} - T_{p,fb}$) provides a measure of back mixing that can be used to estimate the axial dispersion coefficient by using an energy balance of flows coming up from the inner bed temperature to mix with the inlet flows. Energy balances performed on the freeboard zone for the range of test conditions in Table 6 provided a basis for calculating D_{sv} at the top of the bed. Figure 40 plots the calculated D_{sv} at the top of the bed vs. $\hat{U}$ with the symbols colored as a function of $\dot{m}_p$. The plots show significant scatter but also for two different sets of tests at higher and lower $\dot{m}_p$ there is a linear trend between D_{sv} and $\hat{U}$, which would be consistent with the model of a constant dispersion Peclet number based on excess fluidization velocity [68]. The resulting slopes for the two fits in Fig. 40 give D_{sv} values that are reasonable. The offset for the linear fit for the lower $\dot{m}_p$ cases may be due to offsets in minimum fluidization velocities at those low flow rates. All the same, the values for D_{sv} are reasonable and there are significant efforts to add more fitting to measurements in the single-channel test rig to get a robust model for D_{sv} that can be put into the 1-D models.

The impact of D_{sv} on q_w was underestimated at the start of this project. Efforts are ongoing to extract values of D_{sv} from the two-fluid 3D CFD models, and between those studies

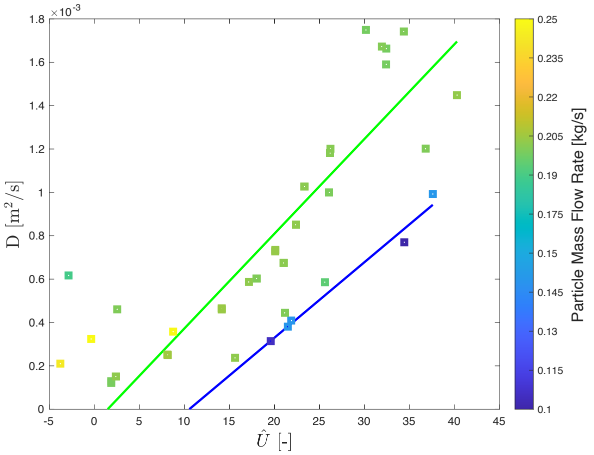

Figure 40: Plots of the vertical axial dispersion coefficient D_{sv} as a function of $\hat{U}$ for all the test conditions listed in Table 6. Symbols are colored by the particle mass flow $\dot{m}_p$ and two linear fits are provided for data at higher $\dot{m}_p$ in green and lower $\dot{m}_p$ in blue.

and the ongoing fitting of experimental measurements of freeboard zone temperatures with energy balance equations including axial dispersion, a more robust of 1-D reduced order model will provide a measure for better assessing what conditions can be used to mitigate the negative impact of D_{sv} on HX and to a lesser extent indirect receiver performance.

6. Summary

6.1. Significant Accomplishments and Conclusions:

This project has led to a much deeper appreciation for the benefits and challenges to mild bubbling fluidization on high-temperature particle-wall heat transfer to benefit primary HX and indirect particle receiver performance for CSP plants with TES subsystems. While the project demonstrated pathways with smaller particles $d_{p,mean}$ < 250μm to achieve $h_{T,w}$ = 1000 W m^{-2} K^{-1} with the potential for overall $\underline{U_{HX}}$ > 600 W m^{-2} K^{-1}, issues associated with axial dispersion may prevent such high overall U_{HX}. The extensive heat transfer data sets with different oxide particles obtained from the single-channel test rig at Mines provided a correlation adopted from the work of Molerus that provides a reliable assessment for calculating $h_{T,w}$ at conditions relevant for primary HX in TES subsystems and for lower-temperature operation in indirect particle receivers. This work is being published for broader dissemination this year.

Mines and Sandia in collaboration with VPE demonstrated that a multi-channel fluidized bed HX can operate reliably and effectively to exchange heat with sCO_2 microchannels in a plate-to-plate diffusion bonded HX. The operation of a unique scoop gate provided a low-friction path for reliably depositing particles into a controlled freeboard zone above the HX core, which supported continuous particle flow through all 12 parallel channel beds. The arrangement of counterflow gas injection has shown that very small gas flows down to 1% of particle mass flow can provide more than adequate fluidization in the multiple HX channel beds with a simultaneous increase in $h_{T,w}$ and in axial dispersion. The resulting trends show that the overall HX heat transferred $\dot{Q}_{\mathrm{HX}}$ only increased from the non-fluidized values at low excess fluidization velocities. $\dot{Q}_{\mathrm{HX}}$ leveled off at higher excess fluidization velocities due to the tradeoff between the increase in both $h_{T,w}$ and axial dispersion. Overall, this project has developed significant know-how in designing and operating a narrow-channel fluidized bed HX and its inlet flow controls. Such know-how will be critical for any possible future scale-up efforts or further efforts to design more effective fluidized bed particle HXs or indirect particle receivers.

The 1-D modeling tools developed in this study provide a robust and computationally efficient tool for designing particle HXs and indirect particle receivers. The models have been used thereunto but current efforts to import a robust and experimental calibrated model for axial dispersion coefficient D_{sv} remains as an ongoing effort to enable these models to provide a reliable tool for fluidized bed HX and particle receiver design.

6.2. Inventions, Patents, Publications, and Other Results

The partners at Mines and Sandia did not apply for any patents under this award and although some new insight has been gained in particle flow control for fluidized bed HX, the insight has been openly shared with other potential HX developers in the field which has led to ongoing collaborations through SETO funded projects with Brayton Energy, NREL's solar thermal group, and Heliogen. Two of those projects (one with Brayton and one with NREL) are working on designs to suppress axial dispersion to take advantage of the very high $h_{T,w}$ values obtainable in narrow-channel fluidized beds as measured in this study.

Numerous conference presentations and publications have been developed under this project and they are listed in Table 7 below. Currently there are five journal publications either submitted in review or being completed for submission this spring or early summer. Those papers, all of which have students as lead authors, cover the following topics:

- single-channel heat transfer testing and heat transfer correlations,
- demonstration fluidized bed particle-sCO_2 HX testing and data analysis,
- analysis of parasitic loads to support fluidization in primary HXs for TES subsystems,
- indirect particle receiver modeling to assess cavity receiver design for next-generation CSP,
- $CuCr_2O_4$ spinel synthesis for solar receiver oxide coatings.

These papers are the beginning of many other publications that are under various stages of development that stem from the work of this project.

6.3. Path Forward

The paths forward for this project are in many ways defined by collaborations that have stemmed from this work. Mines and Sandia identified the need for suppressing axial dispersion and further enhancing heat transfer if bubbling fluidized beds were to be a viable path to significantly shrinking the size and cost of particle HXs for TES subsystems in CSP applications. To this end, Mines wrote a SETO proposal, which is now funded ad DE-EE0009812, with Brayton Energy to use their expertise in extended surface fabrication to explore the use of fins in narrow channels not only to enhance heat transfer but to suppress axial dispersion. Initial results both with experimental testing and with 3-D modeling suggest that such targets are reachable and effective $h_{T,w}$ more than twice observed in this study have been demonstrated in finned plate channels.

Table 7: List of publications and presentations developed in conjunction with this project

A	**Peer-Reviewed Journal Articles (include only if manuscript accepted, including Lab-published works/white papers)**					
	Full Author List	**"Article Title"**	**Journal/Lab**	**Volume Number**	**Issue #**	**pp. (##-##)**
	Jeremy Abraham, Bradley Jesteadt, Gregory S. Jackson	sCO2 Heat Exchangers for Next Generation CSP Plants	*AIP Conference Proceedings*	*2445*	*-2002*	*16007*
C	**Book Chapters**					
	Full Author List	**"Chapter Title", Chapter # in Book Title**	**Edition**	**Full List of Editors**	**Publisher**	**pp. (##-##)**
	Gregory S. Jackson, Christos Agrafiotis, Stefania Tescari, George Karagiannakis, & Andrea Ambrosini	Storage with Oxide Materials" in Concentrating Solar Power and Thermochemical Processes		Jane H. Davidson, Cliff K. Ho	World Scientific Publishing	
E	**Conference Publications (include only if accepted by organizer)**					
	Full Author List	**"Article Title"**	**Paper Number**	**Conference/Proceedings**	**Conference**	**Date**
	Winfred Arthur-Arhin, Azariah Thompson, Chris P. Bowen, Kevin J. Albrecht, Gregory S. Jackson	Design of a 40-kWth Counterflow Particle-Supercritical Carbon Dioxide Narrow-Channel Fluidized Bed Heat Exchanger		SolarPACES 2021	virtual	accepted for publication in AIP proceedings
	Keaton J. Brewster, Azariah Thompson, Kevin J. Albrecht, Gregory S. Jackson, Dereje Amogne	Demonstrating a 40-kWth, Counterflow Particle-sCO2 Narrow-Channel, Fluidized Bed Heat Exchanger		SolarPACES 2022	Albuquerque, NM	
F	**Conference Presentations**					
	Full Author List	**"Paper Title"**	**Paper Number**	**Session/Symposium/Conf**	**Conference**	**Date**
	Keaton Brewster, Winfred Arthur-Arhin, Luca Imponenti, Gregory S. Jackson	Modeling of an Indirect Fluidized Bed Particle Receiver for Concentrating Solar Power		ASME 2022 Energy Sustainability	Philadelphia, PA	07/11-13/22
	Winfred Arthur-Arhin, Jesse R. Fosheim, Azariah Thompson, Gregory S. Jackson	Assessing Parasitic Losses in Narrow-Channel, Fluidized-Bed Particle-sCO2 Heat Exchangers for Next Generation CSP Plants		ASME 2022 Energy Sustainability	Philadelphia, PA	07/11-13/22
	Winfred Arthur-Arhin, Kevin J. Albrecht, Jesse R. Fosheim, Keaton Brewster, Azariah Thompson, Wanjun Dang, Katherine Schubert, Gregory S. Jackson	Testing of a 40-kWth Counterflow Particle-Supercritical Carbon Dioxide Narrow-Channel Fluidized Bed Heat Exchanger		SolarPACES 2022	Albuquerque, NM	9/27-30/2022
	Wanjun Dang, Katherine Schubert, Gregory S. Jackson	Cost-effective pneumatic particle recycling system for lab-scale particle heat exchanger studies		SolarPACES 2022	Albuquerque, NM	9/27-30/2022
	Keaton Brewster, Winfred Arthur-Arhin, Luca Imponenti, Wanjun Dang, Katherine Schubert, Gregory S. Jackson	Parametric Modeling of an Indirect Fluidized Bed Particle Receiver for Concentrating Solar Power		SolarPACES 2022	Albuquerque, NM	9/27-30/2022

Mines has also become a key member of NREL's Light-Trapping Cavity Particle Receiver (LTCPR) development for an indirect receiver concept. That project is exploring novel channel designs and smaller silica particles to achieve $h_{T,w} > 1000$ W m^{-2} K^{-1}. Mines has demonstrated such values for these particles in smooth plates, but further continuous flow data is needed to understand how these smaller particles impact axial dispersion and its effects on heat transfer.

Mines has also won an award to study the coupling of particle-wall heat transfer with decarbonation reactions in limestone calciners for cement production in collaboration with Heliogen and the University of Michigan. Mines work will support the development of reactor-wall boundary conditions to assess the viability of fluidized bed heat transfer to accelerate reaction rates near the wall and mitigate external wall temperatures in solar-driven calcination for carbon-free clinker formation.

Beyond these practical studies, there are many fundamental insights that Mines wants to pursue with the experimental set up and the modeling tools that have been established in this study. Studies should be pursued on the impacts on fluidized bed heat transfer of narrower channels, which have been extremely beneficial for improving moving packed beds. Further studies in continuous flow mode for a wider range of particle dimensions and size distributions should be pursued to understand how particle size distributions beyond just mean diameter can be manipulated to improve heat transfer in channel beds.

References

1. Ho, C.K., Carlson, M., Albrecht, K. J., Ma, Z. W., Jeter, S., Nguyen, C. M., *Evaluation of Alternative Designs for a High Temperature Particle-to-sCO(2) Heat Exchanger.* Journal of Solar Energy Engineering-Transactions of the ASME, 2019. **141**(2).
2. Jackson, G.S., Imponenti, L., Albrecht, K. J., Miller, D. C., Braun, R. J., *Inert and Reactive Oxide Particles for High-Temperature Thermal Energy Capture and Storage for Concentrating Solar Power.* Journal of Solar Energy Engineering-Transactions of the ASME, 2019. **141**(2).
3. Bauer, T., Pfleger, N., Breidenbach, N., Eck, M., Laing, D., Kaesche, S., *Material aspects of solar salt for sensible heat storage.* Applied Energy, 2013. **111**: p. 1114-1119.
4. Ho, C.K., Albrecht, K.J., Yue, L., Mills, B., Sment, J., Christian, J., Carlson, M., *Overview and design basis for the Gen 3 Particle Pilot Plant (G3P3).* AIP Conference Proceedings, 2020. **2303**(1): p. 030020.
5. Diago, M., Iniesta, A. C., Soum-Glaude, A., Calvet, N., *Characterization of desert sand to be used as a high-temperature thermal energy storage medium in particle solar receiver technology.* Applied Energy, 2018. **216**: p. 402-413.
6. Siegel, N.P., M.D. Gross, and R. Coury, *The Development of Direct Absorption and Storage Media for Falling Particle Solar Central Receivers.* Journal of Solar Energy Engineering-Transactions of the ASME, 2015. **137**(4).
7. Chung, K.M., et al., *Measurement and analysis of thermal conductivity of ceramic particle beds for solar thermal energy storage.* Solar Energy Materials and Solar Cells, 2021. **230**: p. 111271.
8. Turchi, C.S., Ma, Z. W., Neises, T. W., Wagner, M. J., *Thermodynamic Study of Advanced Supercritical Carbon Dioxide Power Cycles for Concentrating Solar Power Systems.* Journal of Solar Energy Engineering-Transactions of the ASME, 2013. **135**(4).
9. Mehos, M., et al., *Concentrating Solar Power Gen3 Demonstration Roadmap*, U.S.D.O.E. National Renewable Energy Laboratory, Editor. 2017.
10. Albrecht, K.J., Carlson, M.D., Laubscher, H.F., Crandell, R., DeLovato, N., Ho, C.K., *Testing and model validation of a prototype moving packed-bed particle-to-sCO2 heat exchanger.* AIP Conference Proceedings, 2020. **2303**(1): p. 030002.
11. Albrecht, K.J., Ho, C.K., *Design and operating considerations for a shell-and-plate, moving packed bed, particle-to-sCO(2) heat exchanger.* Solar Energy, 2019. **178**: p. 331-340.
12. Baumann, T., Zunft, S. *Development and Performance Assessment of a Moving Bed Heat Exchanger for Solar Central Receiver Power Plants.* Energy Procedia, 2015. **69**: p. 748-757.
13. Soo Too, Y.C., Kim, J,-S., Kuruneru, S.T.W., Stiff, R., Dawson, A., *Development of a staged particle heat exchanger for particle thermal energy storage systems.* Solar Energy, 2021. **220**: p. 111-118.
14. Ma, Z., Martinek, J. *Analysis of a Fluidized-Bed Particle/Supercritical-CO2 Heat Exchanger in a Concentrating Solar Power System.* Journal of Solar Energy Engineering, 2020. **143**(3).

15. Yu, Q., Yang, Y., Wang, Z., Zhu, H., *Modeling and parameter sensitivity analysis of bed solid particle/sCO2 heat exchanger for concentrated solar power plant.* Applied Thermal Engineering, 2021. **197**: p. 117429.
16. Thanheiser, S., M. Haider, Schwarzmayr, P., *Experimental Investigation of the Heat Transfer between Finned Tubes and a Bubbling Bed with Horizontal Sand Mass Flow.* Energies, 2022. **15**(4): p. 1316.
17. McIntyre, C.J., Symonds, R.T., Lu, D.Y., Champagne, S., Macchi, A., Mehrani, P., *Experimental evaluation of hydrodynamics and tube-to-bed heat transfer of Ilmenite ore particles at elevated pressures.* Powder Technology, 2020. **376**: p. 697-707.
18. Albrecht, K., Laubscher, H.F., Bowen, C.P., Ho, C.K., *Performance Evaluation of a Prototype Moving Packed-Bed Particle/sCO2 Heat Exchanger*. 2022: doi:10.2172/1887943.
19. Flamant, G., Flitris, Y. Gauthier, D., *Heat-transfer to walls in a high-temperature bed of Group-II particles,* Chemical Engineering and Processing-Process Intensification, 1990. **27**(3): p. 175-184.
20. Molerus, O., *Heat-transfer in gas beds 2. Dependence of heat transfer on gas velocity.* Powder Technology, 1992. **70**(1): p. 15-20.
21. Chen, J.C., *Surface Contact-Its Significance for Multiphase Heat Transfer: Diverse Examples.* Journal of Heat Transfer, 2003. **125**(4): p. 549-566.
22. Molerus, O., *Heat-transfer in gas beds 1,* Powder Technology, 1992. **70**(1): p. 1-14.
23. Molerus, O., A. Burschka, Dietz, S., *Particle migration at solid-surfaces and heat transfer in bubbling beds 2. Prediction of heat transfer in bubbling beds.* Chemical Engineering Science, 1995. **50**(5): p. 879-885.
24. Bisognin, P.C., et al., *Influence of different parameters on the tube-to-bed heat transfer coefficient in a gas-solid bed heat exchanger.* Chemical Engineering and Processing - Process Intensification, 2020. **147**: p. 107693.
25. Di Natale, F., Nigro, R., *A critical comparison between local heat and mass transfer coefficients of horizontal cylinders immersed in bubbling fluidised beds.* International Journal of Heat and Mass Transfer, 2012. **55**(25-26): p. 8178-8183.
26. Jiang, F., et al., *Study on the particle distribution of a horizontal multi-tube circulating bed.* Powder Technology, 2016. **295**: p. 272-283.
27. Fosheim, J.R., Hernandez, X., Arthur-Arhin, W.J., Thompson, A.B., Bowen, C.P. Albrecht, K.J., Jackson G.S., Design of a 40-kWth counterflow particle-supercritical carbon dioxide narrow-channel fluidized bed heat exchanger, AIP Conference Proceedings, 2815 (2023).
28. González-Portillo, L.F., et al., *Analysis of optical properties in particle curtains.* Solar Energy, 2021. **213**: p. 211-224.
29. Ho, C.K., et al., *Characterization of Particle Flow in a Free-Falling Solar Particle Receiver.* Journal of Solar Energy Engineering-Transactions of the ASME, 2017. **139**(2).
30. Kim, J.-S., et al., *Design of a multi-stage falling particle receiver with truncated-cone geometry.* AIP Conference Proceedings, 2020. **2303**(1): p. 030023.
31. Albrecht, K.J., Jackson, G.S., Braun, R.J., *Evaluating thermodynamic performance limits of thermochemical energy storage subsystems using reactive perovskite oxide particles for concentrating solar power.* Solar Energy, 2018. **167**: p. 179-193.

32. Schrader, A.J., et al., *Aluminum-doped calcium manganite particles for solar thermochemical energy storage: Reactor design, particle characterization, and heat and mass transfer modeling.* International Journal of Heat and Mass Transfer, 2020. **152**.
33. Schrader, A.J., et al., *Experimental demonstration of a 5 kW(th) granular-flow reactor for solar thermochemical energy storage with aluminum-doped calcium manganite particles.* Applied Thermal Engineering, 2020. **173**.
34. Miller, D.C., Pfutzner, C.J., Jackson, G.S., *Heat transfer in counterflow bed of oxide particles for thermal energy storage.* International Journal of Heat and Mass Transfer, 2018. **126**: p. 730-745.
35. Ansart, R., et al., *Dense gas-particle suspension upward flow used as heat transfer fluid in solar receiver: PEPT experiments and 3D numerical simulations.* Powder Technology, 2017. **307**: p. 25-36.
36. Gomez-Garcia, F., D. Gauthier, and G. Flamant, *Design and performance of a multistage fluidised bed heat exchanger for particle-receiver solar power plants with storage.* Applied Energy, 2017. **190**: p. 510-523.
37. Zhang, H.L., et al., *High-efficiency solar power towers using particle suspensions as heat carrier in the receiver and in the thermal energy storage.* Renewable Energy, 2017. **111**: p. 438-446.
38. Ho, C.K., et al., *On-Sun Testing of an Advanced Falling Particle Receiver System*, in *Solarpaces 2015: International Conference on Concentrating Solar Power and Chemical Energy Systems*, V. Rajpaul and C. Richter, Editors. 2016.
39. Zhu, J., Grace, J.R., Lim, C.J., *Tube wear in gas beds—I. Experimental findings.* Chemical Engineering Science, 1990. **45**(4): p. 1003-1015.
40. Di Natale, F. and R. Nigro, *An experimental procedure to estimate tube erosion rates in bubbling fluidised beds.* Powder Technology, 2016. **287**: p. 96-107.
41. Goel, N., et al., *Effect of temperature on abrasion erosion in particle based concentrating solar powerplants.* Solar Energy, 2021. **224**: p. 1127-1135.
42. Patil, A.V., Peters, E., Kuipers, J.A.M., *Computational study of particle temperature in a bubbling spout bed with hot gas injection.* Powder Technology, 2015. **284**: p. 475-485.
43. Abdelmotalib, H.M., Im, I. *Simulation study of the effect of the restitution coefficient on interphase heat transfer processes and flow characteristics in a fluidized bed.* Numerical Heat Transfer Part A-Applications, 2019. **75**(12): p. 841-854.
44. Bisognin, P.C., Câmara Bastos, J.C.S., Meier, H.F., Padoin, N., Soares, C., *Influence of different parameters on the tube-to-bed heat transfer coefficient in a gas-solid fluidized bed heat exchanger.* Chemical Engineering and Processing-Process Intensification, 2020. **14**7 107693.
45. Fosheim, J.R., Hernandez, X., Abraham, J., Thompson, A., Jesteadt, B., Jackson, G.S., Narrow-channel beds for particle-sCO2 heat exchangers in next generation CSP plants, AIP Conference Proceedings, 2445 (2022) 160007..
46. Albrecht, K.J., Ho, C.K., *Heat Transfer Models of Moving Packed-Bed Particle-to-sCO(2) Heat Exchangers.* Journal of Solar Energy Engineering-Transactions of the ASME, 2019. **141**(3).

47. Ehsan, M.M., Duniam, S., Li, J. S., Guan, Z. Q., Gurgenci, H., Klimenko, A., *Effect of cooling system design on the performance of the recompression CO2 cycle for concentrated solar power application.* Energy, 2019. **180**: p. 480-494.
48. Ehsan, M.M., Duniam, S. Li, J. S., Guan, Z. Q., Gurgenci, H., Klimenko, A., *A comprehensive thermal assessment of dry cooled supercritical CO2 power cycles.* Applied Thermal Engineering, 2020. **166**.
49. Jackson, G.S., et al., *CSP ELEMENTS: High-Temperature Thermochemical Storage with Redox-Stable Perovskites for Concentrating Solar Power*. 2016, Colorado School of Mines, Golden, CO.
50. Luo, K., et al., *CFD–DEM study of mixing and dispersion behaviors of solid phase in a bubbling bed.* Powder Technology, 2015. **274**: p. 482-493.
51. Zhang, Y., C. Lu, and M. Shi, *Evaluating solids dispersion in beds of fine particles by gas backmixing experiments.* Chemical Engineering Research and Design, 2009. **87**(10): p. 1400-1408.
52. Fosheim, J.R., Hernandez, X., Arthur-Arhin, W.J., Thompson, A.B., Bowen, C.P. Albrecht, K.J., Jackson G.S., *Design of a 40-kWth Counterflow Particle-Supercritical Carbon Dioxide Narrow-Channel Fluidized Bed Heat Exchanger*. in *SolarPACES 2021: International Conference on Concentrating Solar Power and Chemical Energy Systems*. 2021.
53. Kunii, D., Levenspiel, O., *Reactor Models for Bubbling Beds of Fine, Intermediate, and Large Particles for the Lean Phase Freeboard and Fast Fluidizzation,* Industrial & Engineering Chemistry Research. 1990. 1226-1234.
54. Salehi, M.-S., Askarishahi, M., Radl, S., *Quantification of Solid Mixing in Bubbling Fluidized Beds via Two-Fluid Model Simulations.* Industrial & Engineering Chemistry Research, 2020. **59**(22): p. 10606-10621.
55. Antonov, M., et al., *Effect of oxidation on erosive wear behaviour of boiler steels.* Tribology International, 2013. **68**: p. 35-44.
56. Goretta, K.C., et al., *Erosion of work-hardened copper, nickel, and 304 stainless steel.* Wear, 1991. **147**(1): p. 145-154.
57. Divakar, M., Agarwal, V.K., Singh, S.N., *Effect of the material surface hardness on the erosion of AISI316.* Wear, 2005. **259**(1): p. 110-117.
58. Javaheri, V., Porter, D., Kuokkala, V.-T., *Slurry erosion of steel – Review of tests, mechanisms and materials.* Wear, 2018. **408-409**: p. 248-273.
59. Islam, M.A., Farhat, Z.N., *Effect of impact angle and velocity on erosion of API X42 pipeline steel under high abrasive feed rate.* Wear, 2014. **311**(1): p. 180-190.
60. Boehlert, C.J., Longanbach, S.C., *A comparison of the microstructure and creep behavior of cold rolled Haynes® 230 alloy™ and HAYNES® 282 alloy™.* Materials Science and Engineering: A, 2011. **528**(15): p. 4888-4898.
61. González de Arrieta, I., et al., *Infrared emissivity of copper-alloyed spinel black coatings for concentrated solar power systems.* Solar Energy Materials and Solar Cells, 2019. **200**: p. 109961.
62. Rubin, E.B., Chen, Y., Chen, R., *Optical properties and thermal stability of Cu spinel oxide nanoparticle solar absorber coatings.* Solar Energy Materials and Solar Cells, 2019. **195**: p. 81-88.
63. Trendewicz, A., et al., *One dimensional steady-state circulating -bed reactor model for biomass fast pyrolysis,.* Fuel, 2015. **144**: p. 439-440.

64. Syamlal, M., Gidaspow, D., *Hydrodynamics of Fluidization - Prediction of wall-to-bed heat transfer coefficients.* AIChE Journal, 1985. **31**(1): p. 127-135.
65. Span, R., Wagner, W., *A New Equation of State for Carbon Dioxide Covering the Fluid Region from the Triple-Point Temperature to 1100 K at Pressures up to 800 MPa.* Journal of Physical and Chemical Reference Data, 1996. **25**(6): p. 1509-1596.
66. Vesovic, V., et al., *The Transport Properties of Carbon Dioxide.* Journal of Physical and Chemical Reference Data, 1990. **19**(3): p. 763-808.
67. Dyreby, J., et al., *Design Considerations for Supercritical Carbon Dioxide Brayton Cycles With Recompression.* Journal of Engineering for Gas Turbines and Power-Transactions of the ASME, 2014. **136**(10).
68. Breault, R.W., *A review of gas–solid dispersion and mass transfer coefficient correlations in circulating beds.* Powder Technology, 2006. **163**(1): p. 9-17.
69. Syamlal, M., Gidaspow, D., *Hydrodynamics of fluidization: Prediction of wall to bed heat transfer coefficients.* AIChE Journal, 1985. **31**: p. 127-135.
70. Albrecht, K.J., Carlson, M.D., Ho, C.K., *Integration, control, and testing of a high-temperature particle-to-sCO2 heat exchanger.* AIP Conference Proceedings, 2019. **2126**(1): p. 030001.
71. Jobson, D.A., *On the Flow of a Compressible Fluid through Orifices.* Proceedings of the Institution of Mechanical Engineers, 1955. **169**(1): p. 767-776.